INTERFEROMETRIC TECHNIQUE FOR MICROSTRUCTURE METROLOGY USING AN INDEX MATCHING LIQUID

By

Daryl Purcell

A dissertation submitted to the faculty of
The University of North Carolina at Charlotte
in partial fulfillment of the requirements
for the degree of Doctor of Philosophy in
Optical Science and Engineering

Charlotte

2010

Approved by:

_____
Dr. Angela D. Davies

_____
Dr. Faramarz Farahi

_____
Dr. Robert K. Tyson

_____
Dr. M. Yasin Akhtar Raja

_____
Dr. Vasily N. Astratov

_____
Dr. Kevin M. Lawton

UMI Number: 3404865

All rights reserved

INFORMATION TO ALL USERS
The quality of this reproduction is dependent upon the quality of the copy submitted.

In the unlikely event that the author did not send a complete manuscript
and there are missing pages, these will be noted. Also, if material had to be removed,
a note will indicate the deletion.

UMI 3404865
Copyright 2010 by ProQuest LLC.
All rights reserved. This edition of the work is protected against
unauthorized copying under Title 17, United States Code.

ProQuest LLC
789 East Eisenhower Parkway
P.O. Box 1346
Ann Arbor, MI 48106-1346

©2010
Daryl Purcell
ALL RIGHTS RESERVED

ABSTRACT

DARYL PURCELL. Interferometric technique for microstructure metrology using an index matching liquid. (Under the direction of DR. ANGELA DAVIES)

Non-null interferometry offers a viable alternative to traditional interferometric testing of aspheric micro-lenses since computer generated holograms or null optics whose fabrication and testing are very expensive, are not required. However, due to the violation of the Nyquist sampling theorem these non-null tests provide limited dynamic range. The dynamic range of these non-null tests can be extended by implementing an index liquid which allows the measurement of micro-lenses with several microns of departure from a sphere. The first objective of this dissertation was to test important micro-lens properties such as the sag, radius of curvature and form errors for a micro-lens by using an index liquid. The results compared favorably to measurements taken on a Twyman-Green interferometer, a contact profilometer and an optical non-contact profilometer. Also, retrace errors, which are aberrations caused by altered ray paths of the test beam through a micro-lens were investigated. Reverse ray-trace and reverse optimization techniques are typically used to calibrate retrace errors, but in depth knowledge of the interferometer optics is assumed, and hence cannot be used for systems containing commercial optics. In this dissertation, re-trace errors are quantified and a novel calibration procedure derived to experimentally compensate for these errors. This retrace error calibration led to agreement of within 1% for the sag values between the index liquid technique and a profilometer. The second objective of this dissertation was to enable measurements of arbitrary geometries and to reduce testing time compared to profilometry. The index liquid technique was applied to faceted microstructured optical products which are

becoming more widespread due to advances in manufacturing. Many of these structures contain faceted surfaces with steep slopes. Adequate metrology for such surfaces is lacking. The use of the index liquid technique achieved high quality, high speed measurements of such faceted microstructures. Refraction is accounted for at the interfaces, rather than consider only optical path length changes due to the index liquid, and this significantly improves the facet angle measurement. The technique is demonstrated with the measurement of an array of micro-pyramids and show that our results are in good agreement with measurements taken on a contact profilometer. The index liquid measurements took approximately five seconds to complete compared to a measurement time of six hours for the contact profilometer. The technique was also extended to measure opaque micro-corner cubes by implementing an intermediate replication step. This allowed a measurement of the angle between facets of a nickel micro-corner cube hexagonal array, a combination not previously demonstrated in the literature. A first order uncertainty analysis was carried out on the index liquid technique to determine any limiting factors that need to be taken into account when assessing such parameters as the sag and facet angle. The uncertainties in the sag and facet angle were found to be well below 1%. Lastly secondary factors such interferometer bias, refraction, masking effects and pixel calibration were investigated to understand the possible implications on the sag and facet angle calculation.

ACKNOWLEDGEMENTS

I am very thankful for all the help and dedication provided by my advisor Dr. Angela Davies. You have given me tremendous technical as well as career advice and you are largely responsible for the wonderful experience that I had in visiting Belgium and Poland where I learned a great deal about microstructure metrology. Angela, I owe the direction of my career to you and will be eternally grateful. I would also like to thank Dr. Faramarz Farahi for giving me great ideas for my dissertation and for keeping me motivated throughout my research. Also, I truly enjoyed working in the UNCC Optics Metrology group, alongside Ayman Samara, Amit Suratkar, Kate Medicus, Brent Bergner, Solomon Gugsa, Serenity Dunn, and Javaid Ikram. In addition, I would like to thank the University of North Carolina at Charlotte, the Department of Physics and Optical Science, and also Kert Edward who allowed me to exchange numerous ideas with him no matter how farfetched. I am also thankful for the funding provided by the National Science Foundation (NSF) (grant #0348142). Special thanks also to the Vrije Universiteit Brussel research group and Dr Heidi Ottevaere for allowing me to use all the wonderful microstructure testing equipment that allowed me to tremendously further my research. Special thanks to Tessera (formerly Digital Optics Corporation), Reflexite and the University of Bremen for providing microstructure samples. Lastly, I am especially grateful to my wife, family and my parents for their constant support and encouragement, and for their genuine interest in my work.

TABLE OF CONTENTS

LIST OF TABLES xvi

CHAPTER 1: INTRODUCTION 1

Micro-lens Arrays 3

Micro-Pyramids/Prisms 10

Micro-Lens/Array Testing 13

Micro-faceted Structure Testing 19

CHAPTER 2: MICRO-STRUCTURE CHARACTERISTICS AND INDEX LIQUID METROLOGY 24

Geometrical Optics 24

Paraxial Approximation 25

Refraction through plane surfaces 26

Refraction at a spherical surface 27

Aberration Theory 29

Ray and Wave Aberrations 30

Zernike Polynomials 36

Diffraction 38

Interference 39

Optical Path Difference and Phase Difference 40

Two-beam Interference 41

Phase-Shifting Interferometry 42

Spatial Sampling 43

Aliasing 45

Phase Unwrapping 45

Aspherical Surfaces 46

Retrace Errors 49

Roughness, Form and Waviness 51

Faceted Micro-Structure Geometry 52

Index Liquid Metrology 55

Sensitivity vs. Fringe Density 62

Index Liquids 65

CHAPTER 3: MICROSTRUCTURE TESTING 68

Mach-Zehnder Interferometer 68

Adjustment of the MZ Interferometer 71

Measurable Quantities and Measuring Procedures 73

Twyman-Green Interferometer 73

Optical Non-Contact Profiler 76

Contact Stylus Profiler 78

Twyman-Green/ MZ interferometer at UNC Charlotte 78

CHAPTER 4: RESULTS 93

Sag Measurement 93

Diameter Measurement 96

Radius of Curvature 98

Form Errors 107

Micro-Pyramid Testing 110

Micro-corner cube Testing 118

Micro-lens Array Testing 121

CHAPTER 5: UNCERTAINTY ANALYSIS 129

Micro-lens Sag Uncertainty 130

Micro-pyramid Facet Angle Uncertainty 141

Retrace Errors 142

Interferometer Bias 149

Refraction Effects 153

Masking Effects 154

Pixel Calibration 156

CHAPTER 6: CONCLUSIONS AND FUTURE WORK 158

REFERENCES 160

LIST OF FIGURES

FIGURE 1: Micro-lens array. 2

FIGURE 2: Artist's concept of a hybrid coupler between a single-mode laser diode and a single optical fiber [1]. 3

FIGURE 3: 2D MEMS Stage integrated with a microlens array for use in an Endocopic Imaging device [12] . 4

FIGURE 4: Idealized schematic of force developed by the densified phase produced by exposure and thermal treatment [14]. 7

FIGURE 5: Basic fabrication process for arrays of spherical microlenses with DLP [15]. 8

FIGURE 6: Fabrication of refractive microlenses by reflow method. Photolithography, developing and melting of photoresist [20]. 9

FIGURE 7: RIE transfer of resist microlenses in fused silica. A correction of the lens slope is obtained by changing the etch rate during RIE [21]. 9

FIGURE 8: Micro-pyramid array. 10

FIGURE 9: Panel configuration of a reflective display laminating a light control film [22]. 11

FIGURE 10: Analog contact lithography with a HEBS glass grey-scale mask [27]. 12

FIGURE 11: Principle of cutting hexagon cube corners [33]. 14

FIGURE 12: Reflection and transmission lateral shearing interferometer [36]. 15

FIGURE 13: Setup to measure the wavefront aberrations of fused silica microlenses in transmission mode [40]. 15

FIGURE 14: Confocal setup for topography measurement using a microlens array [43]. 18

FIGURE 15: Experimental setup with the Mirau interference microscope [46]. 19

FIGURE 16: Schematic of a cantilever-type tactile sensor with piezo-resistive signal read-out and pyramid-shape probing tip [53]. 21

FIGURE 17: Interferogram of plane wave illumination on a micro-pyramid array (a) using no index liquid and (b) using an index liquid. 22

FIGURE 18: Illustration of the law of reflection and refraction. 25

FIGURE 19: The bending of rays at an interface. (a) For rays traveling from a medium where $n_1<n_2$ the rays bend toward the normal. (b) For rays traveling from a medium where $n_2>n_1$ the rays bend away from the normal. 27

FIGURE 20: Refraction at a spherical surface. 28

FIGURE 21: Plano-convex micro-lens parameters. 29

FIGURE 22: Illustration of ray and wave aberrations [71]. 30

FIGURE 23: Relationship between ray and wave aberrations [71]. 31

FIGURE 24: Spherical aberration of a lens, producing in (a) different image distances and in (b) different focal lengths, depending on the lens aperture [71]. 33

FIGURE 25: Coma due to a tangential fan of parallel rays [71]. 35

FIGURE 26: Astigmatic line images T and S of an off-axial point P due to tangential and sagittal fans of light rays through a lens [71]. 36

FIGURE 27: Images of a square grid (a) showing pincushion distortion (b) and barrel distortion (c) due to non-uniform magnifications [71]. 36

FIGURE 28: A succession of diffraction patterns at increasing distance from a single slit; Fresnel at the bottom (nearby), going toward Fraunhofer at the top (faraway) [76]. 40

FIGURE 29: *OPD* between points *a* and *b*. 41

FIGURE 30: Four interferograms with a phase-shift of 90 degrees between each. 43

FIGURE 31: The pixel MTFs for sensors with width-to-pitch ratios of 50 and 100%. 44

FIGURE 32: (a) Sampled interferogram of a defocused wavefront. (b) Under-sampled interferogram showing aliasing. (c) Unwrapped phase map of (b) [49]. 45

FIGURE 33: The phase unwrapping process in one dimension. 46

FIGURE 34: CGH in reflection testing of aspheric lens. 49

FIGURE 35: A surface profile represents the combined effects of roughness, waviness and form [91]. 53

FIGURE 36: (a) The structure of MTCCA. (b) The structure of MSCCA. 53

FIGURE 37: Retro-reflection in a micro-prismatic sheeting [92]. 55

FIGURE 38: Geometric and effective aperture [94]. 56

FIGURE 39: The optical principle showing the three possible cases of the emitted light: (a) direct 56

FIGURE 40: (a) Square Pyramid. (b) Tetrahedron. 57

FIGURE 41: Schematic of the measurement principle for a micro-lens. 58

FIGURE 42: Micro-pyramid measurement principle. 61

FIGURE 43: Max measurable sag vs. refractive index of index liquid. 64

FIGURE 44: Minimum resolvable feature vs. index liquid. 65

FIGURE 45: (a) MZ schematic and (b) picture of the MZ interferometer used for transmitted light measurements [101]. 70

FIGURE 46: Index liquid metrology on MZ interferometer. 71

FIGURE 47: (a) Working principle and (b) picture of Twyman-Green interferometer [103]. 75

FIGURE 48: (a) Schematic and (b) picture of the WYKO optical non-contact profilometer [104]. 77

FIGURE 49: (a) Schematic and (b) picture of Dektak profilometer [67]. 79

FIGURE 50: (*a*) The MORTI schematic is shown. It is a combination of the Twyman–Green (solid line) and Mach–Zehnder (dashed line) interferometer. (b) A picture of MORTI [105]. 80

FIGURE 51: (a) The *z* distance from the confocal position to the (b) cat's eye position is the radius of curvature. When moving the sample from the cat's eye to the (c) MZ confocal position the front focal length is measured. 81

FIGURE 52: (a) Initial layout of beam expander design. (b) Lens data editor table showing the variables for optimization in the initial beam expander design. 83

FIGURE 53: (a) Optimized layout for 5X beam expander. (b) Wavefront map showing PV error less than $2e^{-3}$ waves. 84

FIGURE 54: Excel spreadsheet containing thin-lens equation to aid in beam-expander 86

FIGURE 55: (a) Lay out of final beam expander system. (b) Wavefront error map. (c) Zernike fringe coefficients. 88

FIGURE 56: Fully assembled beam expander system. 89

FIGURE 57: Transmitted wavefront error for beam expander system incorporated into MORTI. 90

FIGURE 58: Fizeau interferometer used to test the transmission wavefront error in the beam expander system. 91

FIGURE 59: Transmitted wavefront error of beam expander system tested on a WYKO RTI Fizeau interferometer. 92

FIGURE 60: (a) Image of Digital Optics Corporation microlens array. (b) Enlarged image of individual micro-lens. 94

FIGURE 61: Contour map of the micro-lens obtained by using a WYKO NT 2000 profilometer. 95

FIGURE 62: (a) Interferogram of micro-lens. (b) Contour map of micro-lens obtained by using the MZ interferometer with water as the index liquid. 96

FIGURE 63: (a) Mask circle for micro-lens measured on WYKO NT profiler. (b) Mask circle for micro-lens measured on MZ interferometer with 1.33 index liquid. 98

FIGURE 64: (a) Confocal position for micro-lens. (b) Cat's eye position of micro-lens. 100

FIGURE 65: ROC as a function of conic values when fitting to a best-fit sphere. 101

FIGURE 66: Best fit sphere ROC vs. clear aperture of aspheric micro-lens for a conic of -1. 102

FIGURE 67: ROC as a function of positive conics when fitting to a best-fit sphere. 103

FIGURE 68: Asphere fit vs. best-fit sphere for index liquid technique. 103

FIGURE 69: Null cavity correction for the confocal and cat's eye positions. 106

FIGURE 70: (a) Interferogram for index liquid of 1.80. (b) Surface Profile for index liquid of 1.80. 108

FIGURE 71: (a) Form errors for TWG interferometer (PV = 670 nm, rms = 149.3 nm). (b) Form errors for index liquid technique (PV = 824.4 nm, rms = 133.6 nm). 109

FIGURE 72: (a) MZ interferometer bias (PV = 449.4 nm, rms = 59 nm). (b) Form error map for index liquid technique with interferometer bias removed (PV = 678.5 nm. rms = 121.9 nm). 109

FIGURE 73: (a) 90 degree rotation. (b) 180 degree rotation. (c) 270 degree rotation. 110

FIGURE 74: (a) Interferogram of plane wave illumination on micro-pyramid array using no index . (b) Interferogram of plane wave illumination on micro-pyramid array obtained using an index liquid. 111

FIGURE 75: Schematic of micro-prism measurement set-up. 112

FIGURE 76: Surface profile obtained with the Dektak surface profilometer. 113

FIGURE 77. Surface map obtained using the MZ interferometer in conjunction with an index matching liquid. 114

FIGURE 78: Polygon mask for MZ index liquid data. 115

FIGURE 79: (a) Binary image of masked MZ data. (b) Labeled facets. 116

FIGURE 80: Example of extracted facet angle. 116

FIGURE 81: (a) Facet angle map of micro-pyramid array obtained with the Dektak surface profilometer. (b) Facet angle map of micro-pyramid array obtained with MZ interferometer. 117

FIGURE 82: SEM image of micro-corner cube array fabricated at University of Bremen. 119

FIGURE 83. (a) Interferogram of micro-corner cube array measurement. (b) Surface profile of replicated micro-corner cube array obtained with MZ interferometer in conjunction with an index matching liquid. 120

FIGURE 84. Mask used for analysis of five randomly selected micro-corner cube arrays with its numbered facets. 121

FIGURE 85: Diagram illustrating the color and letter format for each micro-corner cube. 122

FIGURE 86: Vrije University micro-lens array. 123

FIGURE 87: (a) Interferogram for micro-lens array with 20 μm sag tested in air. (b) Interferogram for micro-lens array with 20 μm sag tested with water as the index liquid. 124

FIGURE 88: Contour map of the Vrije micro-lens array using the plane wave geometry in the MZ interferometer with water as the index material. 125

FIGURE 89: Sag map of the Vrije micro-lens array. 125

FIGURE 90: ROC map of Vrije micro-lens array. 126

FIGURE 91: PV deviation from sphere map for Vrije micro-lens array. 126

FIGURE 92: Form error map of Vrije micro-lens array. 127

FIGURE 93: Zernike coefficients showing form error map dominated by 4^{th} and 5^{th} order spherical aberration. 128

FIGURE 94: Histogram illustrating 20Pt P-V values for θ_4. 139

FIGURE 95: Defocus as a function of index liquid. 144

FIGURE 96: Spherical aberration as a function of index liquid. 144

FIGURE 97: Surface profile of micro-lens scanned by Dektak profilometer. 146

FIGURE 98: 36 Term Zernike fit to Dektak surface profile. 147

FIGURE 99: (a) Index liquid measurement with 1.33 index liquid. (b) Retrace error bias. 148

FIGURE 100: Correct index liquid measurement. 149

FIGURE 101: Dependence of sag on index liquid. 150

FIGURE 102: Interferometer bias measured on MZ interferometer. 151

FIGURE 103: Experimental data compared to equation 79. 152

FIGURE 104: Corrected sag values with interferometer bias removed. 152

FIGURE 105 (a) Facet angle error as a function of facet angle. (b) Facet angle error map for Reflexite sample illustrating the error in facet angle that occurs by neglecting refraction effects. 153

FIGURE 106: (a) Centered Mask. (b) De-centered mask in y. 155

FIGURE 107: Coma induced by a mask-misalignment. 156

FIGURE 108: (a) Form error map with correct lateral calibration. (b) Form error map with incorrect lateral calibration showing induced astigmatism.157

LIST OF TABLES

TABLE 1: Seidel Aberrations. 32

TABLE 2: U of A description of Zernike aberrations [73]. 34

TABLE 3: Conic Sections 47

TABLE 4: Micro-pyramidal array parameters. 57

TABLE 5: Fit statistics 104

TABLE 6: 2^{nd} Order Zernike comparison between TWG and MZ interferometer. 111

TABLE 7: Comparison between MZ interferometer and profilometer. 117

TABLE 8: Angles between facets for micro-corner cubes. 122

TABLE 9: Summary of statistical results for micro-lens parameters.127

TABLE 10: Refractive index and coefficients of index liquids. 132

TABLE 11: Uncertainty in refractive index of liquid due to wavelength and temperature. 133

TABLE 12: Dynamic repeatability measurements of OPD 135

TABLE 13: Calculation of lateral scale factor in *x* and *y* direction. 137

TABLE 14: Uncertainty in sag measurement. 140

TABLE 15: Uncertainty in facet angle measurement. 142

TABLE 16: Fit coefficients for data in Figure 95 and Figure 96. 146

CHAPTER 1: INTRODUCTION

Micro-optics is a collective term for very small optical structures and components, typically less than 1 mm in size. These tiny structures and components enable the manipulation, collection and distribution of light. Micro-optical components such as refractive micro-lens arrays and micro-pyramidal arrays are becoming more widespread due to their variety of applications. These components are the major driving force behind many technical innovations seen in technologies such as data communication applications. The wide ranges of applications are due in large part to advances in material and fabrication technologies. Because micro-optics play a large part in many photonic applications, they rank very high in many research and development initiatives.

Micro-optical systems were largely derived in part because macro-optical systems had to be miniaturized in order to meet specifications where the small size and low cost became an all important factor. In return, these micro-optical elements or systems then led to novel applications and improved performance over conventional optical systems. With cost being a decisive factor, this in turn leads to the mass-production of these micro-optical components in structured arrays. Depending on the intended application, one can either then segment the array into individual micro-components or use the array as a whole. This mass-production of micro-optics in the form of arrays represents a serious drawback in the testing of these devices. Most micro-optics metrology is done serially in

which one device is tested at a time. Because manufacturing methods can produce thousands of these devices in an array, testing times become a bottleneck in the manufacturing process. To overcome this, the test technician can measure serially a sub-sample of the manufactured micro-optics array to provide important feedback to the process engineer. Sampling assumes that the micro-optic components tested are representative of the whole array. This assumption may not be valid, and this might prevent the process engineer from improving the quality of the manufacturing process. Measurement, characterization and testing are key processes during design, production, and assembly of micro-optical components. It is the role of micro-optics metrology to

Figure 1: Micro-lens array.

provide the proper experimental support that is able to deliver initial data and in-process tests for fast product development and produce quality tests.

In this PhD dissertation, we contribute to the fascinating world of micro-optics by developing a novel technique that improves the capability of traditional interferometry by

extending its dynamic range to enable measurements of micro-optics structures and to reduce the testing time compared to other techniques. To this end we focus our techniques on two types of micro-optic structures, namely micro-lens and micro-pyramid arrays.

Micro-lens Arrays

Individual micro-lenses or micro-lens array (Figure 1) have applications that are extremely diverse. These applications can be divided into three broad categories: beam shaping, interconnections and imaging.

In beam shaping applications, micro-lenses find widespread use to correct the wavefront produced by commercial laser diodes (Figure 2). These micro-lenses are geometrically cylindrical and are used to correct the astigmatism inherent in the beam that emerges from these laser diodes [1]. The technique can also be extended in which case a micro-lens array is used to collimate the light from a linear laser diode array [2]. Micro-lens arrays are also used frequently in optical computing and optical information

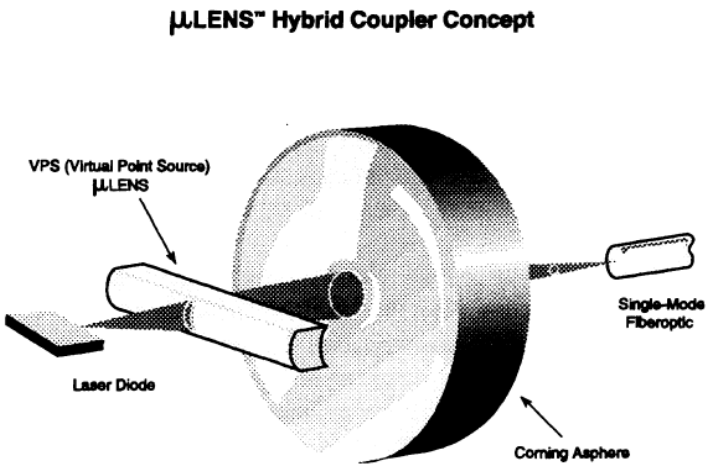

Figure 2: Artist's concept of a hybrid coupler between a single-mode laser diode and a single optical fiber [1].

processing in which the requirement is to generate an array of duplicate images of an input pattern [3]. In the telecommunication industry, linear micro-lens arrays are used to connect arrays of elements such as laser diode arrays, spatial light modulators and detector arrays. These micro-lens arrays must be able to direct a beam from a source array to a spatially variant detector array in order to manipulate data in high speed switching networks [4]. Micro-lenses have also been extensively used to couple light into optical fibers for datacom and telecom applications as well as in diverse application such as Doppler velocimeters and astronomical spectroscopy [5]. Micro-lenses are also used in measurement instrumentation, such as the use of, micro-lens arrays to concentrate light into the photo-receptive cell of CCD cameras in which they can double the photosensitivity of the sensor array [5]. Micro-lens arrays have also found use in measurement applications such as the Shack-Hartmann sensor which is used to assess the shape of an incoming wavefront [7]. This type of sensor is used in advanced telescopes for astronomy in which the information can be used to alter the profile of active mirrors and therefore correct for atmospheric disturbances [8]. Micro-lens arrays are also used in

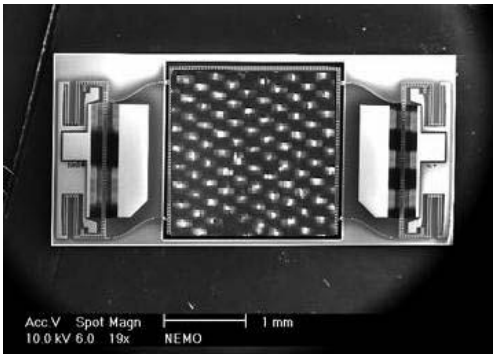

Figure 3: 2D MEMS Stage integrated with a microlens array for use in an Endocopic Imaging device [12].

confocal microscopes in which the micro-lenses are coupled to the nipkow spinning disk hence facilitating higher throughput of the captured light signal [9]. In imaging applications the whole micro-lens array is used rather than an array of elements in a technique known as integral imaging [10]. Integral imaging leads to the formation of an erect, unity magnified image, and is used in some photocopiers and fax machines. Gradient-index (GRIN) micro-lens arrays are commonly used in photocopiers since they can image an object with a large lateral field of view [11]. Micro-lens arrays have also been successfully integrated into 2D micro-mechanical systems (MEMS) devices for potential applications such as optical scanning, biological inspection (Figure 3) and micro-interferometry [12].

Although the application examples presented represent a wide variety of uses, it is by no means a complete list. In fact, no one fabrication technique can produce lenses that satisfy all the application requirements. In addition because the demand for micro-lenses continue to increase, newer fabrication techniques will continue to be developed which in turn improves the quality of the micro-lenses and leads to an extension in existing applications. Fabrication techniques implemented for macro-optics like grinding and polishing are not practical when used for making micro-lenses with diameters less than 1 mm. This has fueled the effort to borrow existing technologies from the lithographic industry that are used to make semi-conductor electronic devices that are of the same size scale. The uses of these techniques for micro-optic fabrication extend the manufacturing requirements in that now the final geometric form of the manufactured micro-lens is a critical parameter. Geometry is critical to the passive propagation of light through an optical component, unlike the electrical current propagation requirement for an electronic

device. Individual micro-lenses and arrays may have very stringent wavefront aberration and focal length requirements. This in turn leads to tight tolerances on physical parameters such as form errors, radius of curvature, and pitch across the array. In general these tolerances must also be met by a manufacturing process that is durable and cheap. As mentioned previously, the need for low cost micro-lens arrays makes mass-production critical and therefore research in the fabrication techniques needed to make large micro-lens arrays have become critical. As with micro-lens applications there are a variety of different fabrication techniques that are used to make glass and plastic refractive micro-lenses.

GRIN micro-lenses are fabricated by ion diffusion in which a dopant that raises or lowers the refractive index of the material is selectively diffused into the substrate. A radially varying index is formed in the substrate by using a mask [13]. The quality of the index profile in the central region of the lens is good, but full aperture measurements show that the aberrations increase considerably towards the edge of the lens. The main advantage of the ion diffusion process is that the surface of the micro-lens array substrate is flat allowing for monolithic integration with other micro-optical components. The main disadvantage is the relatively high fabrication cost due to long fabrication times.

Cylindrical micro-lenses that are used to correct for astigmatic wavefronts in laser diodes are made by heating and drawing a preform [1], the same way optical fibers are made. This prefrom is first made by a numerically controlled grinding technique that can be used to make any desired shape, typically in a glass substrate. After being heated and drawn, the preform shrinks by a factor of 50 -100 to form a micro-lens, but it maintains its cross-sectional profile to a remarkable level. These cylindrical micro-lenses have

diffraction limited performance and can be crossed to create arrays of square aperture micro-lenses.

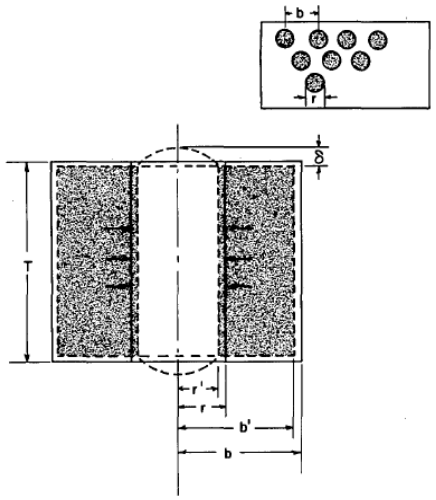

Figure 4: Idealized schematic of force developed by the densified phase produced by exposure and thermal treatment [14].

Photo-thermal techniques have also been used to fabricate micro-lenses in photosensitive glass (Figure 4). By exposing the glass to light and heat, a surface relief pattern is produced as a result of a density mismatch between the exposed and unexposed region [14]. The advantage of this technique is that biconvex micro-lenses can be fabricated. The disadvantages are high form errors and insufficient fill factors caused by a minimum of 15 μm needed between lenses to enable sufficient force to be developed to form lenses. Deep lithography with protons (DLP) is another technique which has been used to fabricate micro-lenses [15]. In this technique, protons penetrate a sample made up of linear high-molecular-weight PMMA which splits the long polymer chains [Figure 5]. This results in the molecular weight in the irradiated zones being reduced. Free radicals are also created and hence these zones can be selectively etched to create micro-lenses. Micro-lenses can also be created by swelling the irradiated domains with monomer vapor

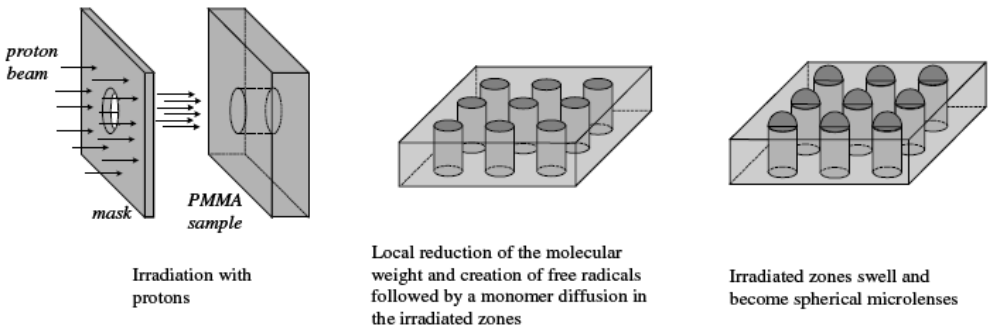

Figure 5: Basic fabrication process for arrays of spherical microlenses with DLP [15].

which in turn creates a hemi-spherical surface. The biggest drawback with DLP is the time consuming irradiation and chemical processes. Micro-lenses are also formed using a hot pressing technique in which a polycarbonate sheet is heated until soft, and then pressed against a stainless steel sheet full of apertures so that bumps form at each aperture [16]. The lenses made from this technique are in the 1-2 mm diameter range and the aberrations increase markedly outside the central region.

Mechanical milling can also be used to fabricate micro-lenses in which a female mold is first made, from which plastic micro-lenses are cast [17]. The surfaces if these micro-lenses tend to be rough and astigmatic. The focal lengths are also limited due to the size of the machining tool. Laser machining on the other hand, can be used to fabricate micro-lenses on the end face of single mode fibers [18]. The surface quality of the fiber-lenses is ~100nm rms roughness, and optical beam profiling indicates the possibility for creating spot sizes of 1/5 the core diameter at the fiber output. Micro-jetted micro-lenses make use of the technology of inkjet printers in which discrete drops of UV curable optical adhesive can be used to form micro-lenses [19]. The adhesive can be dispensed by computer control in a pre-defined array and cured by UV light. Substrate and print head

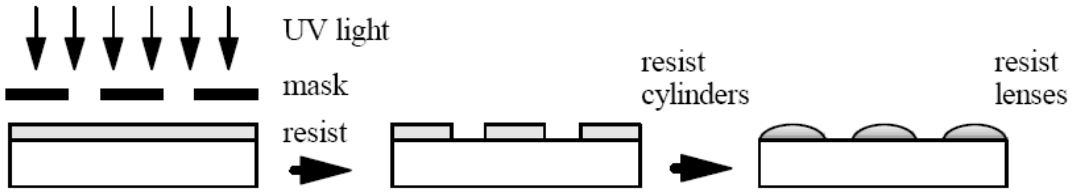

Figure 6: Fabrication of refractive microlenses by reflow method. Photolithography, developing and melting of photoresist [20].

temperature can be controlled to optimize micro-lens performance. Good focal length uniformity can be achieved with minimal spherical aberration. The most popular method of fabrication micro-lenses are by melting photoresist [Figure 6]. Micro-lenses with apertures ranging from 5-750 microns in the form of spheres or cylinders can be made with NAs ranging from 0.5 to 0.2 with diffraction limited performance [20]. These micro-lenses can also be further processed by etching the photoresist lenses into fused silica by

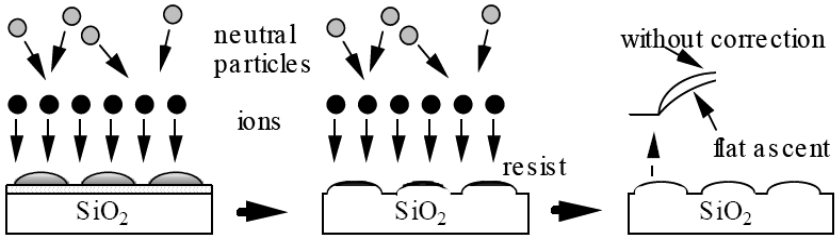

Figure 7: RIE transfer of resist microlenses in fused silica. A correction of the lens slope is obtained by changing the etch rate during RIE [21].

reactive ion etching. This increases the thermal and mechanical stability relative to photo-resist micro-lenses. By changing the etch rate and etch gas composition, the surface profile of the micro-lens can be altered to produce aspheric lenses which can be used to reduce spherical aberration (Figure 7) [21]. As can be seen, there are a variety of manufacturing methods from micro-lenses and micro-lens arrays. Each technique has its own advantages and disadvantages and no one technique can satisfy the variety of all

applications. There are new manufacturing technologies that are being unearthed on a regular basis, which bodes well for this rapidly expanding market.

Micro-Pyramids/Prisms

Micro-faceted structures such as micro-pyramids (Figure 8) do not offer the variety of applications when compared to micro-lenses, but they are becoming widespread in various industries. One application is in the display market where they are used to enhance the brightness and contrast ratio (Figure 9) for LCD (Liquid Crystal Display) televisions [22]. Micro-structures in the form of micro-pyramidal arrays are used as retro-reflectors to enhance the visibility of many safety products such as vehicles, clothing, traffic control signs and person safety devices [23]. Micro-faceted structures are

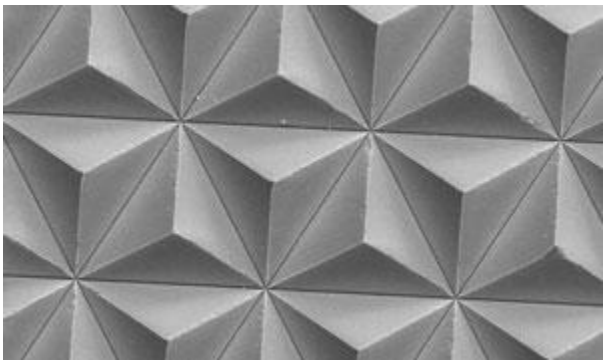

Figure 8: Micro-pyramid array.

also finding new uses in the optical communications industries where micro-pyramidal corner cubes are used in CO2 laser communication systems to yield reliable high quality voice communication under varying conditions of visibility, temperature, humidity, wind and range [24]. Micro-faceted structures such as Fresnel lenses are finding application in new solar concentration configurations to achieve a uniform intensity on the absorber plane with a moderate concentration ratio and hence achieve higher concentration

efficiencies [25]. High aspect ratio Fresnel lenses have also been employed to collimate light from an ultra-bright light-emitting diode that attained high excitation efficiencies [26]. Although micro-optics have become the obvious choice for communication over long distances, recent trends have forced designers to use optical interconnects to bridge short distances within systems such as printed circuit boards. To achieve these optical

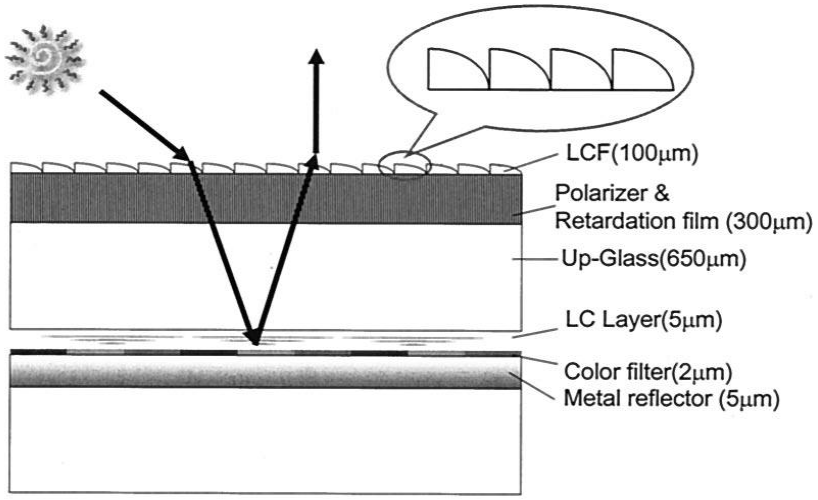

Figure 9: Panel configuration of a reflective display laminating a light control film [22].

interconnections micro-prisms have been used to achieve large coupling angles at low loss (Figure 9) [27].

As we have seen previously, there exists a large variety of ways to manufacture micro-lenses and micro-lens arrays. The situation though is different for micro-pyramid fabrication, where very few fabrication techniques exist. Most are based on mechanical methods. The difference in manufacture for micro-lenses versus micro-prisms is that for micro-lenses, the radially symmetric surfaces are well supported by physical effects such as surface tension (micro-jetted) and isotropic processes such as etching. For micro-pyramid structures, the symmetry of the profile is not continuous and hence the fabrication effort increases significantly. Micro-pyramid structures tend to be

characterized by a linear surface or phase slope which has a very sharp edge. Isotropic processes are not well suited for fabrication of sharp edges and angled steep facets. As the wedge or facet angle of the micro-pyramid increases, the traditional isotropic and lithographic processes that work so well for micro-lens fabrication start to break down.

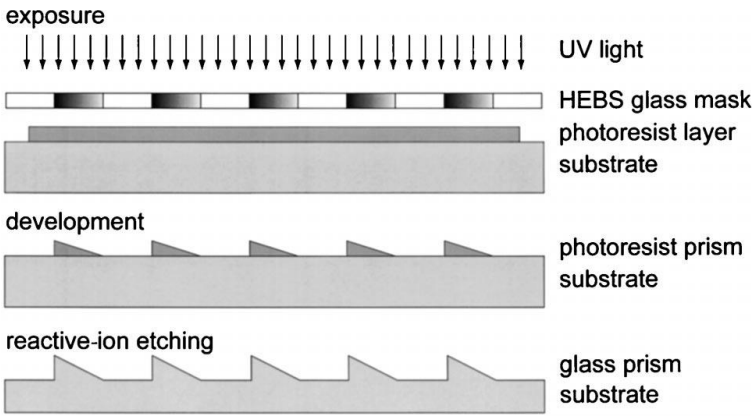

Figure 10: Analog contact lithography with a HEBS glass grey-scale mask [27].

One lithographic process that has been used to manufacture micro-pyramids is proton lithography. This is the same process mention previously to manufacture micro-lenses in which protons from a high energy source are used to shape an under-lying polymer. The micro-prism slopes can be altered by illuminating the polymer at different angles. These techniques though tend to produce rough surfaces [28]. Grey scale lithography with the help of UV photopolymerization has been used to form micro-prisms [29]. In this technique, a special polymer, PMMA, that absorbs strongly in the UV region causes the molecular chains to increase in length, hence causing a simultaneous volume and surface growth. As with deep proton lithography, the greater the slopes, the less well defined the sharpness of the micro-prism edges. Analog lithography with subsequent etching procedures have also been used to fabricate micro-pyramids with large facet angles [27].

Reflow and mass transport techniques have also been used to fabricate micro-prisms in which binary or multi-level preshapes are generated by lithographic techniques. A mass transport or reflow process is then initiated by heating the surface [30]. Laser or e-beam polishing techniques can then be used to smooth the micro-prism surface [31]. Mechanical machining techniques such as diamond turning represent by far the most common fabrication technique for micro-prism arrays. Profiling depths of several tens of micrometers can be achieved, along with a large variety of facet angles and lateral dimensions. Often, diamond turning is first used to make a master mold, then subsequent replication or hot embossing techniques are applied to fabricate micro-prism arrays [32]. Most micro-pyramids are convex pyramidal with triangular apertures. Advancements in manufacturing methods, such as diamond micro chiseling, can be used to create more complex pyramidal structures with concave pyramidal micro-cavities (Figure 11) [33]. Micro-cube corner retro reflectors with a hexagonal aperture fall under this category. They offer much higher reflection efficiencies compared to triangular aperture cube corner retro reflectors. Lastly, anisotropic etching of crystalline substrates can be used to fabricate mirror substrates [34]. The edge sharpness tends to be very good, and a larger number of angles can be etched with different wafer orientations, and etchants. Fabrication is only the first step, the manufacturing process is not complete until the part has been measured and its conformance to tolerances assessed. Characterization of these structures presents its own unique set of challenges. It is the limitations of existing measurement techniques that this dissertation research addresses.

Micro-Lens/Array Testing

Micro-lens array testing can be broken into three categories: wavefront testing,

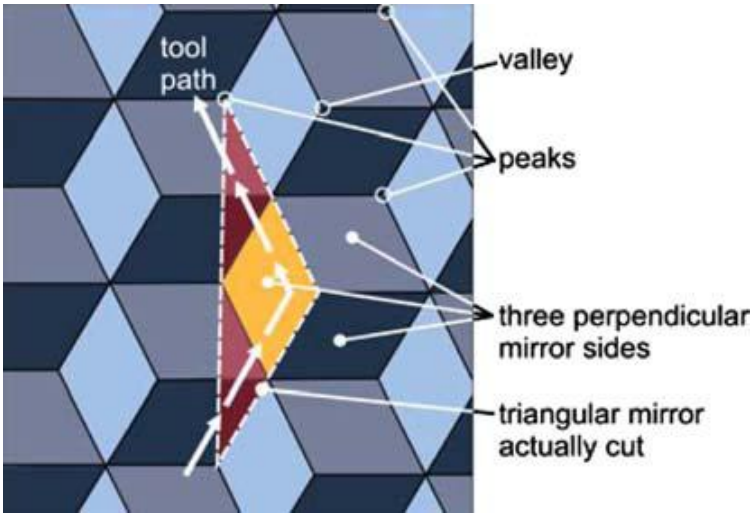

Figure 11: Principle of cutting hexagon cube corners [33].

geometrical properties, and optical properties such as focal length. Wavefront testing is one of the basic performance characteristics of a micro-lens. Interferometers such as Mach-Zehnder [35], Twyman-Green [36], and lateral shearing [36] play a significant role in wavefront testing. However, single-pass arrangements, particularly the Mach-Zehnder and lateral shearing interferometers are preferred for micro-lens testing due to the fact that sharp imaging of the lens aperture onto the detector array is absolutely essential. In a double-pass configuration like a Twyman-Green interferometer, the micro-lens is placed in the test arm of the interferometer and the wavefront travels through the test lens twice. From an imaging perspective, the lens under test exists at two locations along the optical axis and only one may be focused on the detector at a time. Diffraction at the edge of the aperture is no longer completely removed by focusing, and this interferes with the measurement, leading to erroneous wavefront measurements near the edge. Also, when testing a micro-lens array using a double-pass configuration such as a Twyman-Green interferometer, only the even part of the wavefront aberrations can be measured in the

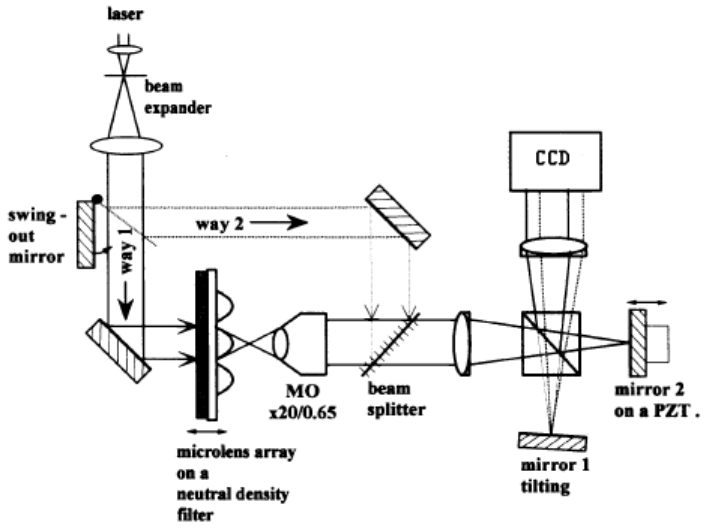

Figure 12: Reflection and transmission lateral shearing interferometer [36].

cat's eye position. [38]. Hence, coma cannot be measured due to the inversion of the wavefront upon reflection at the plane mirror.

Lateral shearing interferometry (Figure 12) calculates the wavefront aberrations of a micro-lens by measuring the partial derivates of the wavefront in two orthogonal directions. Integration of both orthogonal data sets can then be processed to calculate the wavefront aberration of the micro-lens under test [36]. Lateral shearing interferometry in conjunction with Ronchi phase gratings can also be used to measure the uniformity of a micro-lens array, although this is a qualitative test and depends on visual interpretation

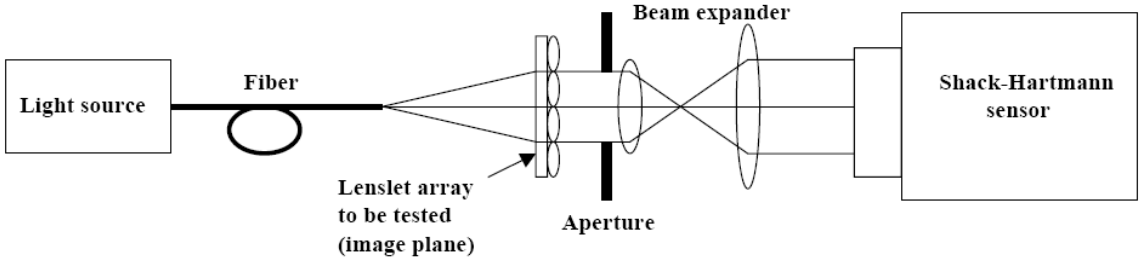

Figure 13: Setup to measure the wavefront aberrations of fused silica microlenses in transmission mode [40].

[39]. An alternative to interferometric techniques for wavefront testing of microlenses is the use of a Shack-Hartmann wavefront sensor [40]. The Shack-Hartmann sensor uses a micro-optic lenslet that is mounted in front of a CCD array to measure the wavefront aberrations of a micro-lens (Figure 13). The light that passes through the micro-lens is sampled by the individual lenslets and creates a series of focal spots onto the finely spaced CCD array. Positioning algorithms are then used to calculate the position of these focal spots with reference to a reference location. The average gradient of the wavefront over each lenslet can be calculated. The wavefront can finally be reconstructed by integration yielding the desired output.

Focal length, chromatic aberration, coupling efficiency and image quality are also important parameters in determining the quality of micro-lenses. These tests are application dependent and are based on microscopy or interferometry. In the first test a microscope in conjunction with a split-field focusing graticule is used to locate the surface of the micro-lens. The focal length can then be determined from a measurement of the displacement necessary to refocus the microscope on the image of a distant source [41]. Both, white light or monochromatic illumination can be implemented in the microscope test. Chromatic aberration can be derived from calculating the focal length at different wavelengths [42]. Interferometers can also be used to measure the focal length if they are equipped with the appropriate linear displacement transducer for length measurement. The measurement principle involves positioning the micro-lens under test on axis, so as to collimate a point source. The interference pattern is monitored to obtain null fringes. The reading from the transducer is then noted at this axial position. The micro-lens is then moved axially until the beam is focused at the cat's-eye position. The

interference pattern again is monitored to obtain null fringes. The difference in axial displacement is the focal length of the lens [41]. A Mach-Zehnder interferometer can also be used to measure the focal length by incorporating plane-wave illumination for high numerical aperture lenses in the central resolved interference field. The diameter of the micro-lens aperture should be known for this calculation [35]. A confocal microscope can be used to calculate the mean effective focal length of a micro-lens array [Figure 14]. This test incorporates a mirror on an adjustable stage with a displacement transducer that is adjusted so as to obtain a maximum intensity at the CCD for each lens element in a micro-lens array [43].

Coupling efficiency, which is expressed as the ratio of the input power to the power transferred is an important parameter in the optical communications industry. Coupling efficiency depends on several factors, which includes the numerical aperture of the lens, the wavefront aberrations, the wavelength of illumination and the numerical aperture of the fiber in which the light is to be coupled. The Strehl ratio is a measure of the point spread function of a lens compared to the ideal case and can be calculated from the wavefront aberrations of a lens [44]. Micro-lens arrays are used in many imaging applications and therefore image quality becomes an important parameter in quantifying the qualities of the micro-lenses in an array. The modulation transfer function (MTF) is used to determine the resolution of the micro-lenses by either using a test object or calculating the MTF by interferometry in which the MTF is calculated via Fourier analysis of the wavefront aberrations [35].

Geometrical properties of a micro-lens or an array, such as pitch (distance between adjacent lenses), sag (peak to valley deviation of the surface height), physical

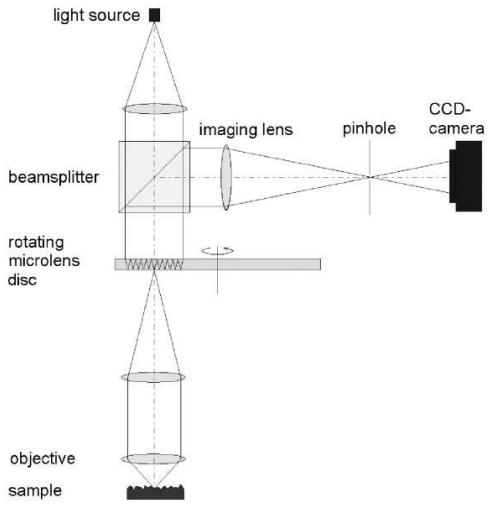

Figure 14: Confocal setup for topography measurement using a microlens array [43].

thickness (maximum local thickness of the array),radius of curvature (distance from the vertex of the lens to the center of curvature), surface shape and form error (deviation from nominal shape) can be measured in a variety of ways. Contact profilometers are the instrument of choice for measuring the surface profile of micro-lenses. This is especially true for micro-lens surfaces with steep profiles [45]. However the stylus of the profilometer is usually made of diamond which can cause damage to the surface of the micro-lens array if too much force is applied. Also, depending on the pitch and packing structure of the micro-lens array, the finite shape of the styli may not penetrate into the valleys, hence giving incorrect sag measurements. Contact profilometers are also very slow, and most can only give two dimensional scans, hence leaving out important asymmetric information. Non-contact profilometers (Figure 15) such as a scanning white light interferometer (SWLI) are capable of mapping 3-D data in a single measurement with similar resolution to contact profilometers [46]. A SWLI though, lacks the dynamic range needed to measure steep sloping aspheric micro-lens resulting in data drop-out. A confocal microscope similar to the one described previously, in conjunction with a

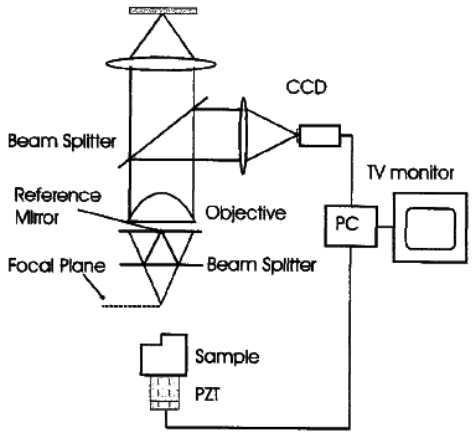

Figure 15: Experimental setup with the Mirau interference microscope [46].

Nipkow disk can also be used to measure the surface profile of micro-lenses [43]. The Nipkow disk is used to generate an array of light spots onto the surface of the micro-lens, hence allowing parallel data acquisition of multiple object points. The radius of curvature of a micro-lens can be measured directly with a Twyman-Green interferometer that is specially adapted to measure micro-lenses. The basic principle is to locate the vertex and the center of curvature of the micro-lens under test by visually looking at the interference pattern. The distance between these two positions is the radius of curvature of the micro-lens [47]. In another recent interferometric approach, reverse ray-tracing along with an index liquid were used to remove retrace error effects in the measurement of a small lens [48]. However, ray-tracing techniques cannot be applied to commercial interferometric systems because optical details are not available for the proprietary components.

Micro-faceted Structure Testing

The testing of micro-structures, such as micro-pyramids is not as developed and refined as their micro-lens counterpart. Because of this there not as many measurement techniques for micro-pyramid measurement as there are for micro-lenses. This is

primarily due to the steep slopes (>40 degrees) of these structures, which make it extremely difficult and sometimes impossible to measure the surface profile. Traditional interferometric techniques are not feasible because the high slopes cause the interference fringes to become so dense they violate the Nyquist sampling theorem [49]. The measurement range of phase-shifting interferometry can be extended by sub-nyquist interferometry [50]; however, this technique requires a sparse-array sensor which can lead to the loss of data between pixel locations. Fringe reflection, which involves the analysis of a straight fringe pattern after its deformation by reflection from a free form surface, has also been used to recover the surface profiles of high slope microstructures, but it incurs a systematic error due to the alignment of the screen, sample and camera [51]. Contact profilometers are commonly used, since they are well suited for steep profile microstructures but even then the arcing motion of the stylus arm can produce errors in the slope measurements [52]. Tactile and non-tactile sensors (Figure 16) with nanometer resolution, low contact force and higher scan speeds than traditional profilometry have been recently developed to measure high aspect ratio micro-structures [53, 54]. These sensors are still relatively slow compared to phase-shifting interferometry. Recently a technique known as digital holographic microscopy has been used to characterize micro-structures such as micro-lenses and micro-pyramids in which a hologram is captured by a CCD camera and processed digitally [55]. This technique employs the Fourier transform method to analyze the resulting hologram which permits a fast acquisition rate which is insensitive to external perturbations. This approach is similar to our proposed measurement in that an interference pattern is analyzed to extract a phase profile, and this is then converted to a height profile for the surface. The authors

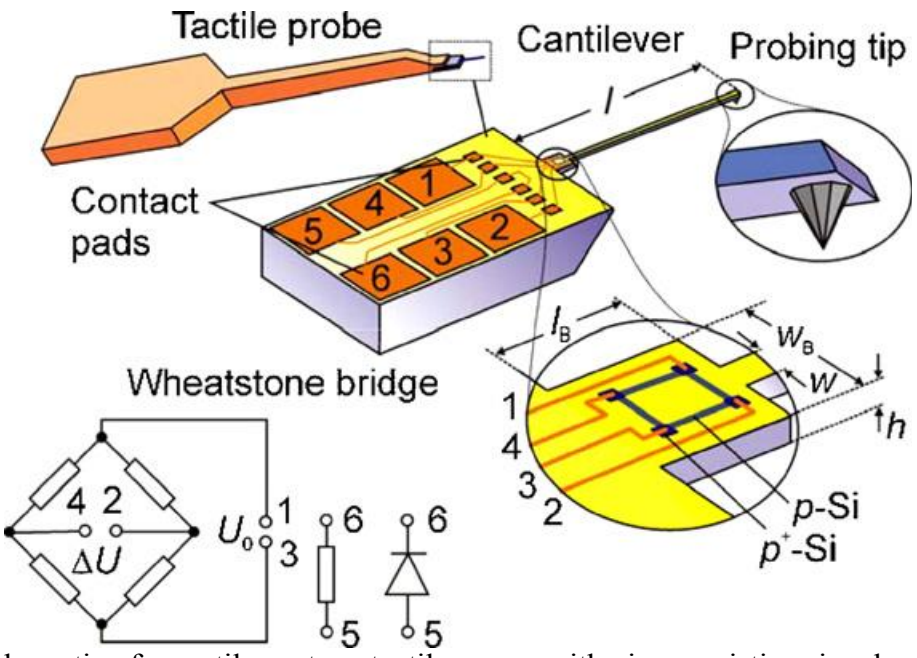

Figure 16: Schematic of a cantilever-type tactile sensor with piezo-resistive signal read-out and pyramid-shape probing tip [53].

correct for the first order effect when using an index liquid, namely scaling the phase profile by the index difference to account for the path length change introduced by the use of the index liquid. But, it does not appear that they take refraction into account and this results in systematic biases.

This dissertation demonstrates an interferometric technique that combines plane wave illumination with an index matching liquid to measure an array of micro-structures (micro-lenses, micro-pyramids) at once (versus scanning). Figure 17 shows the comparison of interferograms obtained with and without the use of an index liquid when measuring a micro-pyramidal array. Notice that without the index liquid the fringe density is too large to allow a phase measurement.

It will be demonstrated that the index liquid technique can be used to measure the sag, radius of curvature and form errors for a micro-lens and that the results compare

favorable to measurements taken on a Twyman-Green interferometer and an optical non-contact profilometer (WYKO NT 2000). The second objective is to enable measurements of arbitrary geometries and to reduce testing time compared to profilometry [56]. It is the ability to use plane wave illumination for the interferometric measurement that allows one to measure many microstructures at a time and greatly reduce measurement time. The analysis presented here accounts for path length changes introduced by the immersion liquid but in a manner whereby refraction is also taken into account. This allows the dynamic range of interferometry to be extended such that micro-lenses with several hundred of microns departure from a sphere can be measured. The measurement on the micro-faceted structures focuses on the extraction of the facet angles of the micro-pyramids under test. The facet angle is defined as the angle the surface normal each face of the micro-pyramid makes with the base of the pyramid. It is a crucial parameter for micro-pyramid manufacturing, since it determines the overall efficiency as brightness enhancers.

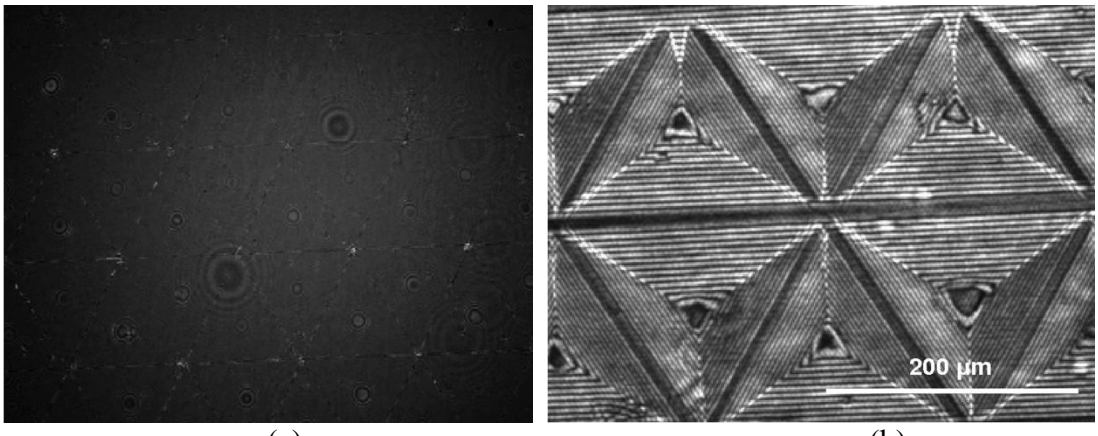

(a) (b)

Figure 17: Interferogram of plane wave illumination on a micro-pyramid array (a) using no index liquid and (b) using an index liquid.

It will be shown that measurements of a micro-pyramid array using the index liquid technique compare favorably to measurements on a VEECO Dektak contact profilometer. Measurements take approximately five seconds to complete compared to a measurement time of six hours for the contact profilometer. Also, the index liquid technique allows measurement of the angle between facets of a nickel micro-corner cube hexagonal array, a combination not previously demonstrated in the literature. An uncertainty analysis is carried out on the index liquid technique to determine any limiting factors that need to be taken into account when implementing such a technique. Lastly, we demonstrate an experimental method that can be used to compensate for re-trace errors which account for the biggest uncertainty in the calculation of the sag of a micro-lens.

CHAPTER 2: MICRO-STRUCTURE CHARACTERISTICS AND INDEX LIQUID METROLOGY

In this chapter an introduction is made to the most important geometrical and optical parameters that will be used throughout the rest of this dissertation to describe the characteristics of microstructures, namely refractive microlenses and faceted structures such as micro-pyramids. An overview of the geometrical imaging properties of microlenses as well as the impact of aberrations on image quality is also presented. Finally, the theory behind the index liquid technique is presented for both micro-lenses and micro-pyramids.

Geometrical Optics

The optical and geometrical properties of micro-lenses and micro-pyramids can be derived from a first order look at geometrical optics. Geometrical optics refers to the special case where the wavelength of light is negligible in comparison to the dimensions of optical components in an optical system. In this dissertation we are concerned with micro-structures with a foot-print varying from 200 μm to 500 μm at a measurement wavelength of 0.6328 μm. Light in this regime, can be approximated by rays which travel out from a source along straight lines or rays. The optical path length for a ray traversing through a system consisting of different media can be approximated by a sequence of straight lines. The laws of geometrical optics describe the direction of rays as it travels from one medium to another. These laws are as follows:

The law of Reflection

When a ray of light is reflected at an interface dividing two uniform media, the reflected ray remains within the plane of incidence, and the angle of reflection equals the angle of incidence. The plane of incidence includes the incident ray and the normal to the point of incidence.

The law of Refraction or Snell's Law

When a ray of light is refracted at an interface dividing two uniform media, the transmitted ray remains within the plane of incidence and the sine of the angle of refraction is directly proportional to the sine of the angle of incidence. This law can be summarized by the following equation

$$n_1 \sin\theta_1 = n_2 \sin\theta_2 , \tag{1}$$

where n_1 and n_2 are the indices of refraction of the two uniform media and θ_1 and θ_2 are the angles between respectively the incident and refracted ray and the normal to the surface. Both laws are illustrated in Figure 18.

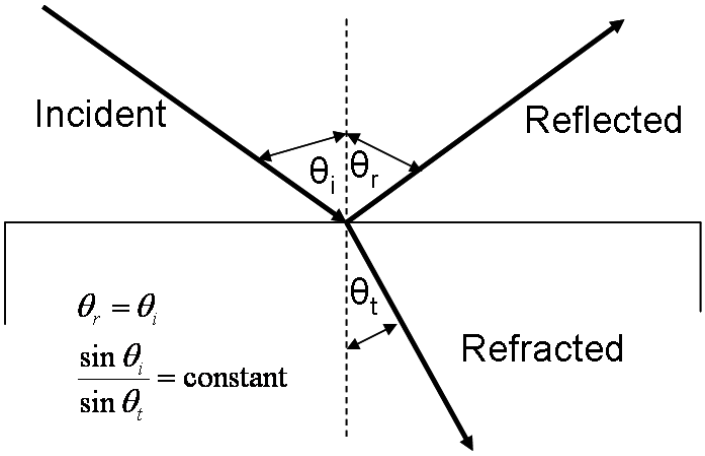

Figure 18: Illustration of the law of reflection and refraction.

Paraxial Approximation

The basic optics of image location and magnification is demonstrated by the

application of paraxial optics, commonly referred to as Gaussian optics. In Gaussian optics, the only rays that will be considered are those which lie close to the optical axis, so that all the angles are small (θ<15 degrees). Hence, Snell's law can be written as

$$n_1\theta_1 = n_2\theta_2 . \tag{2}$$

Since, in the paraxial approximation *sin (θ) = θ*.

Refraction through plane surfaces

The micro-lenses that are discussed in this dissertation are plano-convex whilst the micro-pyramids have one-side (back surface) that are planar while the other side contain surfaces that are tilted with respect to the back surface, hence a discussion on the refraction of light rays through these plane surfaces are pertinent. For rays traversing from one medium (n_1) to another (n_2) that are separated by a plane surface, Snell's law requires that if $n_1 > n_2$, the angle of refraction is greater than the angle of incidence and therefore the ray bends away from the normal. Conversely, for rays travelling from a medium with a smaller index of refraction to that of a medium with a higher index of refraction, the rays bend toward the normal. These two situations are illustrated in Figure 19. Rays though that propagate from a medium of higher refractive index to that of a lower refractive index with increasing larger angles of incidence, refract at increasingly larger angles. A critical angle of refraction is reached θ_c when the angle of refraction reaches 90 degrees. From Snell's law the critical angle is defined as

$$\theta_c = \sin^{-1}\left(\frac{n_2}{n_1}\right). \tag{3}$$

Therefore for angles on incidence greater than the critical angle, the incident ray experiences total internal reflection. Note that this phenomenon does not occur unless n_1 is greater than n_2.

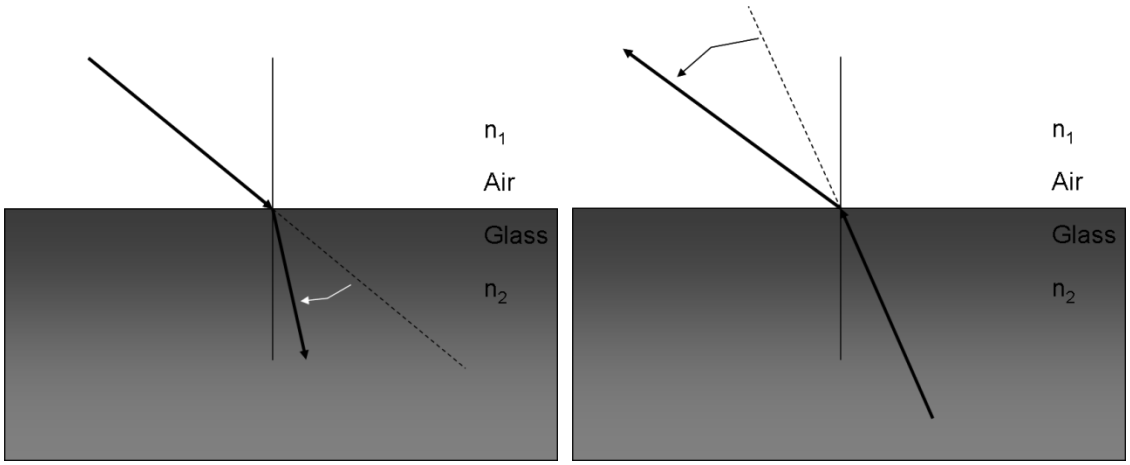

(a) (b)

Figure 19: The bending of rays at an interface. (a) For rays traveling from a medium where $n_1<n_2$ the rays bend toward the normal. (b) For rays traveling from a medium where $n_2>n_1$ the rays bend away from the normal.

Refraction at a spherical surface

To investigate refraction at a spherical surface such as in the case of a micro-lens, Figure 20 shows rays emanating from object point *O*. One ray is an arbitrary ray incident at point *P*, whilst the other ray is an axial ray normal to the surface at its vertex and therefore there is not change in direction upon refraction. The arbitrary ray though refracts according to Snell's law,

$$n_1 \sin\theta_1 = n_2 \sin\theta_2 , \tag{4}$$

These two refracted rays appear to emanate from image point *I*. The center of curvature of the concave surface is denoted at point *C*. From triangle *CPO*,

$$\theta_1 = \alpha - \varphi . \tag{5}$$

From triangle *CPI*,

$$\theta_2 = \alpha' - \varphi . \tag{6}$$

Substituting, equations (5) and (6) into equation (4) gives

$$n_1(\alpha - \varphi) = n_2(\alpha' - \varphi). \tag{7}$$

Taking the tangents of the angles and substituting into equation (7) gives

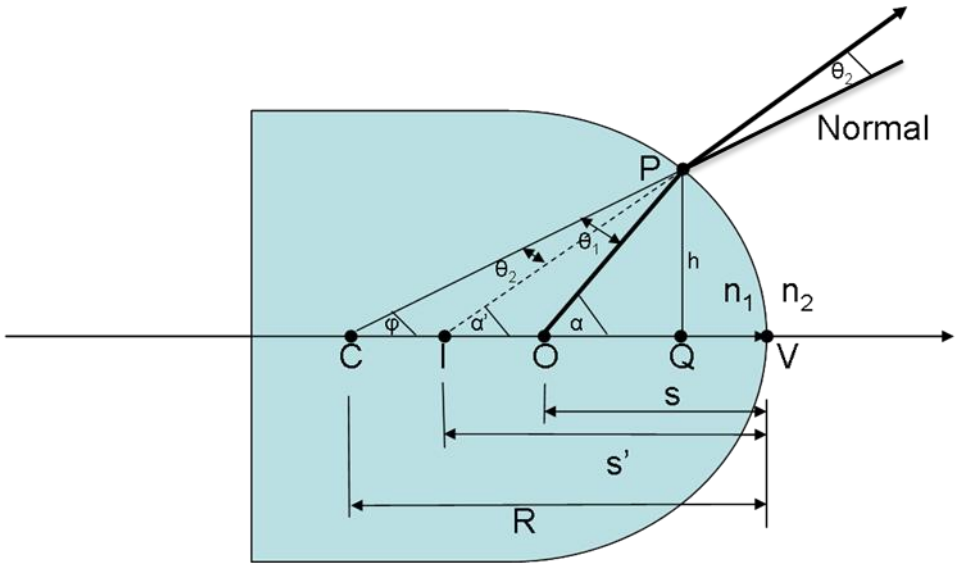

Figure 20: Refraction at a spherical surface.

$$\frac{n_1}{s} + \frac{n_2}{s'} = \frac{n_2 - n_1}{R}. \tag{8}$$

Equation 8 assumes that the distance QV is neglected in the small angle approximation and the sign convention that positive distances represent real objects while negative distances represent virtual objects and images. Hence, $s' < 0$ and the radius of curvature $R < 0$. Equation 8 holds also for convex surfaces. The distance from the object point to the vertex of the refractive surface is called the front focal length f_{ffl} if the image I is at infinity ($s' = \infty$). Equation 8 then gives

$$f_{ffl} = -\frac{n_1}{n_2 - n_1} R. \tag{9}$$

Similarly, if the image is placed at the back focal length f_{bfl}, such that the object distance equals infinity ($s = \infty$), then

$$f_{bfl} = \frac{n_2}{n_2 - n_1} R. \tag{10}$$

For a plano-convex lens, which is common in micro-lens arrays, equation 10 simplifies to

$$f = \frac{R}{n_1 - 1}. \tag{11}$$

Micro-lens arrays mostly consist of plano-convex lenses with the geometrical parameters shown in Figure 21. The variable *t* represents the substrate thickness, *R* is the radius of curvature and is the distance from the vertex of the micro-lens to the center of curvature of the lens surface. The variable *d* is the diameter of the lens, *h* is the sag which is measured form the vertex to the substrate and *f* is the front focal length as measured form the vertex. The sag of the lens is related to the diameter and radius of curvature by

$$h = R - (R^2 - \frac{d^2}{4})^{1/2}. \tag{12}$$

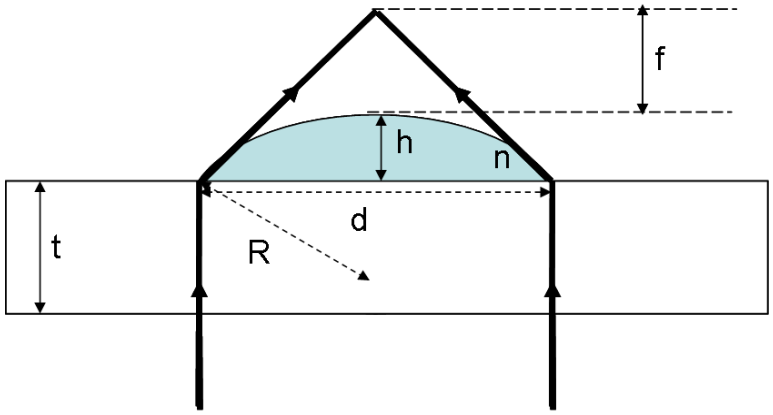

Figure 21: Plano-convex micro-lens parameters.

Aberration Theory

The paraxial formulas derived earlier for image formation by spherical refracting surfaces assumed rays both near the optical axis and at small angles to it. Once the higher order terms (x^3) for both sine and cosine functions are included inconsistencies develop with the corresponding paraxial description. These departures from Gaussian optics are referred to as aberrations. More specifically, when the x^3 term is included in the approximation for the sine function, third-order aberration theory results. For

monochromatic light there are five third order or Seidel aberrations: spherical aberration, coma, astigmatism, curvature of field and distortion. There is another aberration known as chromatic aberration which results from the wavelength dependence of the imaging properties of an optical system.

Ray and Wave Aberrations

Aberrations can be described either as ray or wave aberrations. Ray aberrations are easier to understand and can be described as in Figure 22. Here we have two wavefronts that emerge from an optical system. Wavefront W_1 is a perfect spherical reference wavefront that produces an image at point *I*. W_2 is a wavefront that contains aberrations due to the optical system. Rays from *A* (ideal ray) which is normal to W_1 intersects the image plane at point *I*, whilst rays from *B* (actual ray) which is normal to W_2 intersect the image plane at point *S*. The distance *LI* is called the longitudinal aberration and *IS* is known as the transverse aberration. These are known as ray aberrations. These aberrations can lead to the blurring of an image in a typical image forming system. Wave aberrations can be described as the optical path difference along a ray between the actual wavefront W_2 and the ideal wavefront W_1. Figure 23 can be used

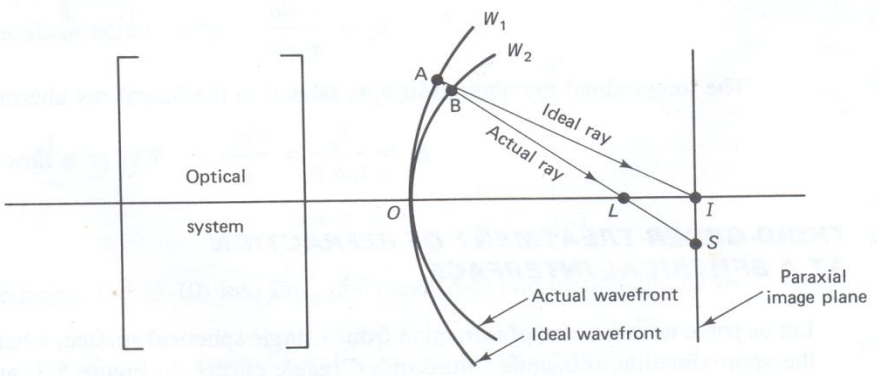

Figure 22: Illustration of ray and wave aberrations [71].

to show that there is a relationship between the ray and wave aberrations [71]. In fact, the

ray aberrations are the derivative of the wavefront aberrations. The lateral ray aberration b_y due to rays from the neighborhood of P can be approximated by

$$b_y = \frac{s' da}{n_2 dy}, \tag{13}$$

where da/dy represents the local curvature of the wavefront at P. The longitudinal ray aberration b_z can be described in terms of the lateral ray aberration b_y and is given as

$$b_z = \frac{s' b_y}{y}. \tag{14}$$

Third-order Siedel aberrations are typically described by polynomials which are derived by expanding the theory of refraction at a single spherical surface to include the x^3 terms (third-order) in polar pupil coordinates. The wavefront aberration polynomial ξ then becomes a function of the paraxial image height h' and the polar pupil coordinates r and θ and is given by

$$\begin{aligned}\xi(h', r, \theta) = {}_0C_{40} r^4 + {}_1C_{31} h' r^3 \cos\theta + \ldots \\ {}_2C_{22} h'^2 r^2 \cos^2\theta + {}_2C_{20} h'^2 r^2 + {}_3C_{11} h'^3 r \cos\theta\end{aligned}. \tag{15}$$

The C coefficients are subscripted by numbers that specify the powers of the term

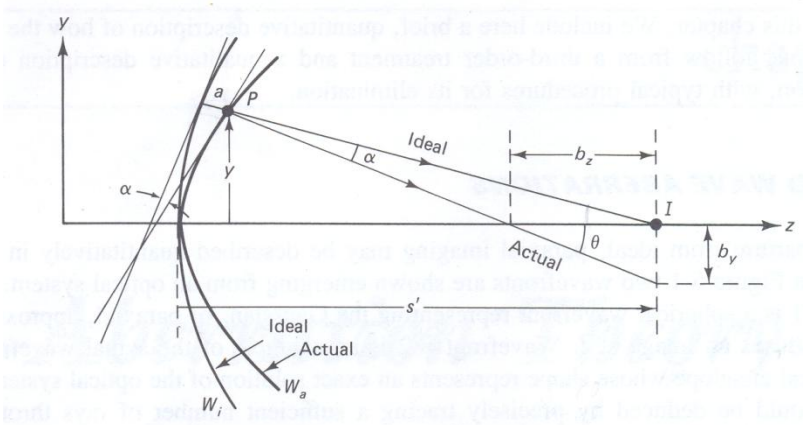

Figure 23: Relationship between ray and wave aberrations [71].

dependence on h', r and $\cos\theta$ respectively [71]. These terms comprise the five

monochromatic Seidel aberrations which are summarized in Table 1 as follows:

Table 1: Seidel Aberrations.

r^4	Spherical aberration
$h'r^3\cos\theta$	Coma
$h'^2r^2\cos^2\theta$	Astigmatism
h'^2r^2	Curvature of field
$h'^3r\cos\theta$	Distortion

Higher order (x^5, x^7 etc) aberrations also exist and are typically described by Zernike polynomials, which unlike Seidel polynomials are orthogonal polynomials, meaning that each term in the polynomial is unique and independent of the others. This orthogonality also simplifies fitting the polynomials to measured interferogram data [72]. There are two dominant naming and ordering conventions which are used to describe Zernike polynomials; OSA and University of Arizona. In this dissertation we employ University of Arizona's description in the form of thirty-six entries (Astigmatism is defined by the third term in equation 15 and increases with the off-axis object and image distances from the optical axis *h'* as well as with the aperture radius, *r*. This aberration also becomes more severe with increases in θ. Astigmatism results when rays from an off axis object point that lie in the sagittal plane come to focus at a different distance than rays that lie in the tangential plane. This is shown in Figure 26 for an off-axial point *P*. To eliminate astigmatism in an optical system, the tangential and sagittal surfaces must be made to coincide. This can be achieved by altering the curvatures and spacing between lenses. The resulting surface is then called a Petzval surface. Although in a Petzval

surface astigmatism is eliminated, field curvature (h'^2r^2) still remains because the Petzval surface is curved. This means that the focus changes from the center out to the edge of the field of view. This aberration causes flat objects to

be imaged onto a curved surface rather than a plane. To eliminate field curvature, an

Table 2) since most interferometric software applications employ this convention. The Zernike polynomials were developed as a convenient set for representing wavefront aberrations over a circular pupil. One problem with Zernike polynomials is that that non-rotationally symmetric aberrations like coma and astigmatism need to be decomposed into two components one along the x axis and another along the y axis [72]. In the following section we briefly describe the third-order Seidel aberrations in terms of their visual effects and describe some of the ways in which these aberrations can be reduced.

Spherical aberration is described by the first term in equation 15 and is the only term that does not depend on the height of the paraxial image *h'*, hence spherical aberration exits even for axial object and image points. Spherical aberration exists due to the fact that rays emanating from the extremities of the lens come to focus at different locations than rays passing through the lens closer to the optical axis. This results in longitudinal and lateral spherical aberration as shown in Figure 24. Because the focal

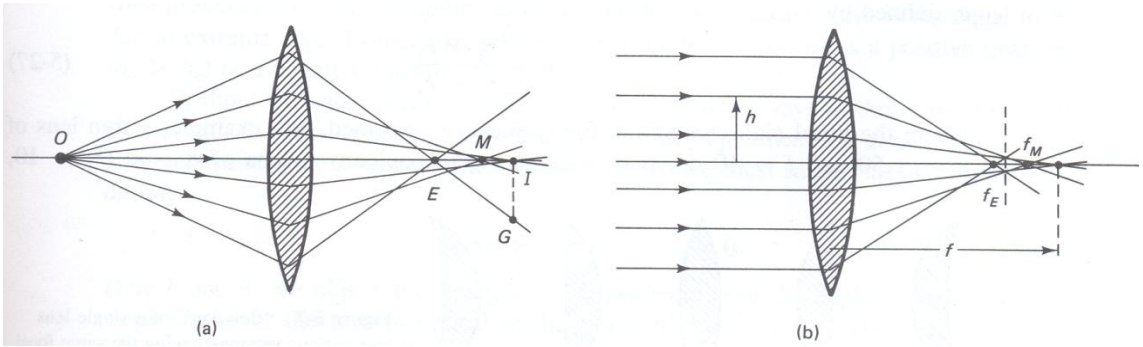

Figure 24. Spherical aberration of a lens, producing in (a) different image distances and in (b) different focal lengths, depending on the lens aperture [71].

length of the lens depends on the radii of curvature of the two surfaces, spherical aberration can be reduced by changing the shape of lens surfaces while whilst keeping the focal length constant. In fact it can be shown that for an object at infinity, a plano-convex lens results in minimum spherical aberration [71]. Incidentally, most micro-lenses that are manufactured are of this type. It should be noted though that to achieve minimum spherical aberration, the convex side of the micro-lens should face the parallel incident rays. In this way each surface contributes to refraction hence dividing the refraction over two surfaces which results in the incident angles are smaller therefore most of the rays coming to a focus on the optical axis closer to one another. In optical systems, spherical aberration can be reduced by employing positive and negative lenses since these lenses produce spherical aberration of opposite sign. This approach is used frequently when designing afocal systems. For optical systems where only a smaller number of surfaces are allowed, cemented doublets and aspherical lenses are generally employed.

Coma unlike spherical aberration depends on the object and image height *h'* which indicates an off-axis aberration. Such an aberration is prevalent in misaligned optical systems. It is represented by the second term in equation 15 which also indicates that coma is nonsymmetrical ($cos\ \theta \neq$ constant) about the optical axis and that it increases rapidly with the aperture radius of the lens, *r*. Coma results because rays passing through the periphery form images of different lateral magnification than rays passing through the center of lens. This is seen in Figure 25 for a tangential fan of parallel rays. Coma, like spherical aberration, can be either negative or positive. To reduce coma, the lateral magnification resulting from refraction by all zones of a lens must be constant [71].

Astigmatism is defined by the third term in equation 15 and increases with the off-axis object and image distances from the optical axis *h'* as well as with the aperture radius, *r*. This aberration also becomes more severe with increases in θ. Astigmatism results when rays from an off axis object point that lie in the sagittal plane come to focus at a different distance than rays that lie in the tangential plane. This is shown in Figure 26 for an off-axial point *P*. To eliminate astigmatism in an optical system, the tangential and sagittal surfaces must be made to coincide. This can be achieved by altering the curvatures and spacing between lenses. The resulting surface is then called a Petzval surface. Although in a Petzval surface astigmatism is eliminated, field curvature (h'^2r^2) still remains because the Petzval surface is curved. This means that the focus changes from the center out to the edge of the field of view. This aberration causes flat objects to be imaged onto a curved surface rather than a plane. To eliminate field curvature, an

Table 2: U of A description of Zernike aberrations [73].

$z0 = 1;$	Piston or Bias
$z1 = \rho \cos[\theta];$	Tilt x
$z2 = \rho \sin[\theta];$	Tilt y
$z3 = -1 + 2\rho^2;$	Power
$z4 = \rho^2 \cos[2\theta];$	Astig x
$z5 = \rho^2 \sin[2\theta];$	Astig y
$z6 = \rho(-2 + 3\rho^2)\cos[\theta];$	Coma x
$z7 = \rho(-2 + 3\rho^2)\sin[\theta];$	Coma y
$z8 = 1 - 6\rho^2 + 6\rho^4;$	Primary Spherical
$z9 = \rho^3 \cos[3\theta];$	Trefoil x
$z10 = \rho^3 \sin[3\theta];$	Trefoil y
$z11 = \rho^2(-3 + 4\rho^2)\cos[2\theta];$	Secondary Astigmatism x
$z12 = \rho^2(-3 + 4\rho^2)\sin[2\theta];$	Secondary Astigmatism y
$z13 = \rho(3 - 12\rho^2 + 10\rho^4)\cos[\theta];$	Secondary Coma x
$z14 = \rho(3 - 12\rho^2 + 10\rho^4)\sin[\theta];$	Secondary Coma y
$z15 = -1 + 12\rho^2 - 30\rho^4 + 20\rho^6;$	Secondary Spherical
$z16 = \rho^4 \cos[4\theta];$	Tetrafoil x
$z17 = \rho^4 \sin[4\theta];$	Tetrafoil y
$z18 = \rho^3(-4 + 5\rho^2)\cos[3\theta];$	Secondary Trefoil x
$z19 = \rho^3(-4 + 5\rho^2)\sin[3\theta];$	Secondary Trefoil y
$z20 = \rho^2(6 - 20\rho^2 + 15\rho^4)\cos[2\theta];$	Tertiary Astigmatism x
$z21 = \rho^2(6 - 20\rho^2 + 15\rho^4)\sin[2\theta];$	Tertiary Astigmatism y
$z22 = \rho(-4 + 30\rho^2 - 60\rho^4 + 35\rho^6)\cos[\theta];$	Tertiary Coma x
$z23 = \rho(-4 + 30\rho^2 - 60\rho^4 + 35\rho^6)\sin[\theta];$	Tertiary Coma y
$z24 = 1 - 20\rho^2 + 90\rho^4 - 140\rho^6 + 70\rho^8;$	Tertiary Spherical
$z25 = \rho^5 \cos[5\theta];$	Pentafoil x
$z26 = \rho^5 \sin[5\theta];$	Pentafoil y
$z27 = \rho^4(-5 + 6\rho^2)\cos[4\theta];$	Secondary Tetrafoil x
$z28 = \rho^4(-5 + 6\rho^2)\sin[4\theta];$	Secondary Tetrafoil y
$z29 = \rho^3(10 - 30\rho^2 + 21\rho^4)\cos[3\theta];$	Tertiary Trefoil x
$z30 = \rho^3(10 - 30\rho^2 + 21\rho^4)\sin[3\theta];$	Tertiary Trefoil y
$z31 = \rho^2(-10 + 60\rho^2 - 105\rho^4 + 56\rho^6)\cos[2\theta];$	Quatenary Astigmatism x
$z32 = \rho^2(-10 + 60\rho^2 - 105\rho^4 + 56\rho^6)\sin[2\theta];$	Quatenary Astigmatism y
$z33 = \rho(5 - 60\rho^2 + 210\rho^4 - 280\rho^6 + 126\rho^8)\cos[\theta];$	Quatenary Coma x
$z34 = \rho(5 - 60\rho^2 + 210\rho^4 - 280\rho^6 + 126\rho^8)\sin[\theta];$	Quatenary Coma y
$z35 = -1 + 30\rho^2 - 210\rho^4 + 560\rho^6 - 630\rho^8 + 252\rho^{10};$	Quaternary Spherical

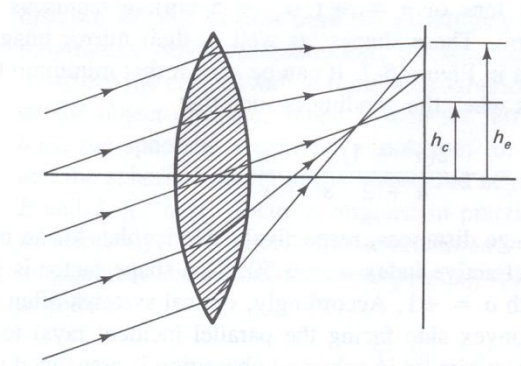

Figure 25: Coma due to a tangential fan of parallel rays [71].

aperture stop can positioned in front of a lens. This results in the sagittal and tangential surfaces that are oppositely curved and this produces a surface of least confusion that is flat [71]. Distortion which is described by the fifth term in equation 15 and shows up as a

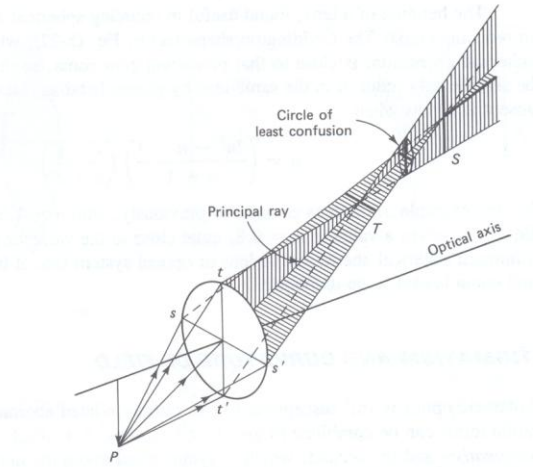

Figure 26: Astigmatic line images T and S of an off-axial point P due to tangential and sagittal fans of light rays through a lens [71].

variation in the lateral magnification for object points at different distances from the optical axis. Distortion which results in a decrease in magnification with distance from the optical axis is known as barrel distortion. Pin-cushion distortion results from an increase in magnification with object distance. Barrel and pin-cushion distortion are shown in Figure 27. Distortion is normally caused by stops that are used in turn to either decrease astigmatism or field curvature. To eliminate distortion the aperture stop should be placed at the position of the lens.

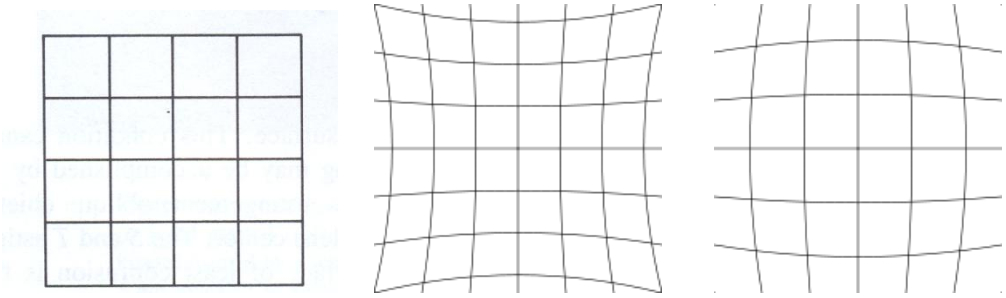

(a) (b) (c)

Figure 27: Images of a square grid (a) showing pincushion distortion (b) and barrel distortion (c) due to non-uniform magnifications [71].

Zernike Polynomials

In general it is impossible to design a system which is free from all primary Seidel

aberrations as well as higher order aberrations. Sometimes higher order aberrations are introduced to balance out the effects of Seidel aberrations. As mentioned previously, Zernike polynomials are generally used to represent these higher order aberrations. Zernike polynomials have been described in many places in the literature [74]. The Zernike polynomials $Z_n^e(\rho,\theta)$ are usually defined in polar coordinates where ρ is the normalized radial distance ranging from 0 to 1 and θ is the angle from the y axis ranging from 0 to 2π. The polynomials are orthogonal over the circle with unit radius and are given as [72]

$$\int_0^1\int_0^{2\pi} Z_n^l Z_{n'}^{l'} \rho d\rho d\theta = \frac{\pi}{n+1}\delta_{nn'}\delta_{ll'}, \tag{16}$$

where δ_{ij} is the Kronecker symbol. The polynomials are represented by two indices, n and l, where n is the degree of the radial polynomial and l is the angular dependence parameter. The numbers n and l are both even or both odd, making n-l always even. There are $(1/2)(n+1)(n+2)$ linearly independent polynomials $Z_n^l(\rho, \theta)$ of degree $\leq n$, one of each pair of numbers n and l.

The polynomials can be separated into two functions [75]

$$Z_n^l(\rho,\theta) = Z_n^{n-2m}(\rho,\theta) = R_n^{n-2m}(\rho)\begin{Bmatrix}\sin\\ \cos\end{Bmatrix}(n-2m)\theta, \tag{17}$$

where the sine function is used when $n-2m > 0$ while the cosine function is used when $n-2m \leq 0$. The degree of the radial polynomial $R_n^l(\rho, \theta)$ is n which can range between $0 \leq m \leq n$. It may be shown that $|l|$ is the minimum exponent of these polynomials. The radial polynomial is given by [72]

$$R_n^{n-2m}(\rho) = \sum_{s=0}^{m}(-1)^s \frac{(n-s)!}{s!(m-s)!(n-m-s)!}\rho^{n-2s}. \tag{18}$$

Any continuous wavefront shape $W(\rho, \theta)$ of degree k may be expressed by a linear combination of the Zernike Polynomials as follows:

$$W(\rho,\theta) = \sum_{n=0}^{k} \sum_{l=0}^{n} R_n^l \left(a_{nl} \cos l\theta + b_{nl} \sin l\theta \right). \tag{19}$$

The advantage of expressing the wavefront by a linear combination of orthogonal polynomials is that the wavefront deviation represented by each term is a best fit or minimum fit variance with respect to the actual wavefront. The practical consequence of the orthogonality of the Zernike polynomials is that any aberration term, like defocus, tilt or any other may be added or subtracted from the wavefront without compromising the best fit to the actual wavefront.

Diffraction

In the ideal situation where a lens has no aberrations, blurring of the spot in the image plane still occurs. This is due to diffraction which is the observable wave property of light when the wavefront is obstructed along its propagation path. The geometrical model that was previously discussed is not adequate to describe wavefront propagation in the immediate vicinity of boundaries that occur in the shadows of these obstructions. These regions are of interest because optical images might also reside in these areas. Wave optics is an approach that is normally used to describe diffraction primarily through the Huygens-Fresnel principle [76].

Diffraction rings can be seen when trying to focus on the aperture of a micro-lens under test. To see how these rings occur we can look at the case in which a uniform plane wave interacts after passing through a circular aperture. This is very prevalent since most apertures in optical systems are circular. The far-field or Fraunhofer diffraction pattern for a uniformly illuminated circular aperture is the well known Airy disk pattern and is

given by

$$E(r,z) \sim \frac{2J_1(2\pi a\theta/\lambda)}{(2\pi a\theta/\lambda)}. \tag{20}$$

Where J_1 is the first order Bessel function. This pattern has a single dominant central lobe surrounded by a series of increasingly weaker circular rings as shown in Figure 28. The Fresnel diffraction patterns for a uniformly illuminated circular aperture consists of a series of circular rings modulating a constant-amplitude background as shown in Figure 28. As one get closer to the aperture the frequency of the Fresnel ripples increase. It is these Fresnel ripples that have the most adverse effects on phase-shifting interferometry. In phase-shifting interferometry one modulates the fringes formed between the test and reference arm by varying the optical path difference between the two by using a devise such as a PZT. Once can recover the phase and hence the surface profile of the optics under test by employing any of the multitude of phase-shifting algorithms. Fresnel ripples can cause these algorithms to report inaccurate surface profiles. To remedy such effects, the exit pupil of the micro-lens under test should always be imaged directly onto the image plane of the CCD camera.

Interference

In the manufacture of micro-structural arrays such as micro-lenses and micro-pyramids it is important to control the manufacturing process. To aid the process engineer in achieving optimum conditions, it is important that he or she can measure both the optical and geometrical properties of these micro-structures. Most of the instruments used in this work to measure the micro-structures are based on the principles of interference.

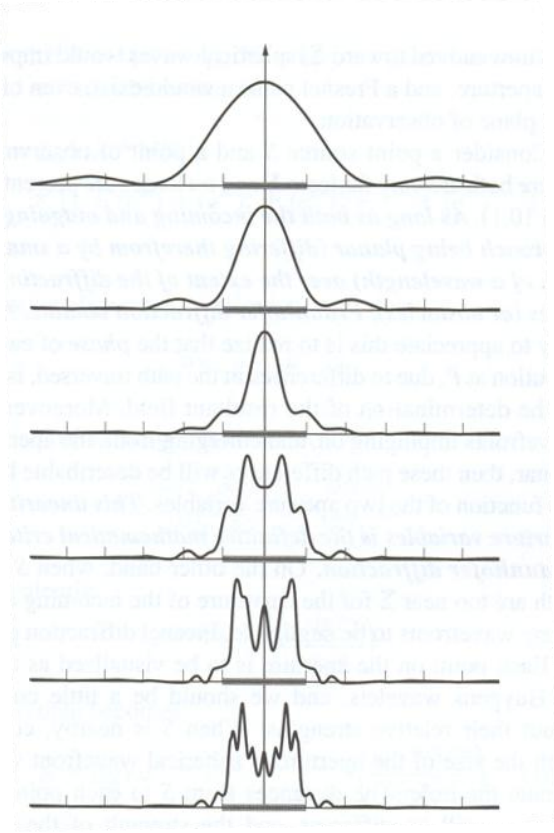

Figure 28: A succession of diffraction patterns at increasing distance from a single slit; Fresnel at the bottom (nearby), going toward Fraunhofer at the top (faraway) [76].

As a lead into the explanation of interference, two important concepts need to be introduced: optical path difference and phase difference.

Optical Path Difference and Phase Difference

The wave velocity of light in a transparent material is different from that in free space and is given by

$$v' = \frac{v}{n}, \tag{21}$$

where n is the refractive index of the transparent material. The optical path difference can be defined as the geometrical path length of a wave multiplied by the refractive index of

the material traversed by the ray. The optical path length between points *a* and *b* in Figure 29 is given by

$$OPD = D_1 + n_2 D_2 + D_3 + n_4 D_4 + D_5 . \tag{22}$$

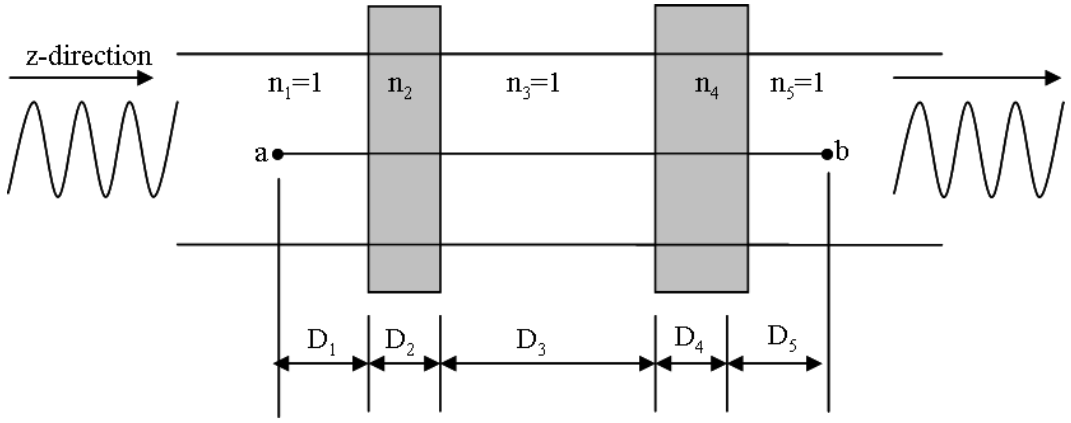

Figure 29: *OPD* between points *a* and *b*.

Let us assume that the phase at point *a* in Figure 29 for a plane wave traveling in the z-direction is given by

$$\phi_1 = kz_1 - 2\pi\nu t + \delta , \tag{23}$$

where *k* is the propagation number and δ is an arbitrary phase offset. The phase at point *b* is given by

$$\phi_2 = kz_2 - 2\pi\nu t + \delta . \tag{24}$$

Hence the phase difference between *a* and *b* is given by

$$\phi_2 - \phi_1 = kOPD . \tag{25}$$

Two-beam Interference

Interference is the superposition (addition) of two waves in space. Typically these two waves originate from the same source and recombine after travelling along different paths. For example consider two waves

$$A_1(z_1,t) = U_1 \cos(\phi_1 - 2\pi\nu t), \tag{26}$$

and

$$A_2(z_2,t) = U_2 \cos(\phi_2 - 2\pi\nu t) \tag{27}$$

.

The resulting wave will simply be

$$A = A_1 + A_2 . \tag{28}$$

For the case where $U_1 = U_2$ and $\varphi_1 \neq \varphi_2$, the intensity of the resultant wave can be observed as

$$I = (A_1 + A_2)^2 = U_1^{\,2} + U_2^{\,2} + 2U_1U_2 \cos(\phi_1 - \phi_2) \tag{29}$$

.

Since $I_1 = U_1^{\,2}$ and $I_2 = U_2^{\,2}$ equation 29 now becomes

$$I = I_1 + I_2 + 2\sqrt{I_1 I_2}\cos\Delta\phi. \tag{30}$$

Hence the measurable quantity irradiance is not only the sum of the intensities but also has an additional term called the interference term which can produce an enhancement or diminution of the intensity through interference.

Phase-Shifting Interferometry

Phase-shifting interferometry (PSI) is by far the most wide-spread technique used to recover the phase difference ($\Delta\varphi$) between two wavefronts in an interferometer. It involves introducing a known phase shift $\delta(t)$ between the reference and sample wavefronts. Hence equation 30 can be written in the following manner

$$I(x,y,t) = I'(x,y) + I''(x,y)\cos[\phi(x,y+\delta(t))], \tag{31}$$

where $I'(x,y) = I_1 + I_2$ is the intensity bias and $I''(x,y) = 2\sqrt{I_1 I_2}$ is half the peak-to-valley intensity modulation.

PSI takes full advantage of today's computing power to rapidly collect high resolution, repeatable and accurate interferometric data. PSI is incorporated by using a CCD camera and frame grabber to capture successive images while the phase of the interference is modulated. Each image will contain intensity values ranging from 0-255 (8-bit camera) which gives you the grey level of each pixel, *I(x, y)*, in the acquired image. A plethora of phase-shifting algorithms can then be implemented to recover the three unknowns *I'*, *I"* and $\Delta\varphi$ [49]. The simplest of these is the three-step algorithm with a phase-shift of 90 degrees:

$$\phi(x,y) = \tan^{-1}\left(\frac{I_3 - I_2}{I_1 - I_2}\right). \tag{32}$$

Figure 30 shows four interferogram with a phase-shift of 90 degrees between them. Notice how interferograms one and three are the complement of each other due to the 180 degree phase-shift between them. The same can be said for interferograms two and four.

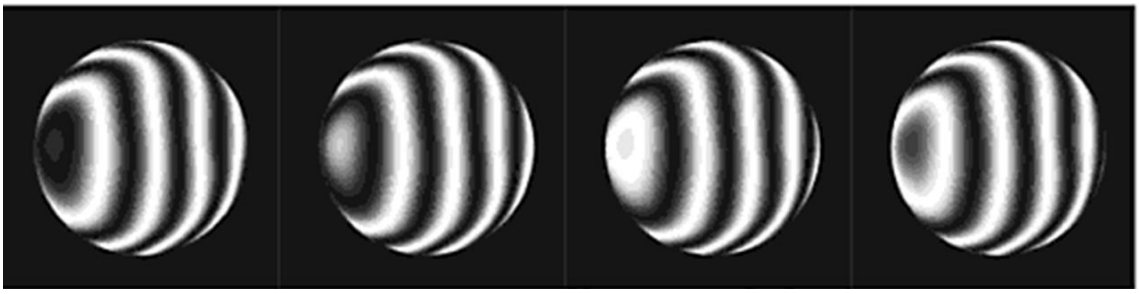

Figure 30: Four interferograms with a phase-shift of 90 degrees between each.

Spatial Sampling

Almost all phase-shifting interferometric tests today produce an interferogram that is imaged onto a sensor, and the intensity pattern is spatially averaged over the sensor's active area during the digitization process. Sampling the interferogram leads to

two major consequences, a reduction in the modulation of the digitized interference pattern and a limitation on resolution.

The modulation reduction is a function of the spatial frequency of the fringes being recorded. The higher the frequency of the fringes, the larger the modulation reduction will be for a given pixel size. The pixel MTF describes the reduction in recorded signal modulation due to the nonzero size of the pixels [49]

$$\text{Pixel MTF} = \sin c(a\xi, b\eta). \tag{33}$$

where a and b is the pixel spacing in the x and y dimension and ξ, η are the spatial frequency coordinates. Figure 31 illustrates the pixel MTFs for sensors with width-to-pitch ratios of 50% and 100%. By using equation 33, one sees that the pixel MTF goes to

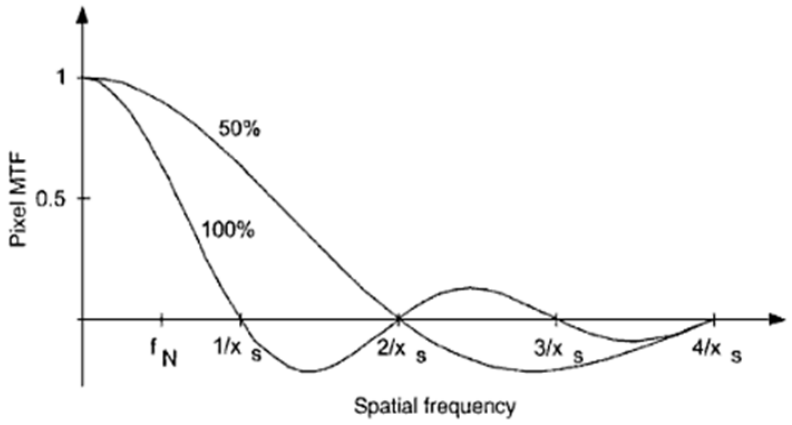

Figure 31: The pixel MTFs for sensors with width-to-pitch ratios of 50 and 100%.

zero at a spatial frequency of *1/a*. Modulation plays an integral part in PSI since the PSI algorithms need a high enough modulation signal to successfully calculate the phase.

Spatial sampling of the interferogram also sets a limit on the resolution which is known as the Nyquist frequency. The Nyquist frequency is defined as half the sampling frequency:

$$f_n(\text{Nyquist frequency}) = \frac{1}{2x_s} \tag{34}$$

where x_s is the spacing of the pixels in the x-direction. Therefore in PSI there needs to be at least two pixels per fringe, which are capable of measuring the high and low points on a fringe. If the fringe frequency exceeds the Nyquist frequency, aliasing occurs and the PSI algorithms cannot interpret the interferogram. As a safe measure in PSI, it is recommended that four pixels per fringe be used to avoid aliasing [49].

Aliasing

Aliasing causes fringe frequencies above the Nyquist frequency to be displayed at frequencies less than the Nyquist frequency. Figure 32 illustrates the unwrapping errors that could be caused by aliasing if a wavefront is sampled at less than the Nyquist frequency.

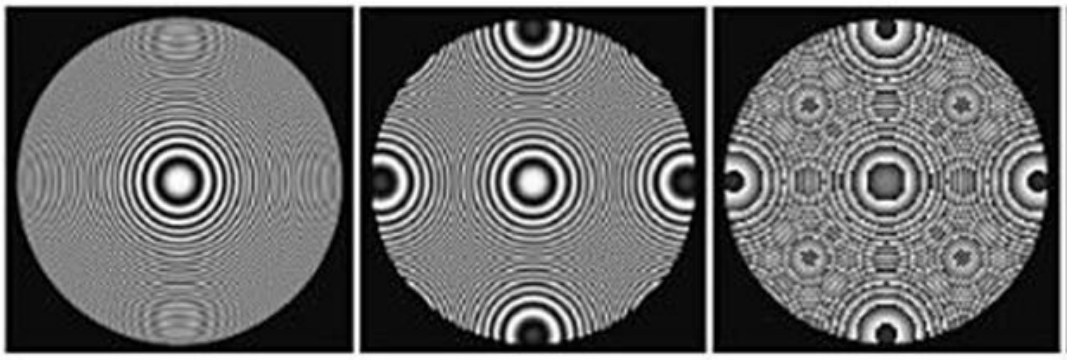

(a) (b) (c)

Figure 32. (a) Sampled interferogram of a defocused wavefront. (b) Under-sampled interferogram showing aliasing. (c) Unwrapped phase map of (b) [49].

Phase Unwrapping

Phase unwrapping is a necessary step in the recovery the surface profile of an object under test by PSI methods. This is because the arctangent function in equation 32 only produces phase values between $-\pi/2$ and $\pi/2$ at each pixel. Hence, the phase has to

be extended in the range from 0 to 2π since we know the surface is continuous and extends over a larger range. This can be done since the signs of the since and cosine function are known independently of the tangent [49]. After the phase values are converted from 0 to 2π, the final step is to unwrap the 2π discontinuities into a continuous representation of the wavefront under test. This process is illustrated for one-dimensional data in Figure 33.

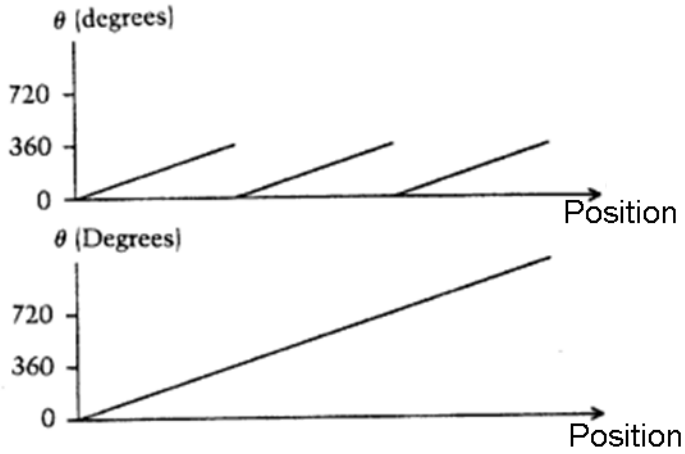

Figure 33: The phase unwrapping process in one dimension.

Aspherical Surfaces

Aspherics are optical elements that have either one or both surfaces that are neither planar nor spherical. It has been shown using Fermat's principle that aspherics are well suited in transforming a spherical wave into a plane wave and vice-versa [77]. Aspheric elements are able to minimize aberrations caused by and inherent to spherical optical elements. Fewer elements are needed, making systems smaller, lighter and shorter. This has led to frequent use in optical systems, such as cameras, projectors, telescopes and eyeglasses as a means of correcting imaging errors. Although they are

well suited to certain applications, aspheric surfaces are still difficult to manufacture as well as test [78].

Most aspheres manufactured today are rotationally symmetric. If we take the z-axis as the axis of revolution, the surface can be defined as:

$$z = \frac{cS^2}{1+\left[1-(K+1)c^2S^2\right]^{1/2}} + A_1S^4 + A_2S^6 + A_3S^8 + A_4S^{10} \tag{35}$$

,

where $S^2 = x^2 + y^2$ and $c = 1/r$, where r, is the base radius of curvature. A_1, A_2, A_3, A_4, are the aspheric deformation coefficients, and K is the conic constant. If the aspheric coefficients are zero, the surface is a conic surface of revolution, and is categorized as follows [79]:

Table 3: Conic Sections

Hyperboloid	K < -1
Paraboloid	K = -1
Ellipsoid	-1 < K < 0
Sphere	K = 0
Oblate Spheroid	K > 0

Aspheric elements give the optical design engineer greater freedom to design high quality optical systems. This though comes at a price, since aspheric elements are quite expensive to manufacture. Due to an advance in asphere manufacturability, aspheric optics has become more widespread, as designers push the limits of performance. The most popular techniques for manufacturing aspheres are injection molding, diamond-turning and reactive ion etching [80, 81]. Molding tends to produce aspheres with a high

quality finish and is therefore suitable for visible optic applications such as imaging (digital cameras). Diamond-turning by computer control produces aspheres which may need additional polishing by grinding or magnetorheological finishing [81]. Diamond-turning techniques have primarily been used for infra-red applications.

Aspheric metrology is limited to a number of special techniques which can be broken down into three main categories: physical measurements, reflection testing and transmission testing. Co-ordinate measuring machines and profilometry fall under the physical measurement category because the probe or stylus is in contact with the aspheric surface under test. Reflection or transmission testing can be implemented with a Twyman-Green or Fizeau interferometer [82]. These interferometric methods were originally developed for the testing of spherical optics and could be adapted to measure aspheres with the use of auxiliary optics such as computer generated holograms (CGH). CGHs are expensive to manufacture and also have to be tested before being implemented into an interferometric setup. For this reason, CGHs should only be contemplated if the departure of the aspheric surface from a best fitting sphere is too large to be handled by a traditional confocal test configuration [83]. This occurs if the departure causes many fringes in the interferogram which then violates the Nyquist theorem. Typically, these interferometric systems can only handle 10-20 fringes of aspheric departure [49]. Figure 34 demonstrates a CGH in use for testing an aspheric lens in reflection. There are other more exotic aspheric testing methodologies such as the sub-aperture stitching interferometer which is used to overcome fringe density due to high local slope [83].

It should be noted that the interferometric tests described above are well suited for large scale aspheres (> 5 mm). Micro-lens array that incorporate aspheres are normally

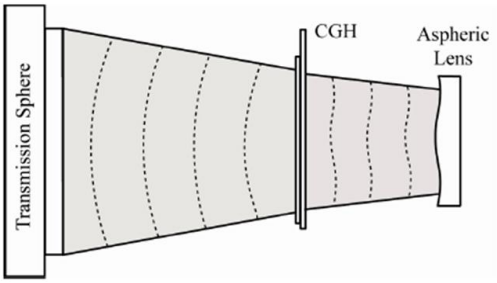

Figure 34: CGH in reflection testing of aspheric lens.

tested by conventional interferometers (TWG and MZ) that have been specially adapted to measure micro-optics. These interferometers will be described in further detail in Chapter 3 and work best for mild aspheres with departure from a base sphere on the order of a few microns.

Retrace Errors

Most interferometric test are null tests in which the goal is to create a wavefront that matches the test surface, mostly by the use of a high quality microscope objective, so that the wavefront is normally incident everywhere on the test surface. The reflected light as in the case for a TWG interferometer retraces the incident path, and a null interferogram (no fringes in the field of view) results. These tests are normally implemented to test spherical optics, since a high quality microscope objective can produce a near-perfect spherical wavefront.

Non-null interferometers are generally used to test aspheric surfaces when a part specific CGH is deemed to expensive. These aspheric surfaces tend to have a small departure from a sphere and hence the test and incident wavefront will not match and interference fringes result. The light is no longer normally incident on the aspheric surface, and does not follow the same path back through the interferometer. The wavefront then is altered on the return path and induces part-dependent aberrations to the

test wavefront. These induced aberrations are commonly referred to as retrace errors. The greater the departure is from a sphere, the greater the re-trace error.

Simulations have been performed that intentionally introduced tilt, power and spherical aberration into a TWG interferometer test wavefront for which the measurement error was calculated [84]. It has also been shown experimentally that intentionally defocusing a sphere to produce large departures from a reference sphere introduced significant aberrations with an rms error up to 3.5% of the total wavefront departure [85].

In order to obtain accurate results when employing non-null interferometric tests, the induced aberration must be removed. Methods have been developed to compensate for re-trace errors in aspherics with several microns of departure from a sphere. These methods reduced uncorrected errors exceeding 50 nm to errors less than 10nm in magnitude [86]. In other methods, third-order analytic expressions were derived for retrace errors generated by a tilted or defocused test surface. The expressions were tested with a specially built interferometer [87]. The most complete method to compensate for re-trace errors is via reverse ray-tracing. This technique involves tracing rays back from the detector or image plane through the system to the test plane to determine the surface figure. This can be done with ray-trace software such as Zemax or Code V, and requires precise knowledge of the interferometer set-up. For commercial systems this is almost impossible since optical details are not available for proprietary components. For non-commercial systems, some parameters can be independently tested, but absolute part locations are still difficult to measure. Reverse optimization can be used to calculate the interferometer specifications. This is implemented by first measuring a well known part

with the interferometer. By using the interferometer parameters as variables in the ray-tracing package, the system parameters can be optimized to give the desired test wavefront, and hence find the best description of the interferometer. Reverse optimization in conjunction with reverse ray-tracing was used to calibrate non-null interferometer for a wavefront with more than 200 waves of departure to an accuracy of 0.16 waves PV and 0.02 waves rms [88].

The index-liquid technique is a non-null test since the wavefront from the test part is essentially spherical and differs from the wave-front in the test arm which is planar. This creates interference fringes which includes those due to re-trace errors. In the error analysis section we will demonstrate the magnitude of these re-trace errors for a micro-lens tested in a MZ configuration and how we go about calibrating for it.

Roughness, Form and Waviness

There are a variety of manufacturing methods that can be used to make micro-structures such as micro-lenses and micro-pyramids [89, 90]. The manufacturing method chosen is highly dependent on the application for which the micro-structure will be used. Each manufacturing process needs to be highly controlled since any variation can affect the surface texture which in turn affects the performance of the part. For instance, in reactive ion etching of micro-lens arrays if the etch rate is not controlled appropriately, the surface shape deviates from the intended shape causing changes in the radius of curvature of the lenses. In the data-com industry the radius of curvature of these micro-lens arrays is of critical importance to the performance of the high bandwidth data networks.

The main elements of surface texture are roughness, waviness and form. Roughness is defined as the irregularities which are inherent in the manufacturing process and is produced only by the method of manufacture resulting from the process rather than the machine [91]. Waviness is defined as that part of the texture on which roughness is superimposed. It may result from vibrations, chatter or work deflections and strains in the material [91]. Form is defined as the general shape of the surface, ignoring variations due to roughness and waviness. It should be noted that these three characteristics are never found in isolation. Most surfaces are the result of a combination of the effects of roughness, waviness and form [91]. Figure 35 depicts a surface profile which represents the combined effects of roughness, waviness and form.

Faceted Micro-Structure Geometry

Faceted micro-structures such as micro-triangle corner and micro-square corner arrays operate on the principles of reflection and refraction. Which principle is used depends on the application. For instance, micro-triangle corner arrays (MTCCA) that are used as brightness enhancers for LCDs operate on the principles of reflection (also total internal reflection) and refraction whereas micro-square-corner cube arrays (MSCCA) that are used in road-safety-applications rely solely the principle of reflection (retro-reflection). Figure 36 illustrates the two types of micro-cube-corner arrays (MCCA). Retro-reflection is the process in which light is reflected back to the source with a minimum scattering of light. Figure 37 illustrates the concept of retro-reflection in a MTCCA structure. In this case the retro-refection involves mirror reflections from three mutually orthogonal surfaces that are back-sides of prisms. Additionally there is refraction as light enters and leaves the plastic medium in which the prisms are formed.

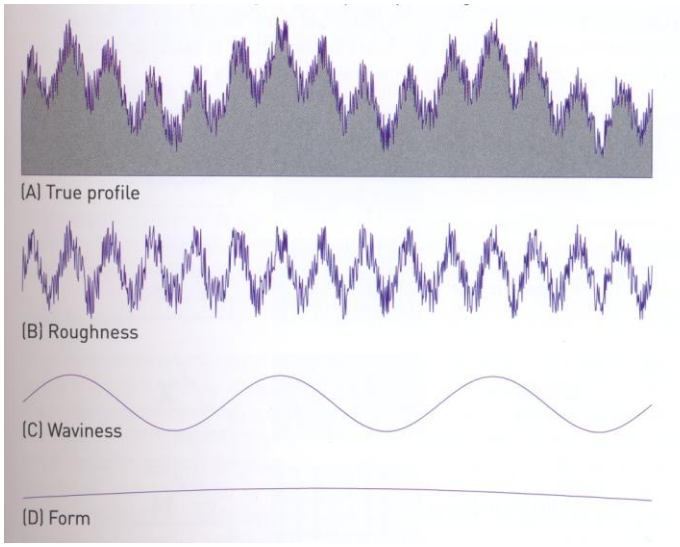

Figure 35: A surface profile represents the combined effects of roughness, waviness and form [91].

Retro-reflection in micro-cube-corner arrays (MCCA) tend to have higher retro-reflectivity, smaller divergence and are harder to fabricate than competing technologies such as micro-sphere arrays [93]. The major advantage of MSCCA over MTCCA has to do with the fact that the available surface area (effective aperture) for MSCCA is greater than that for MTCCA. This leads to greater reflection efficiency for MSCCA when compared to MTCCA. This effect of geometry on reflection efficiency is depicted in

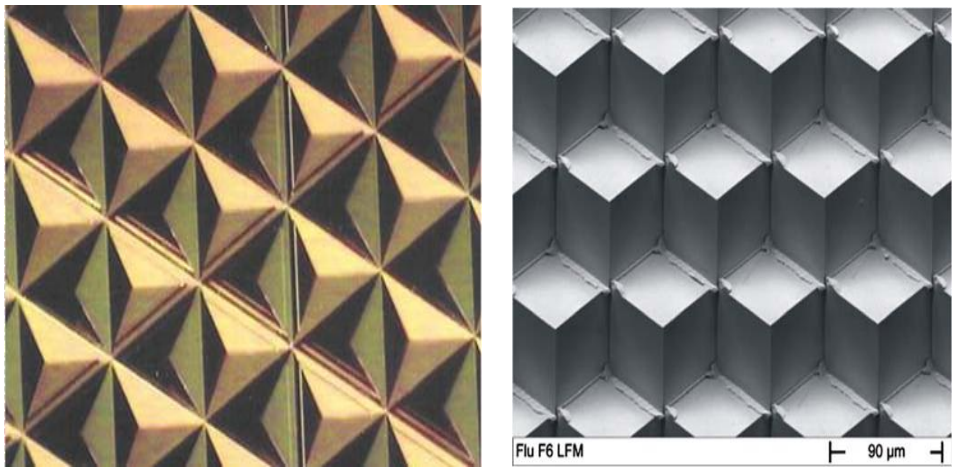

Figure 36: (a) The structure of MTCCA. (b) The structure of MSCCA.

Figure 38. For angles of incidence equal to zero degrees the reflection efficiency for MSCCA is 100% whereas a MTCCA obtains not more than 66 % [94]. One also notices in Figure 38 that the effective aperture of the MTCCA is limited to a hexagon, hence the rest of the aperture appears black which means it is wasted. For the MSCCA the whole surface area of the MSCCA appears bright as it completely reflects the incoming light beam [94]. To achieve higher reflection efficiency the structure size, the facet angle and the surface quality of the micro-pyramids are all important parameters that need to be tightly controlled.

By far the most widespread use of micro-pyramid arrays are as brightness enhancers for liquid crystal displays (LCD) in consumer electronic devices such as laptop computers, personal TVs and camcorders. These micro-pyramidal arrays fall under the category of MTCCA and are generally made of plastic materials that are optically transparent. These micro-pyramids can save unnecessary power consumption by redirecting and redistributing the incident light coming from the back side of the films to the front side. It has been shown that up to 20% brightness enhancement with front viewing angles of ±35 degrees can be achieved [95]. Figure 39 illustrates the optical principle of the pyramid shaped structure. The emitted light can be divided into three categories: a) direct recycle, b) effective refraction and (c) indirect recycle [95]. Direct recycle occurs when the light in reflected back and recycled. Effective refraction occurs when the light is refracted out to the front of the pyramid. Indirect recycle occurs when both reflection and refraction at the pyramid faces causing the light to travel through and be recycled by another pyramid. The most common type of micro-pyramids used as

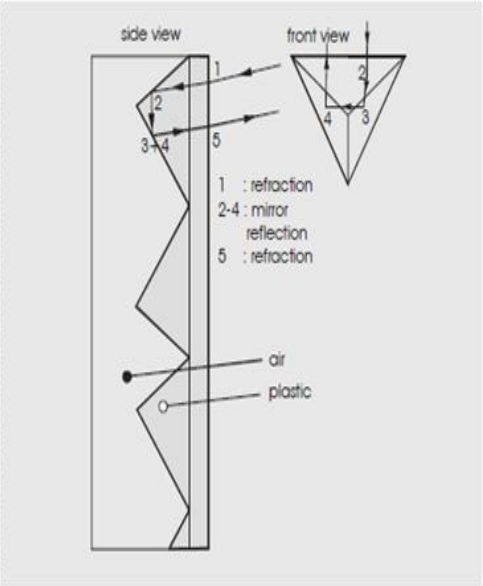

Figure 37: Retro-reflection in a micro-prismatic sheeting [92].

brightness enhancers are right pyramids whose base is a regular polygon. An example of this type of micro-pyramid is a square pyramid whose base has four sides and comprises four equilateral triangles is illustrated in Figure 40. A special case of a regular pyramid having equilateral triangles as sides and an equilateral triangle as a base is known as a tetrahedron (Figure 40). Table 4 describes the parameters and the corresponding formulas for the pyramids illustrated in Figure 40.

Index Liquid Metrology

As mentioned previously, index liquid metrology extends the dynamic range of phase-shifting interferometry. Our approach is to place a liquid with a specific refractive index next to a microlens or micro-structure array, as shown in Figure 41, and to use the measured phase profile of the exiting wave front to determine important microlens parameters such as, sag, radius of curvature, deviation from sphere, wavefront aberrations and focal length. For microstructure arrays, we are primarily concerned with calculating the height and facet angles.

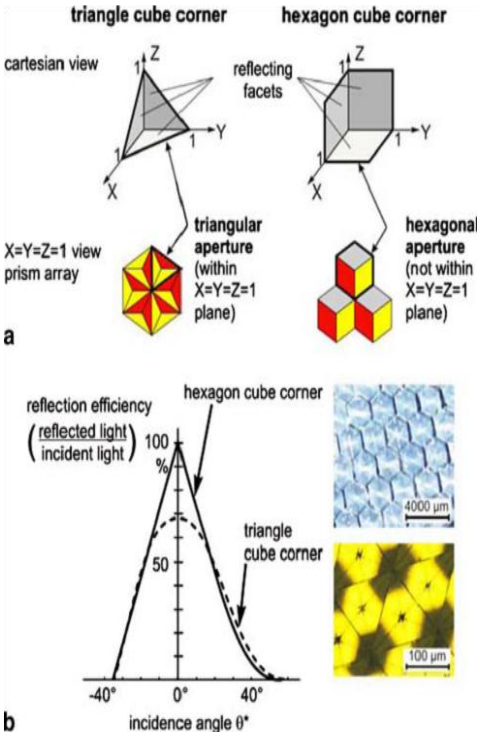

Figure 38: Geometric and effective aperture [94].

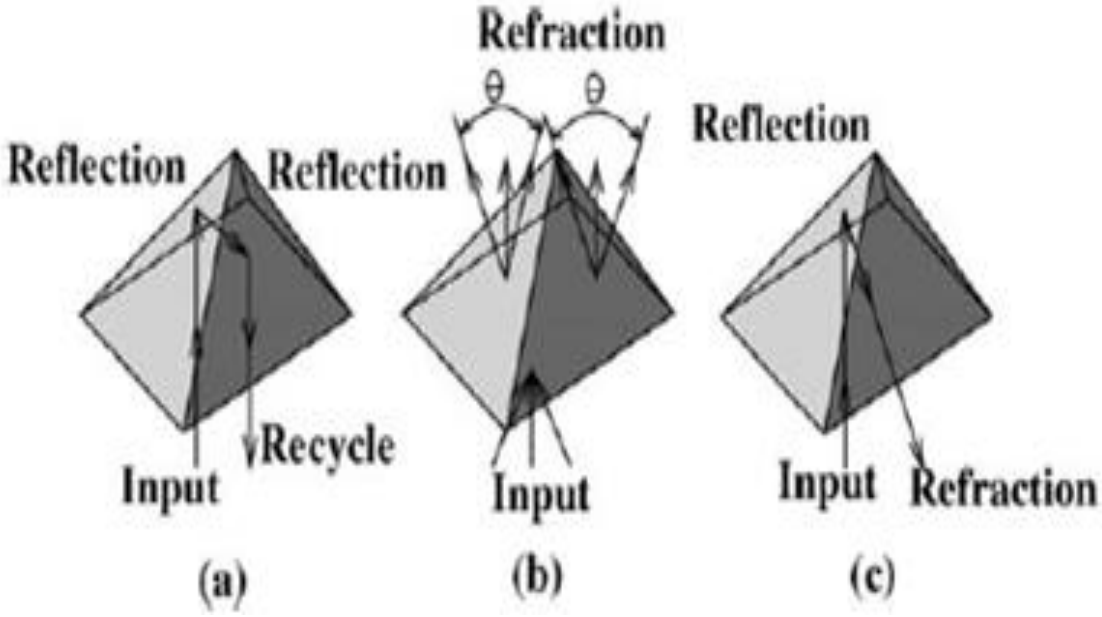

Figure 39: The optical principle showing the three possible cases of the emitted light: (a) direct recycle; (b) effective refraction; (c) indirect recycle [95].

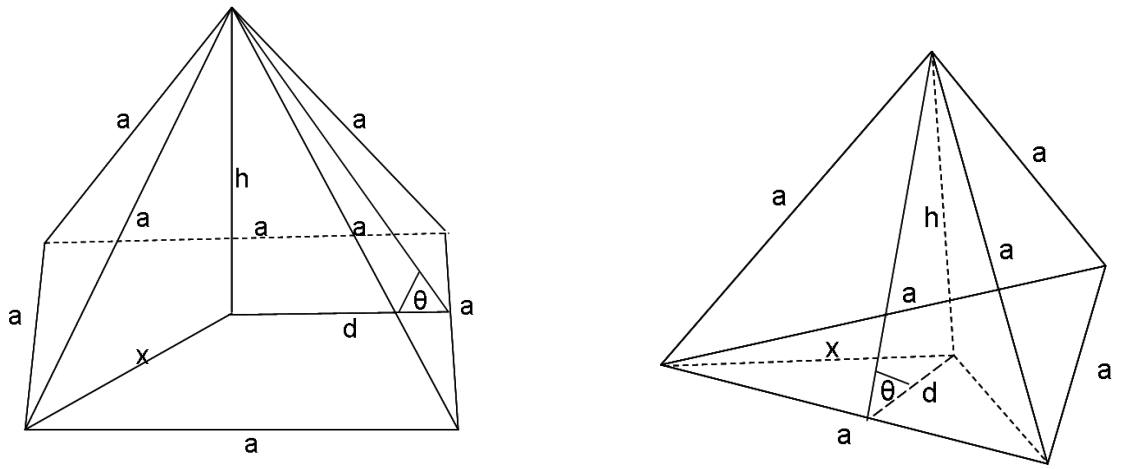

Figure 40: (a) Square Pyramid. (b) Tetrahedron.

Table 4: Micro-pyramidal array parameters.

Parameter	Description	Square Pyramid	Tetrahedron
a	Length of pyramid side	*a*	*a*
x	Distance from center to vertex edge	$\frac{a}{\sqrt{2}}$	$\frac{1}{3}\sqrt{3}a$
d	Distance from perpendicular bisector of *a* to center	$\frac{a}{2}$	$\frac{1}{6}\sqrt{3}a$
h	Height of pyramid	$\frac{a}{\sqrt{2}}$	$\frac{1}{3}\sqrt{6}a$
θ	Angle between pyramid face and pyramid base otherwise known as facet angle.	54.74	70.53

When a collimated wave front passes through the micro-pyramid, refraction and therefore distortion of the wavefront occurs at the microlens boundary and this is reduced

compared to refraction with an air boundary. By controlling and reducing this refraction, the transmitted wave can be interferometrically measured against a plane wave. Take the refractive index of the micro-lens as n_2 and the refractive index of the liquid as n_1, as shown in Figure 41. The optical path length at the vertex of the microlens is given by

$$OPL_0 = n_1 t_1 + n_1 h \tag{36}$$

where t_1 is the thickness of the substrate and h is the sag of the micro-lens. The optical path length for the arbitrary ray shown is given by

$$OPL(x,y) = n_1 t_1 + n_1 h(x,y) + n_2 L(x,y) \tag{37}$$

where L is the distance from the point of refraction to the index liquid-air interface. The optical path difference between these two rays is therefore given by

$$OPD = n_1(h(x,y) - h) + n_2 L(x,y) \tag{38}$$

.

Solving for $L(x, y)$ in equation 38 we get

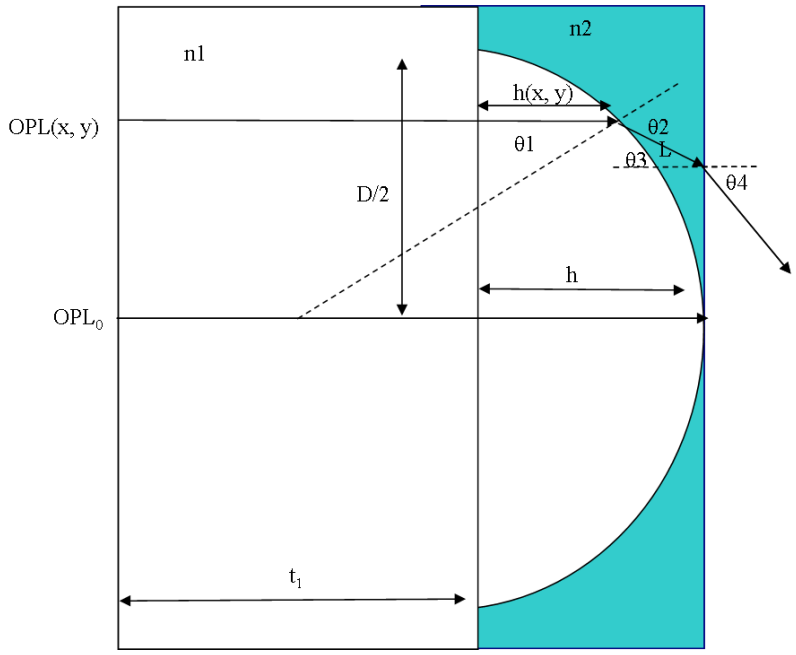

Figure 41: Schematic of the measurement principle for a micro-lens.

$$L(x,y) = \frac{OPD - n_1\left(h(x,y) - h\right)}{n_2}. \tag{39}$$

From the figure above we know

$$h = h(x,y) + L(x,y)\cos\theta_3, \tag{40}$$

substituting equation 39 into equation 40 gives

$$h = h(x,y) + \left(\frac{OPD - n_1\left(h(x,y) - h\right)}{n_2}\right)\left(\cos\theta_3\right). \tag{41}$$

After some rearranging we get

$$h - h(x,y) = \frac{OPD\cos\theta_3}{n_2 - n_1\cos\theta_3}. \tag{42}$$

Now if we assume the sag is the difference between the rays at the edge of the aperture and the rays at the vertex, then the above equation is

$$sag\left(x,y\right) = \frac{OPD\left(x,y\right)\cos\theta_3\left(x,y\right)}{n_2 - n_1\cos\theta_3\left(x,y\right)}, \tag{43}$$

where θ_3 from Snell's law is given as

$$\theta_3\left(x,y\right) = \sin^{-1}\left(\frac{\sin\left(\theta_4\left(x,y\right)\right)}{n_2}\right). \tag{44}$$

Hence, to recover the surface profile of the micro-lens under test, *sag (x, y)*, we need to know the index of refraction of the micro-lens under test (n_1), the index of the liquid (n_2) and $\theta_4(x, y)$, which is the angle (slope) at each point on the exiting wave front. The interferometric measurement directly gives us $\theta_4(x, y)$. By implementing phase-shifting techniques [49], we can recover the phase profile and hence the surface profile of the micro-lens under test by using the following equation;

$$OPD(x,y) = \frac{\lambda\phi(x,y)}{2\pi}, \tag{45}$$

where $\varphi(x, y)$ is the phase at a point on the wavefront exiting the micro-pyramid structure, λ is the wavelength of the laser source used, and *OPD* is the optical path difference introduced by the micro-lens. The slope of the exiting wavefront at each point, $\theta_4(x, y)$), can then be calculated directly from the gradient of the optical path difference as

$$\theta_4(x,y) = a\tan^{-1}\left(\nabla OPD(x,y)\right). \tag{46}$$

In the limit where rays are impinging close to the optical axis (n_2 nearly matches n_1), the angle $\theta_4 \approx \theta_3 \approx 0$ hence $\cos(\theta_3)$ goes to 1 and equation 43 reduces to

$$sag(x,y) = \frac{OPD(x,y)}{n_2 - n_1}. \tag{47}$$

Equation 47 represents the first order theory in index metrology in which the surface profile of the micro-lens can be obtained by measuring the phase profile in waves and then scaling by the refractive index difference and wavelength to convert to height. To achieve maximum accuracy refraction must be considered as was shown in equations 36-46. There are other higher-order effects such as retrace errors from the non-null fringe condition [96, 97, 98]. Interferometer bias, inhomogeneity, and substrate form error are also issues, but less of a concern for testing micro-lenses where the spatial variation of such errors is, in general, larger than the length scale of the micro-structures themselves. These errors will be discussed in more detail in the error analysis section. It must be mentioned that equation 43 holds for the sample orientation shown in Figure 41, for index liquids larger or smaller in refractive index than that of the sample, since the cosine function is even. If the sample is flipped, equation 43 becomes

$$sag = \frac{OPD\cos\theta_3}{n_2\cos\theta_3 - n_1}. \tag{48}$$

Therefore it is important to know which orientation the sample is placed in before analyzing the results with either equation 43 or 48. In order to measure faceted structures such as micro-pyramids the same steps applies as in the case of micro-lenses but in this case we focus on the facet angle calculation. Take the refractive index of the micro-pyramid as n_2 and the refractive index of the liquid as n_1, as shown in Figure 42. Using Snell's Law, we get

$$n_1 \sin\theta_1 = n_2 \sin\theta_2, \tag{49}$$

$$n_2 \sin\theta_3 = n_3 \sin\theta_4 \tag{50}$$

and

$$\theta_2 = \theta_1 + \theta_3. \tag{51}$$

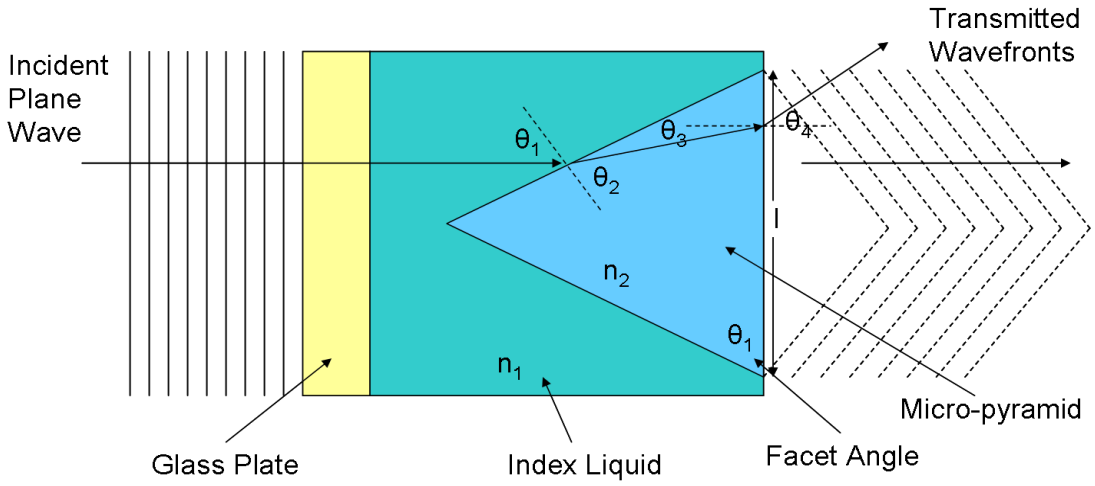

Figure 42: Micro-pyramid measurement principle.

Substituting equation 51 into equation 49 gives

$$n_1 \sin\theta_1 = n_2 \sin(\theta_1 + \theta_3). \tag{52}$$

By using the sum and difference formulas, we can expand equation 52 to get

$$n_1 \sin\theta_1 = n_2 \sin\theta_1 \cos\theta_3 + n_2 \cos\theta_1 \sin\theta_3. \tag{53}$$

Dividing equation 53 through by $cos\theta_1$, we have

$$n_1 \tan\theta_1 = n_2 \tan\theta_1 \cos\theta_3 + n_2 \sin\theta_3. \tag{54}$$

By solving for the facet angle (θ_1), we finally have

$$\theta_1 = \tan^{-1}\left(\frac{n_2 \sin\theta_3}{n_1 - n_2 \cos\theta_3}\right), \tag{55}$$

where

$$\theta_3 = \sin^{-1}\left(\frac{\sin\theta_4}{n_2}\right). \tag{56}$$

Hence, to recover the facet angle of the micro-pyramid under test, θ_1, we need to know the index of refraction of the micro-pyramid under test (n_2), the index of the liquid (n_1) and θ_4, which is the angle (slope) of the exiting wave front. The interferometric measurement directly gives us θ_4. The *OPD* and slope of the exiting wavefront (θ_4) is found in exactly the same way as in equations 45 and 46. As was also the case for the micro-lens the orientation should be taken into consideration before applying the appropriate equations.

Sensitivity vs. Fringe Density

The index liquid that is chosen will depend heavily on what characteristic of the micro-optics need to be tested. This is because the index liquid puts a threshold on the sensitivity of the index liquid technique due to refraction. If the index of the liquid is very different from the micro-optic refractive index, the refraction is strong at the index liquid-micro-optic boundary and the wavefront is significantly distorted and not measurable with interference against a plane wave. In the same way if the index liquid has a

refractive index that is too similar to that of the micro-optic, little refraction occurs and the wavefront is not distorted enough. Hence, the index liquid must be chosen carefully. The larger the refraction, the higher the sensitivity to form errors on the lens, yet the larger the refraction the more difficult it is to resolve the dense interference fringes. Hence, if the index liquid technique is used purely to measure the height of a micro-lens or pyramid, then one can use an index liquid that closely matches that of the part under test. If on the other hand form errors or defects on the order of a fraction of a wavelength are to be measured on a micro-lens, using an index liquid that gives the highest density of fringes without violating the Nyquist limit is recommended.

To bring these ideas sharply into focus, we can use equation 47 to model the maximum allowable sag of the microlens and the minimum surface figure error that we can resolve to estimate which index liquid should be chosen. If we assume that our camera has a resolution of 640 x 480 pixels and that the entire lens under test (λ = 0.6328 μm) occupies the entire field of view, then according to the Nyquist theorem (at least 4 pixels per fringe for PSI), one can resolve 60 fringes from the center of the lens out to the edge of the lens, then equation 47 becomes

$$sag(x,y) = \frac{38\mu m}{n_2 - n_1}. \tag{57}$$

Using n_1 as 1.50, we can plot a graph of the maximum sag that can be measured versus the refractive index of the liquid n_2. This graph is illustrated in Figure 43, which clearly illustrates that we can measure a microlens with a larger sag the closer the refractive index of the liquid matches that of the microlens under test. If one knows the approximate To investigate the minimum measurable surface feature, lets assume that we have an 8 bit

analog to digital converter that capture our interference patterns. Using PSI techniques this divides the gray level of the interference pattern into 256 discrete levels. Hence, theoretically speaking PSI allows one to resolve a fractional fringe to 1/256. There will obviously be quantization errors in the in the digitization process, hence in practice a fringe resolution of 1/100 of a fringe (6nm) is reasonable [99]. Modeling equation 47

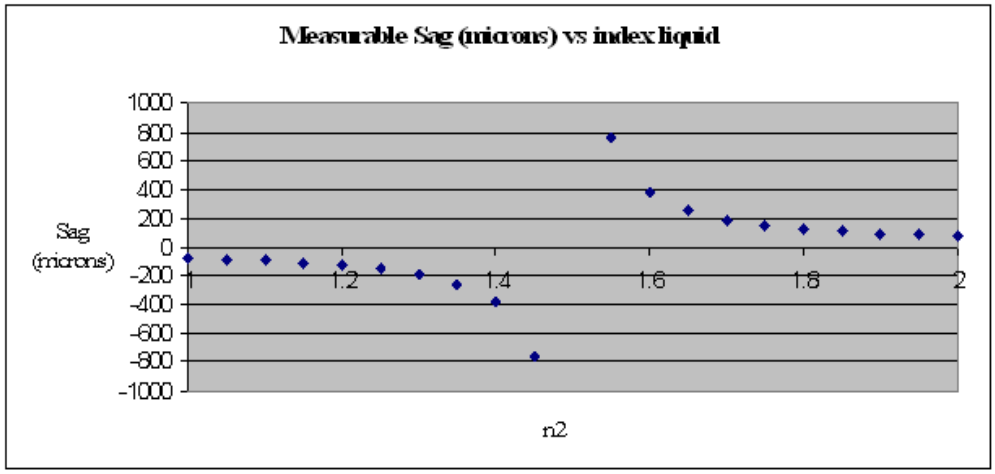

Figure 43: Maximum measurable sag vs. refractive index of index liquid.

again, we find the minimum resolvable feature is given by

$$sag(x,y) = \frac{6nm}{n_2 - n_1}. \tag{58}$$

Figure 44 shows a plot of the minimum resolvable feature versus the refractive index of the liquid. The analysis shows that larger features are measurable with a larger index mismatch. Conversely, a smaller index mismatch reduces the sensitivity of the index liquid technique. It should also be noted that although the sag of the lens determines the number of fringes seen across the lens aperture, the slope of the lens determines the fringe spacing. Therefore, the higher the slope of the micro-lens surface the greater the fringe density. Aspheric micro-lens arrays have generally greater slopes than spherical

micro-lens arrays so special attention must be paid to aspheric micro-lens whether testing in transmission or reflection.

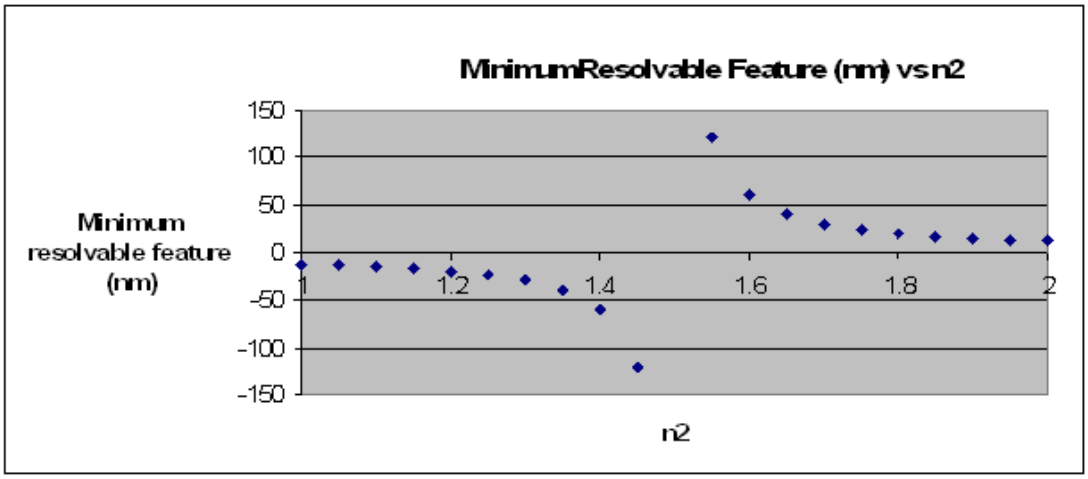

Figure 44: Minimum resolvable feature vs. index liquid.

Index Liquids

There are many index matching materials available. They include optical fluids, optical gels and optical thermosets. Optical fluids (index liquids) are the most convenient to apply particularly for temporary use in testing and prototyping. The disadvantage with optical fluids is that they tend to flow-out from the optical interface unless properly contained with a seal. Optical gels are non-migrating and do not require containment seals but lack the range of indices available in index liquids. Optical thermosets are soft plastics which, when cured provide dimensional rigidity. Optical thermosets also lack the availability in index of index liquids. It is for this reason along with cost that led to the choice on index liquids as our index material of choice.

Index liquids used in this experiment were obtained from Cargille Laboratories, the number one source for optical liquids. Their refractive index liquids come in ¼ fl. oz. bottles which range in index from 1.3000 to 2.31 in .002 index intervals with an

uncertainty of ±0.0002. These liquids are specified at a wavelength of 589.3nm at a temperature of 25^0C. Because index liquids are less stable than gels or thermosets, particular attention must be paid to an index liquid's thermal coefficient as well as evaporation [100].

Cargille Laboratories specifies its index liquids of have a thermal coefficient of -0.00004 refractive index units per degree centigrade. Hence the temperature where these index liquids are stored should be monitored closely. Evaporation can also impact the refractive index of an index liquid, since most of these liquids are mixtures of substances with different refractive indices and different volatilities. Hence, if the more volatile material evaporates it will lead to a change in the refractive index of the mixture, since the proportion of components in the mixture changes. Cargille Laboratories remedies this by using liquids in their mixtures with very low and balanced volatility. It is for these reasons that oil based liquids are preferred to water-based liquids [100].

The refractive index of liquids also varies with wavelength. This variation is called refractive dispersion. For index liquids, as the wavelength increases, the refractive index goes down. Also, the higher the refractive index of the liquid the higher the dispersion. For interferometric testing, a HeNe laser is used with a wavelength of 0.6328 μm, which is in the visible spectrum and hence will have a very high transmittance through most optical liquids. The laser is also low powered hence heating and thermal breakdown in the liquid is avoided. Sunlight also causes optical liquids to become dark over time since they absorb UV, but Cargille Laboratories specializes in light-insensitive index liquids. Even so, index liquids should be stored in a dark place in a dark amber glass bottle and used under low power or with wavelengths that will not affect it. Lastly

light scatter is common in liquids with high molecular weight, but the amount of light lost to scatter is very negligible in nearly all Cargille optical liquids [100].

The most important physical properties of index liquids are viscosity, surface tension and adhesion. High viscosity index liquids are less likely to run than low viscosity index liquids. On the other hand, low viscosity index liquids take less time to reach a stable temperature than high viscosity index liquids. The balance of the surface tension with the adhesion properties can affect the performance of the index liquid [100]. For instance, low surface tension and high adhesion may cause to flow to unwanted areas in the test set-up. It is important to take both the optical and physical properties of optical liquids into consideration before using them in experimental conditions.

Because index liquids need to be in physical contact with the micro-optic surface under test it is important to discuss compatibility and clean up. Most optical liquids are compatible with optical polymers (Su8, PMMA, polycarbonate), and glasses (fused silica, BK7). Index liquids supplied by Cargille Laboratories that are above 1.8 may contain sulphur and arsenic tribromide which is corrosive and may be incompatible with ester-vulnerable plastics and elastomers [100]. All index liquids may be removed from optical surfaces by first wiping off excess fluid with a suitable cloth wipe and then using a suitable reagent grade solvent. Most optical liquids can be removed with isopropanol, or acetone. Use caution when using acetone for clean-up; some optical plastics are incompatible with acetone. Purosol, a molecular lens cleaner sold by most optics catalogs, has been found to remove index liquids very effectively. It is environmentally safe and made from a non-toxic formula.

CHAPTER 3: MICROSTRUCTURE TESTING

Microstructure testing is an essential step in order for the manufacturing engineer to fine-tune his process. Parameters such as surface profile, focal length, wavefront aberrations are very important and need to be characterized in the case of micro-lens arrays. Micro-pyramid height, facet angle and surface quality are also very important factors when testing micro-pyramids. In this chapter we discuss the measurement instruments needed to characterize the geometrical and optical parameters of microstructures measured in this dissertation. Special attention is paid to the Mach-Zehnder phase-shifting interferometer because it is primarily used to implement the index liquid technique. The TWG interferometer as well as an optical non-profiler are discussed and used to compare results obtained with the index liquid for micro-lens measurements. Lastly, we describe contact stylus profilometer as a means for comparing facet angle geometry of micro-pyramids to that obtained with the index liquid technique.

Mach-Zehnder Interferometer

Although reflected light test geometries such as the Twyman-Green interferometer (TWG) has been traditionally used to measure the radius of curvature and departure from a sphere for micro-lenses, the Mach Zehnder (MZ) interferometer has been preferred when inspecting the wavefront aberrations of micro-lenses for a number of reasons. Although the TWG is more sensitive to very small aberrations due to its double-

pass configuration, in the specific case of testing microlenses which has only a single surface bent to obtain optical power, the interferometer bias has a main contribution from retrace error [101]. Also, the MZ interferometer is less prone to parasitic fringes, due to the fact that light will have to be reflected twice at glass surfaces in the instrument in order to be scattered in the forward direction and hence interfere with the test wavefront [60]. Hence, the intensity of these spurious reflections is markedly reduced when compared to parasitic fringes occurring in the TWG interferometer. Partial coherent illumination is normally used to smooth fringes seen in a TWG interferometer. This causes a reduction in interference between test and reference beams when inspecting the cat's eye position in a TWG interferometer, since at the cat's eye position the wavefront symmetry is inverted [65]. The MZ interferometer does not suffer from inversion symmetry due to its single pass configuration, hence coherent sources can be implemented. Additionally, the MZ interferometer can be used to measure the phase lag for slow lenses (NA<0.05) and hence the back focal length with out violating the Nyquist sampling theorem [60]. Lastly, because of the small apertures of micro-lenses under test in a TWG interferometer, a diffraction pattern is superimposed on the interference pattern, sometimes making quantitative analysis impossible. This is because when the light passes through the microlens twice, the aperture of the microlens cannot be clearly imaged onto the camera, and Fresnel diffraction effects are encountered [102].

The MZ interferometer that was used to test the majority of microstructures mention in this dissertation was built by Joaness Schwider from Erlangen University. It was built into a commercial microscope from Carl Zeiss Jena, hence a fiber-based system was seen as the best solution for implementation. A schematic of the MZ interferometer

is shown in Figure 45. The HeNe-laser (0.6382 μm) outputs a beam that is split by a polarizing beam splitter (PBS) and a half wave plate (HWP) at the entrance to enable balancing of the two interfering beams. The fibers used in the test and reference arms are of the polarization-maintaining type in order to preserve the integrity of the polarization and hence maintain the contrast of the interference fringes [101]. The second beam splitter is non-polarizing, hence, the two beams can be forced to interfere by rotating the reference by 90 degrees. This is controlled by twisting the end of the fiber, and with the help of the polarizer. In its normal configuration, as shown in Figure 45a, the MZ interferometer is used to measure the wavefront aberrations of a micro-lens under test.

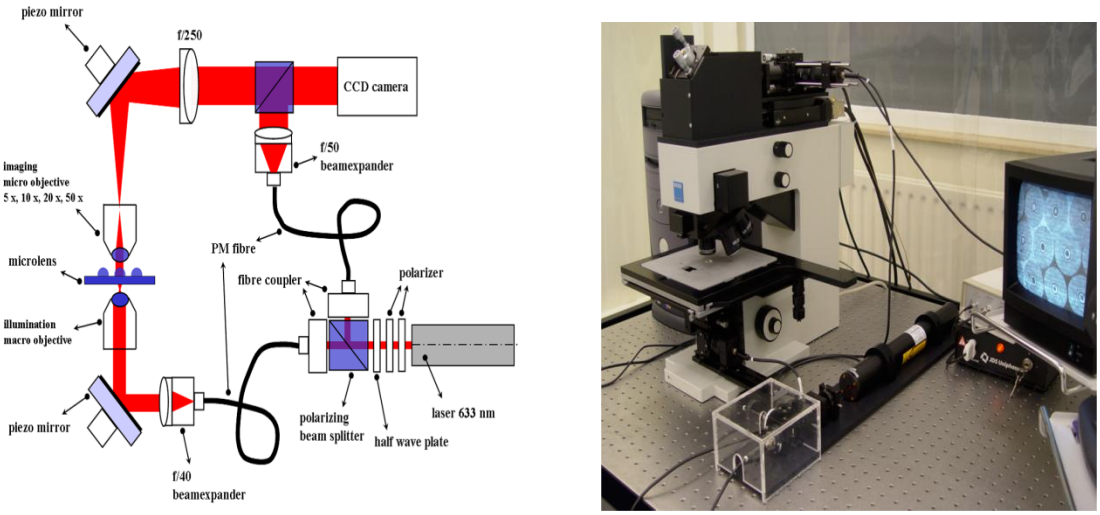

Figure 45: (a) MZ schematic and (b) picture of the MZ interferometer used for transmitted light measurements [101].

The microlens to be measured is illuminated by means of a spherical wave from the backside which is generated by means of a high quality micro-objective. The microlens transforms this wave back into a plane wave. A telescopic microscope produces an image of the lens on a CCD camera on the one hand and on the other an expanded plane wave which enters a second polarizing beam splitter is superimposed by a plane reference wave

fed through the second fiber and an expansion lens to a second beam splitter. One of the mirrors in the object arm of the MZ is mounted on a PZT driver to enable phase shifting interferometry. For this purpose the CCD camera has a pixel synchronous frame grabber coupled to a modern PC [101].

In order to implement index liquid metrology into the MZ interferometer, the illumination micro-objective was removed in order to allow plane wave illumination of the micro-lens or structure under test. This is shown in Figure 46. The input beam is approximately 2 mm in diameter. An imaging micro-objective in conjunction with a tubus lens (f/2.5) forms a telescopic combination which captures the wavefront emanating from the micro-lens array and images it onto the CCD camera.

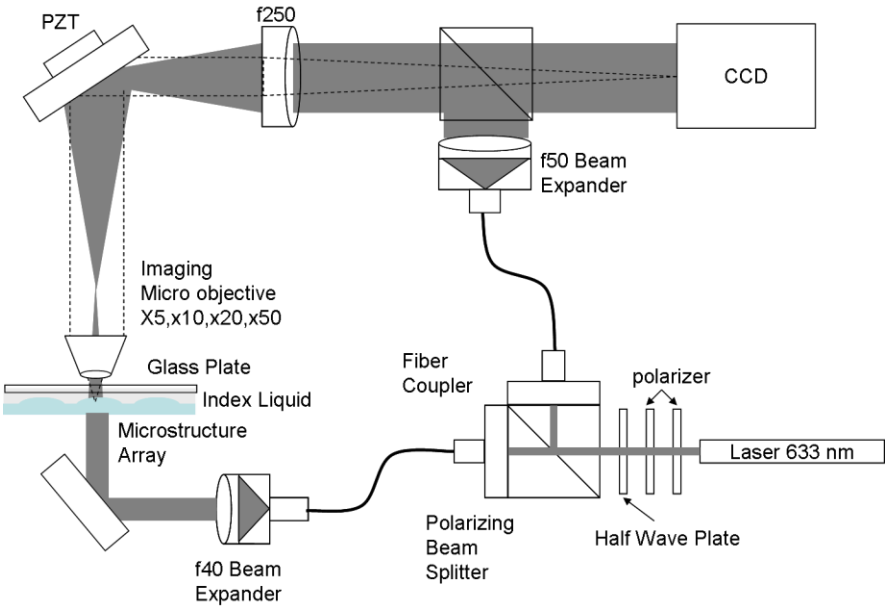

Figure 46: Index liquid metrology on MZ interferometer.

Adjustment of the MZ Interferometer

The MZ interferometer has to be adjusted in order for the object under test to be imaged sharply on the CCD camera. To implement this, the microscope has an option

that allows incoherent light from an incandescent bulb to be used to illuminate the sample under test. This procedure makes it easier to focus on the rim of the micro-lens under test by axially moving the stage which holds the micro-lens array. After the micro-lens under test is imaged sharply onto the CCD camera, the incandescent lamp is switched off and the laser beam is switched back on. A good indicator of proper focusing is by inspecting the image for an edge ringing effect (Fresnel diffraction) at the rim of the micro-lens. Once these rings vanish, the rim is in proper focus.

Now depending on the size of the micro-lens array under test or the field of view, the MZ interferometer is equipped with different imaging micro-objectives (5X, 10X, 20X, 50X). Now because these micro-objectives are used in conjunction with a tubus lens to image the micro-lens array under test, one has to make sure that they are well aligned. More specifically, the back focal length of the imaging micro-objective needs to coincide with the front focal length of the tubus lens in order to eliminate the defocus aberration. The elimination of the defocus aberration is important in plane-wave testing, since the defocus term seen in the analysis should only be associated with the micro-lens under test and not due to any lateral misalignment between the micro-objective and the tubus lens. Any additional defocusing will influence the focal length measurement of the micro-lens under test, which can also affect the sag of the micro-lens. Hence changing the micro-objective to another magnification will change the focal length. The sample should be taken out from the field of view of the interferometer. The interference pattern one sees will then consist of curved interference fringes (defocus). The tubus lens and the camera, which are mounted on a translation stage, can be moved on command by the computer until the curved fringes are straight. These straight fringes can then be nulled by tipping

or tilting the beam splitter which makes the test and reference beam parallel. Once in the null position, the micro-lens sample can then be reinserted into the interferometer and then refocused as described above.

Measurable Quantities and Measuring Procedures

The plane-wave illumination mode allows one to measure multiple micro-lenses in an array simultaneously. By choosing a suitable index liquid, one can measure fast microlenses, aspheric microlenses with hundreds of microns departure from a sphere as well as micro-structures with non-spherical geometries such as micro-pyramids. Important geometrical parameters for micro-lenses such as form error, surface profile, focal length, sag, diameter, radius of curvature, pitch, f/# and NA can all be measured either directly or indirectly by the index liquid technique. For non-spherical micro-structures such as, micro-pyramids, parameters such as surface profile, height, pitch and facet angle can also be measured using the index liquid technique.

Twyman-Green Interferometer

A Twyman-Green (TWG) interferometer is preferred to a MZ system, when testing high the transmitted wavefront of high quality optics whose aberrations are very small. This is because the wavefront has to traverse the optics twice (double-pass), and wavefront aberration is magnified by a factor of two. This will not be the case in a single-pass system as in the MZ interferometer. TWG interferometers can also be used to directly measure the form error and the radius of curvature of a micro-lens. Since most applications for micro-lenses require a spherical shape, the TWG interferometer becomes a valuable tool when investigating the deviations of the micro-lens surface from an ideal sphere.

To measure the deviation of a micro-lens from a perfect sphere, a plane wave is focused by a high quality, high numerical aperture microscope objective in such a way that the focus of the microscope objective coincides with the center of curvature of the micro-lens under test. The light rays that impinge normally on the surface, pick up any surface deviations of the micro-lens and are retro-reflected. The reflected beam carrying the deviations is then re-collimated by the microscope objective and then interferes at the beam-splitter with a plane reference beam. The micro-lens under test as well as the interference pattern are both imaged onto a CCD camera. To obtain a phase map of the form errors, phase-shifting interferometry is performed by axially shifting the reference mirror with a PZT.

As mentioned above, due to the double-pass configuration of the TWG interferometer as well as the high spatial and temporal coherence of laser illumination, speckle noise and spurious fringes can corrupt an interferogram [65, 103]. Hence, to reduce spurious reflections, polarizing optics (beamsplitter, half-wave plate) are normally implemented. These polarizing optics can also be used to balance the intensities between the test and reference arm so as to obtain high contrast fringes. Unfortunately, the interferograms still suffer from speckle noise, which lead to rough interference fringes. To reduce these effects, the spatial coherence is reduced while maintaining the temporal coherence of the laser illumination. This is implemented by introducing a rotating scatterer in the light beam which smoothes the fringes.

A picture of the Twyman-Green interferometer as well as a detailed schematic is shown in Figure 47. This interferometer works by imaging the beam from a HeNe laser onto a rotating scatterer via a microscope objective. The light is then re-collimated by an

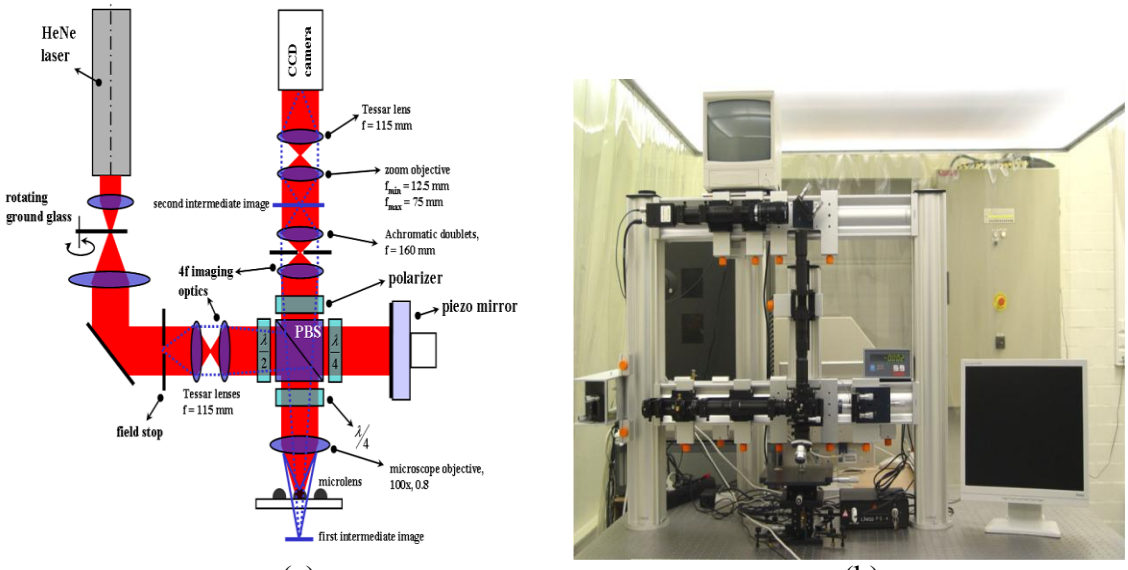

(a) (b)

Figure 47: (a) Working principle and (b) picture of Twyman-Green interferometer [103].

achromat and then passes a field stop which is sharply imaged by a 4f system onto the lens under test. The field stop can be moved along its optical axis until it is in focus on the surface of the micro-lens under test. To achieve high contrast fringes, the image of the stop due to the reference mirror should also be imaged sharply on to the CCD array. The half wave plate in front of the polarizing beam splitter allows for the intensity balance of the two arms of the interferometer, which is very essential, since the reflectivity of the lens under test and the mirror in the reference arm can be quite different. The polarizer at the exit of the interferometer is used to force the two orthogonally polarized beams to interfere. The imaging optics following the exit of the interferometer allows the intermediate image of the micro-lens formed by the condenser lens to be imaged sharply onto the CCD camera. The PZT attached to the reference mirror allows the implementation of phase-shifting.

This interferometer allows for sphericity testing of micro-lenses ranging from 50

μm to 2 mm in diameter with a maximum radius of curvature of 4500 μm. It is also possible to measure the radius of curvature of a micro-lens by using the TWG interferometer described above. In order to achieve this, the micro-lens has to be shifted axially downwards from the confocal position to the cat's eye position, which is the position where the spherical wavefront focuses on the vertex of the micro-lens under test. Visually, one should see straight, parallel, equidistant interference fringes. The difference between these two positions is monitored by a Renishaw length gauge which gives the radius of curvature of the micro-lens under test.

It is important to note that in order to visually attain the cat's eye position, the rotating scatterer should be removed from the beam path, since the cat's eye position causes an inversion of the object wavefront with respect to the reference wavefront. This causes a loss of contrast in the interference fringes with partially coherent illumination.

Optical Non-Contact Profiler

In order to measure the diameter and sag of the microlenses, a WYKO NT2000 non-contact profilometer was implemented. A schematic of this instrument is shown in Figure 48. There are two configurations in which the profilometer is used to measure a wide range of surface heights. Vertical scanning interferometry (VSI) is used to measure rough surfaces ranging from 160 nm to 2 mm. The phase-shifting interferometry mode is used to measure fairly smooth and continuous surfaces ranging from 0.1 nm to 160 nm. Since phase-shifting has been previously explained (Chapter 2), we will now discuss the principle of vertical scanning interferometry. Optical non-contact profilometry is based primarily on a Mirau interference microscope where a white light beam is split by a beam split which reflects half of the beam to a reference surface and the other half to the

sample under test. The light beam from the sample and the reference surface then recombines to form interference fringes which are imaged at the CCD camera. In the vertical scanning mode, the system measures the degree of fringe contrast.

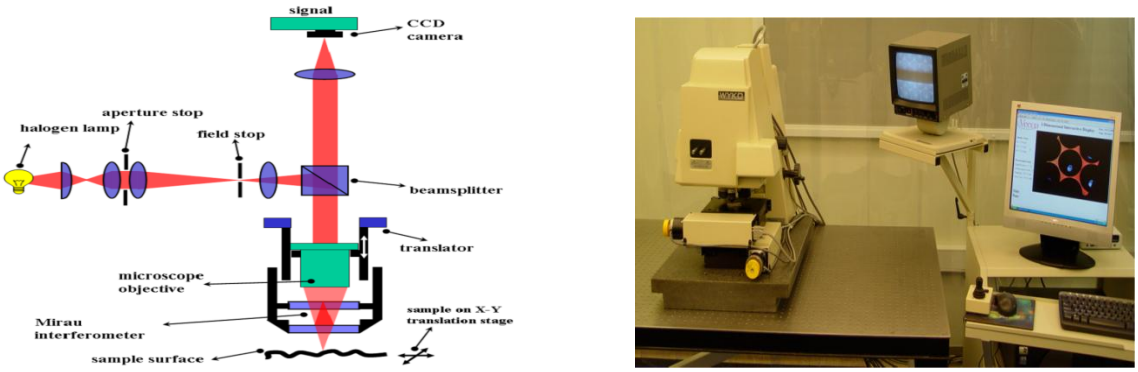

(a) (b)

Figure 48: (a) Schematic and (b) picture of the WYKO optical non-contact profilometer [104].

Since white light has a short coherence length, interference fringes will only be present over a shallow depth for each focus position. Hence, fringe contrast will reach its maximum value at a certain point on the sample as it is translated through focus. As a measurement is taken, the reference arm which contains the interferometric objective is moved vertically to scan the sample at varying heights. This is controlled by a PZT that precisely controls this motion. As the reference arm is scanned vertically, the fringe contrast of each pixel on the sample surface is recorded, after which computer algorithms are used to demodulate the envelope of the fringe signal, hence extracting the surface information of the sample under test. The vertical resolution is approximately 3 nm root-mean-square (RMS) for a single measurement. The lateral resolution of the instrument depends on several factors such as the system magnification, detector array size and cursor position accuracy [104]. The profilometer is also equipped with a stitching function which preserves a high resolution by enabling a larger field view without

switching to a lower powered objective.

Contact Stylus Profiler

A contact stylus profilometer (Dektak8, Veeco Inc.) was used to characterize the surface profiles of micro-pyramidal structures. These measurements were used to compare the accuracy of the index liquid interferometric technique. The measurements were also done to compare time.

The contact stylus profilometer works by electromechanically moving the sample under a diamond-tipped stylus. The test part sits on a high precision translation and rotation stage according to the translation speed, stylus force and scan length. As the stage moves across the sample, surface variations cause the stylus to be translated vertically. The resultant vertical motion of the stylus compresses a piezoelectric element which generates a fairly linear voltage response. Computer algorithms are then used to convert these signals into height variation information. The working principle and image of the profilometer is shown respectively in Figure 49.

Twyman-Green/ MZ interferometer at UNC Charlotte

As a comparison to results obtained using the MZ interferometer at Vrije University, measurements were also taken on a hybrid Twyman-Green and Mach-Zehnder interferometer known as MORTI (Micro-optic Reflection and Transmission Interferometer) which was developed at UNC Charlotte. This micro-interferometer can be used to measure micro-lens form and transmitted wavefront errors, as well as radius of curvature and back focal length.

MORTI is constructed on a Mitutoyo® microscope body and operates with a 0.6328 μm helium-neon laser fiber input as the light source. Figure 50 show that two

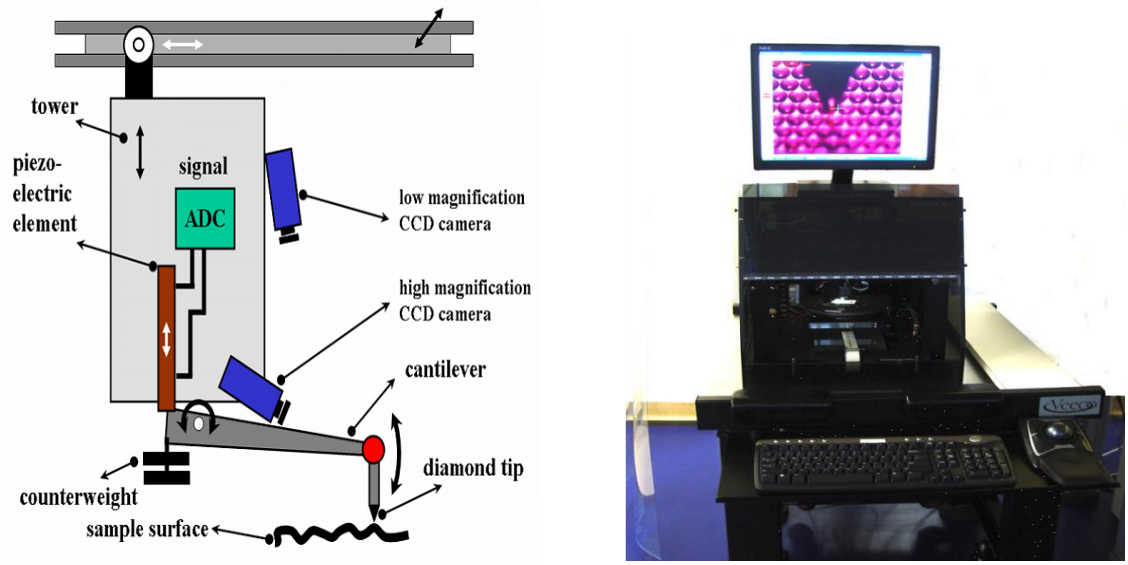

(a) (b)

Figure 49: (a) Schematic and (b) picture of Dektak profilometer [67].

fiber beamsplitters are used to divide the beam of a pig-tailed helium–neon laser into three inputs: the TG illumination, the MZ illumination and the MZ reference beam. All the fibers are single mode. In the TG configuration (solid line in Figure 50(*a*)), the beam from the illumination is collimated and expanded to a 1 cm diameter size. Then, it is split by the main beamsplitter. One beam goes to the reference mirror mounted on a PZT, while the other beam is directed through a microscope objective to the sample and reflected back. Both beams are combined again by the main beamsplitter and follow the imaging leg to the CCD camera [105].

In the MZ configuration (dashed line in Figure 50(*a*)), the MZ reference beam is 1.6 mm in diameter. It is directed to the mirror attached to the PZT by means of a beamsplitter. Then, it follows the same path as the TG reference beam to the main beamsplitter. The MZ illumination arm is also collimated and expanded to a 2 mm

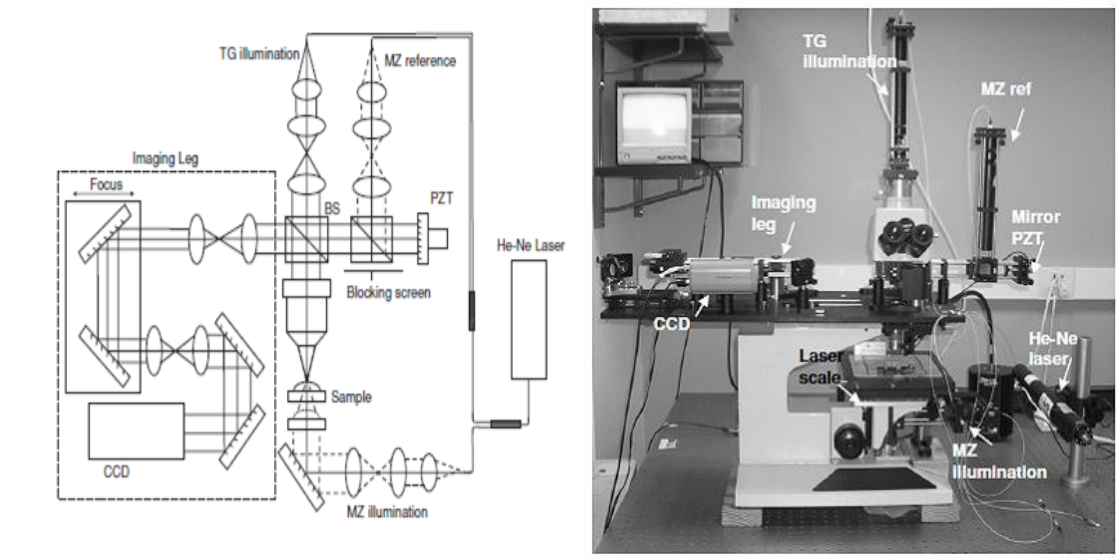

(a) (b)

Figure 50: (*a*) The MORTI schematic is shown. It is a combination of the Twyman–Green (solid line) and Mach–Zehnder (dashed line) interferometer. (b) A picture of MORTI [105].

diameter size. It travels through the sample under test and goes to the main beamsplitter, where it is combined with the MZ reference beam. The Mitutoyo microscope objective expands the beam to a 1 cm diameter if its numerical aperture is fully filled [105].

A key advantage of this configuration is the ability to image the exit pupil of the system, in this case the aperture of the micro-lens under test onto the detector array. This is achieved by varying the distance between the two afocal systems that make up the 4f imaging leg, via a focusing-fold-mirror-assembly (FFMA). By properly focusing on the aperture of the lens, one can drastically reduce the effects of Fresnel diffraction, which manifests itself as ring-like structures that occur at the edge of the aperture. These structures can affect the ability of the integrity of the phase-shifting algorithms which lead to erroneous results. This flexibility is also necessary to refocus the instrument to measure a range of different microlenses (from 0.18 to 0.6 mm ROC) [106].

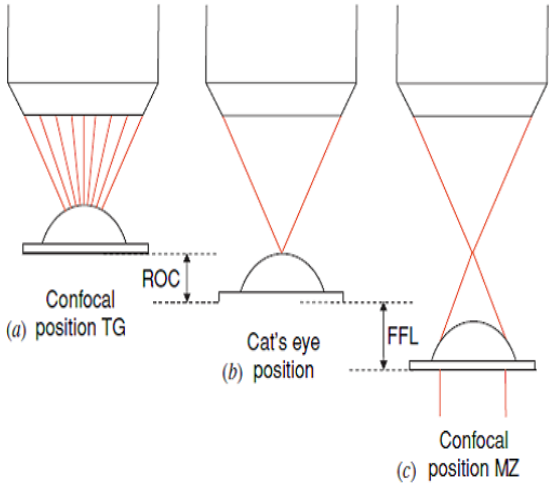

Figure 51: (a) The *z* distance from the confocal position to the (b) cat's eye position is the radius of curvature. When moving the sample from the cat's eye to the (c) MZ confocal position the front focal length is measured.

In order to perform FFL and ROC measurements (Figure 51), a Sony laser scale is centered below the stage and aligned to the motion axis to measure the *z* direction translation of the sample [106]. Surface data is acquired (phase-shifting interferometry) and analyzed using Intelliwave™ data acquisition software made by Engineering Synthesis Design, Inc.

Unfortunately, in its present state the MZ arm of MORTI did not have sufficient magnification to implement the index liquid technique. Using MORTI in its current configuration would only have allowed 13% use of the available pixels on the CCD sensor. This would not have provided sufficient lateral resolution needed for high quality measurements. Therefore a 2-lens afocal component was designed as a beam expander to replace the objective that was currently being used in MORTI. An afocal system is defined as a system without a focal length. It consists of two lenses that are separated by a distance that is equal to the sum of their focal lengths. In other words, the back focal length of the first lens coincides with the front focal length of the second lens. The

magnification is simply the ratio of the focal length of the second lens divided by the focal length of the first (f_2/f_1). This design is primarily used in binoculars and in astronomical telescopes and is known in this field as the infinite conjugate configuration.

This design fulfills two crucial functions. The first of which was to expand the beam that is incident on the test sample to approximately 8 mm which would give us a CCD fill factor of close to 100%. Secondly, the two-lens afocal system must be designed so that in conjunction with the 4f imaging leg would allow sufficient focusing on the aperture of the micro-structure under test.

Zemax, a ray trace package was implemented to aid in the design of the afocal component. Zemax was used to first approximate what type (positive or negative) lenses would be needed in order to achieve the required magnification and secondly to predict the type and magnitude of aberrations that were expected from such a design. In the starting design, the afocal component was designed to be a 5x beam expander, work at a wavelength of 0.6328 μm and to have a minimum PV wavefront error. In the preliminary set-up of the system, there was no power in the lenses and as expected no beam expansion. This is shown in Figure 52. It is important that Zemax be made to work in afocal image space or else the design could produce erroneous results. The default merit function was set so as to minimize wavefront error, spot radius and angular errors. The optimization operand “REAY” which is the real ray y-coordinate at the image surface was used to ensure that the output beam diameter was 8 mm. This diameter was chosen to ensure a magnification of 5X since the incoming beam had a diameter of 1.6 mm. The system was optimized such that the radii of curvature of the lenses were treated as variables so as to minimize the wavefront error whilst achieving a magnification of 5X.

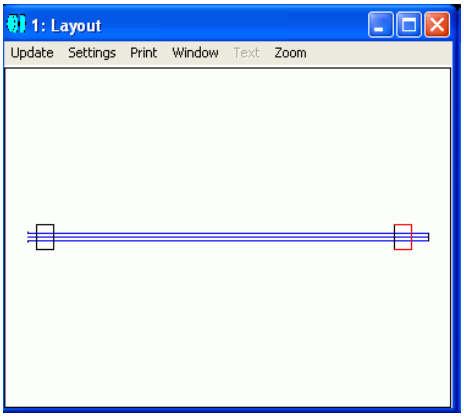

(a)

Lens Data Editor

Edit Solves View Help

Surf:Type		Comment	Radius		Thickness	Glass
OBJ	Standard		Infinity		Infinity	
STO	Standard	input beam	Infinity		5.000000	
2	Standard	expander	Infinity	V	10.000000	N-BK7
3	Standard		Infinity	V	90.000000	
4	Standard	collimator	Infinity	V	10.000000	N-BK7
5	Standard		Infinity	V	10.000000	
IMA	Standard	output beam	Infinity		-	

(b)

Figure 52: (a) Initial layout of beam expander design. (b) Lens data editor table showing the variables for optimization in the initial beam expander design.

The glass was chosen as BK7 since this is the most widespread lens material and could be found in multiple optics catalogs. The total track length was fixed at 100 mm due to space constraints in the actual system. Figure 53 shows the resulting system after optimization. Notice that Zemax outputs a negative lens (meniscus) as the first lens while the second lens is plano-convex. This is to compensate for spherical aberration which along with defocus represents two of the largest aberrations present in afocal systems. To compensate for higher order aberrations, the operand "OPDX" which is the optical path difference with respect to the mean OPD over the pupil was introduced since for a perfectly collimated output beam the OPD over the pupil should be essentially zero. Notice also than the accompanying wavefront error map has a PV wavefront error of less

(a)

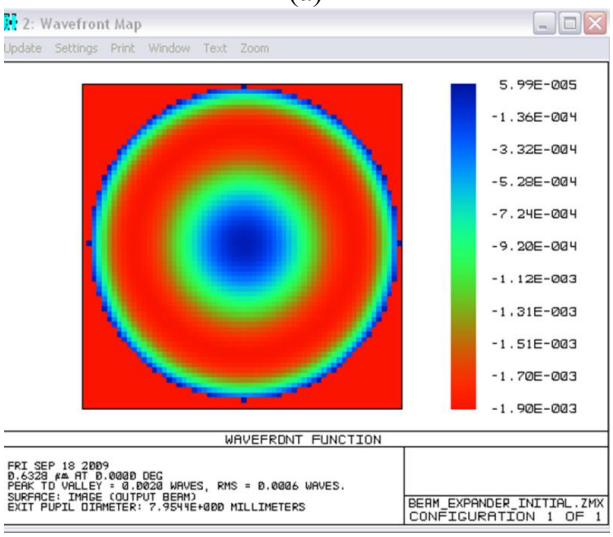

(b)

Figure 53: (a) Optimized layout for 5X beam expander. (b) Wavefront map showing PV error less than $2e^{-3}$ waves.

than $2x10^{-3}$ waves which is excellent. The wavefront map contains mostly defocus and spherical aberration.

An excel spreadsheet containing thin-lens equations of the afocal component and the 4f imaging leg were also used as a tool in order to make sure that the aperture of the micro-structure could be properly focused onto the sensor. This is shown in Figure 54. The following sign conventions were maintained throughout the spreadsheet when trying to calculate the image distance: light is travelling from left to right, distances to the left of the lenses are negative, the focal length of a convergent lens is positive, the distance to a real object is negative and finally the distance to a real image is positive. Hence a

negative value for the distance between lens f_4 and the CCD sensor indicates a virtual image which essentially means that the aperture of the micro-structure cannot be imaged onto the CCD sensor. A positive value indicates the ability of the imaging system to focus on the aperture of the micro-structure under test.

There were a number of practical constraints that were encountered when trying to design such a system. The first was making sure that the distance between the lenses in the beam expander were not too long, therefore prohibiting the afocal component from fitting in the space between the stage and the upper plate which contains the reference and imaging arm of MORTI. Although the stage could be moved vertically, its range was limited. The total track length of the beam expander system was constrained to 100 mm in total track length.

The second constraint was the trade-off between the ability of the system to image the aperture of the micro-structure onto the CCD sensor and reducing the aberrations introduced by the afocal design. For example, in the first iteration of the design (Figure 54) the first lens in the afocal system had a focal length of -18 mm whilst the second lens had a focal length of 90 mm. The axial length was 77 mm and the PV wavefront error was $2x10^{-3}$ waves. Third order spherical aberration was approximately non-existent. In terms of expanding the beam by 5X whilst having very low wavefront error this design was perfect. These focal lengths were then input into the excel spreadsheet to investigate if the afocal system in conjunction with the 4f imaging system could image the aperture of the micro structure onto the CCD sensor. The working distance of the afocal system was set at 25.4 mm. This resulted in the formation of a virtual image. In order for the

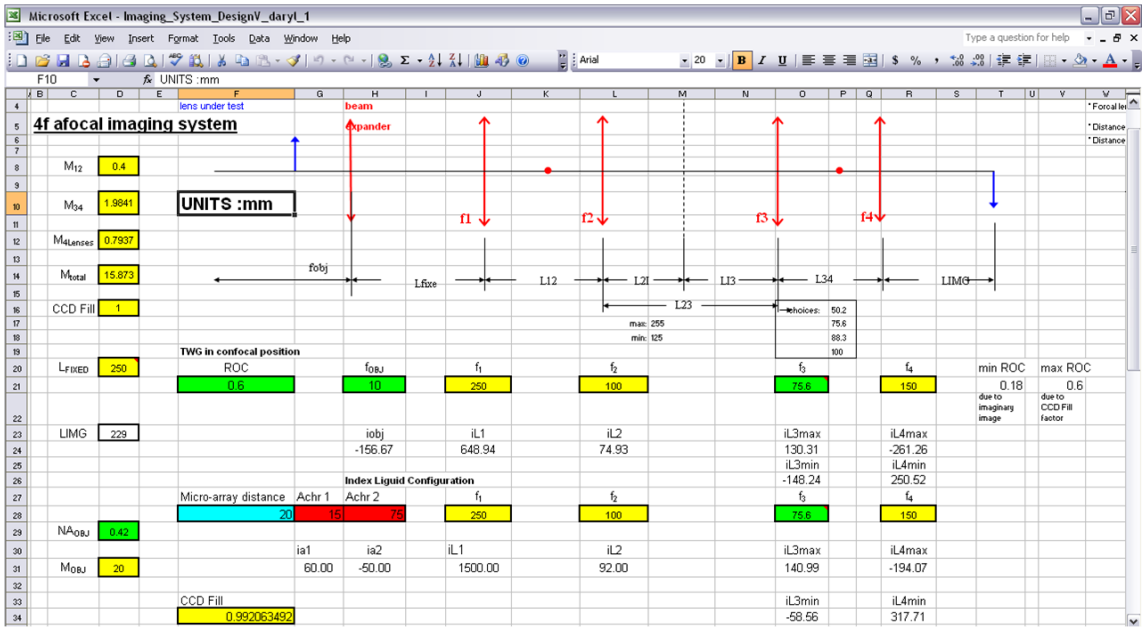

Figure 54: Excel spreadsheet containing thin-lens equation to aid in beam-expander design.

aperture to be properly focused onto the CCD sensor, the working distance of the afocal system would have to be set to 7 mm which was very impractical (too close to the beam expander) for the experimental configuration. For a more practical working distance of 15 mm, in order to achieve proper focusing, the first negative lens would have to have a focal length of – 5 mm and the second lens a focal length of 25 mm. A negative lens of this magnitude though is not easily available through lens catalogs such as Thorlabs or Newport. This type of lens would have to be specially fabricated to fit our purposes, and hence will also be very expensive.

To achieve proper focusing in the afocal design, whilst having a reasonable working distance, a positive lens would have to be used as the first lens in the afocal system. This was clearly a trade-off as a positive lens though would not be able to compensate for any spherical aberration as would a negative element. To alleviate this

potential problem, an aspheric lens of focal length 15 mm was chosen as the first element in the afocal system. This lens which was obtained from Thorlabs was specifically designed to focus an incoming collimated beam. Hence, its shape is such that it reduces spherical aberration. The second lens used in the afocal component was an achromatic doublet with a focal length of 75 mm. Achromatic lenses have the primary advantage of reducing chromatic aberration as well as spherical aberration. After inputting this design into Zemax and optimizing for the merit function, the PV wavefront error obtained was 0.0174 waves, with 0.01 waves of third order spherical aberration. The optimal distance needed between the two components to achieve this was 81.60 mm. The total axial length was 104 mm. Figure 55 shows the final system along with the wavefront error map and the 2^{nd} order Zernike coefficients. The next step was to implement and align the beam expander system into MORTI. The system could have also been aligned by using a high accuracy Fizeau interferometer. The biggest disadvantage with using the Fizeau interferometer (4 inch aperture) was that the system did not have sufficient magnification to use all the available pixels in the camera hence resolution became a factor when testing the beam expander system (1 inch clear aperture). Also, by aligning the system in MORTI, one can also compensate for any residual axial misalignments that may be present in the 4f imaging system. However, the advantage of the Fizeau interferometer lies in the fact that if the transmission and reference flat are of sufficient high quality ($\lambda/20$), the wavefront aberration measured can be attributed solely to the afocal system. The transmission wavefront error of the afocal system as measured by a WYKO RTI 4100 Fizeau interferometer will be presented later on.

The beam expander system was built using a series of adjustable length lens

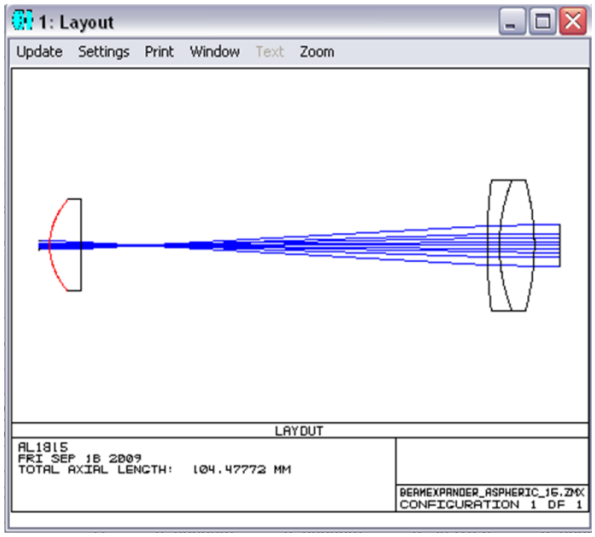

(a)

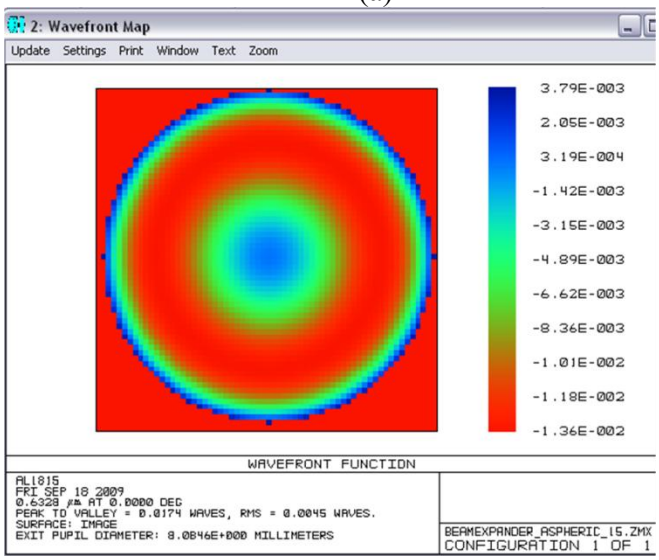

(b)

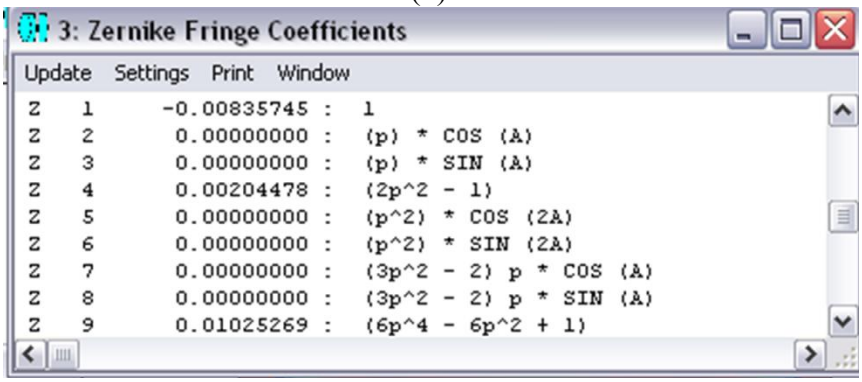

(c)

Figure 55: (a) Lay out of final beam expander system. (b) Wavefront error map. (c) Zernike fringe coefficients.

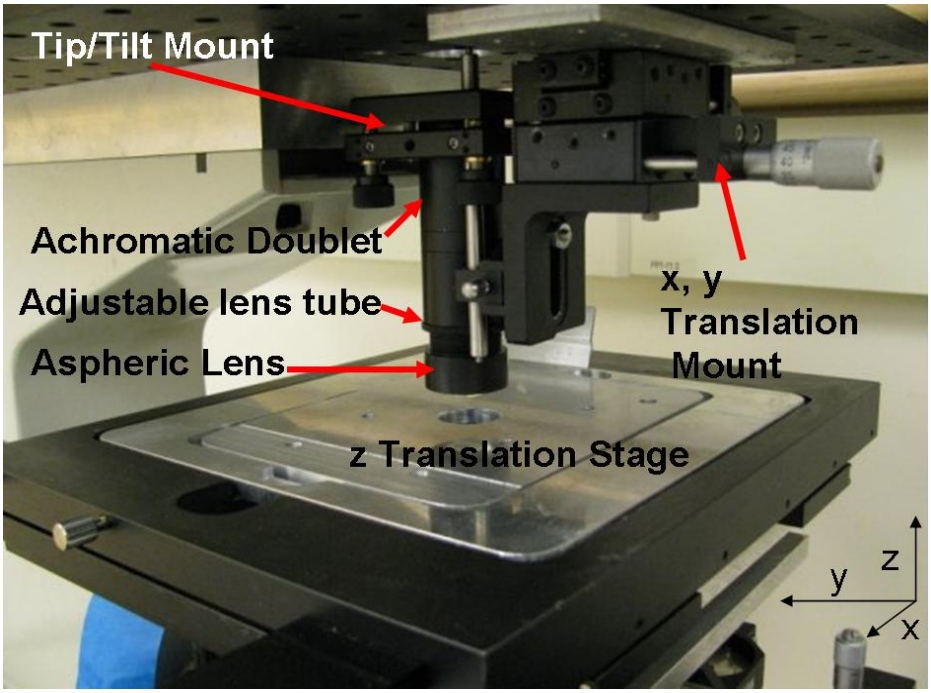

Figure 56: Fully assembled beam expander system.

tubes, cage assemblies and tip/tilt mounts. All these components were acquired from ThorLabs. Figure 56 shows the assembled beam expander system. After implementing the system into MORTI, the afocal components needed to be aligned to the optical axis of the input beam. According to the Zemax design, the optimal distance between lenses was 81.60 mm apart. To align the optical axis of the afocal system to that of the incoming beam, the afocal system was attached to a fixture that could be translated in both the x/y direction. For coarse alignment, the fixture was translated in both x and y directions until circular symmetric fringes were obtained on the monitor. For finer alignment, Intelliwave was used to measure the transmitted wavefront. The Zernike coefficients related to coma and astigmatism were then monitored after systematically translating the afocal component in the x and y directions. Large values of coma and astigmatism indicate lateral misalignment as well as vignetting of the incoming beam. Once these values were

minimized, the afocal component was fixed in the x/y position. To adjust the distances between the lenses, the first lens was placed in an adjustable lens tube. The tube was then adjusted so as to move the first lens either closer or further away from the second lens. For coarse adjustment, the tube was adjusted until the circular fringes which indicated curvature in the wavefront become less dense. Straight fringes indicate that most of the curvature of the emerging wavefront was removed. For fine tuning the distance between the lenses in the afocal pair, Intelliwave was again used to capture the transmitted wavefront. The defocus coefficient was then monitored for a minimum value. A minimum value indicated a plane emerging wavefront from the afocal system, assuming that the afocal pairs in the 4f imaging system were perfectly aligned. After obtaining

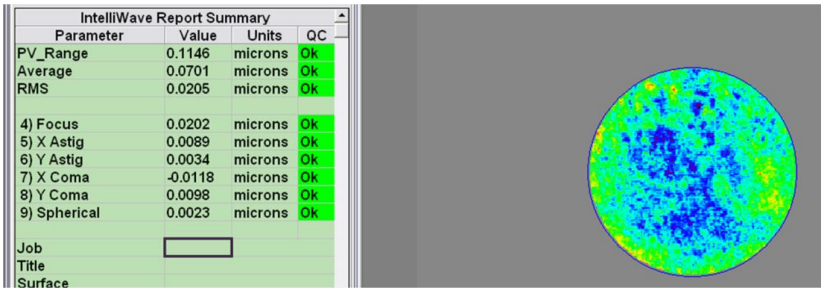

Figure 57: Transmitted wavefront error for beam expander system incorporated into MORTI.

straight fringes, the tip/tilt mirror in the reference arm was adjusted until the fringes were nulled. The PV wavefront error obtained after implementing and adjusting the afocal component in MORTI was 0.1146 microns (0.18 waves), with an rms of 0.0205 microns (0.03 waves). The OPD map for the transmitted wavefront for the MZ arm of MORTI is shown in Figure 57. It is important to note that the transmitted wavefront error is only over a clear aperture of 8 mm. This only represents ~30% of the full aperture of the beam expansion system. Also, transmitted wavefront error map contains errors not only due to

the beam expander but also from the other optics in the system, such as the 4f imaging system as well as the mirrors. To get a better understanding of the transmitted wavefront error contribution of only the beam expander over the full aperture, it was set up on a WYKO 6000 RTI Fizeau interferometer to be tested in transmission [107]. Figure 58 shows the testing configuration for the beam expander system. Alignment of the beam expander system was also performed in the x, and y direction to suppress vignetting. The lenses in the beam expander system itself were not manipulated. The reference and transmission flat were certified to λ/20. Figure 59 shows the transmitted wavefront error map for the beam expander system across its full aperture. The largest aberration excluding tip/tilt is astigmatism in the ±45 degree position. This may be due to a shearing effect which derives from a misalignment in both the x and y directions of the optical axis

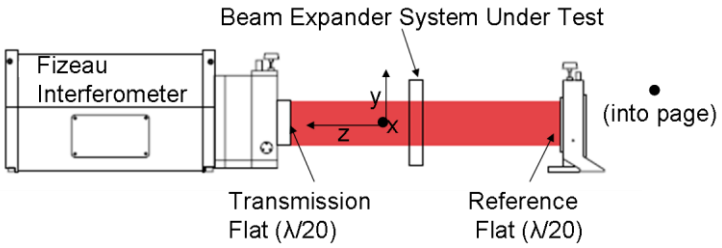

Figure 58: Fizeau interferometer used to test the transmission wavefront error in the beam expander system.

of the beam expander relative to the optical axis of the interferometer. Ignoring this aberration, we have a defocus contribution of 0.025 waves and a spherical aberration contribution of 0.138 waves. These aberrations are well above the design given by Zemax (Figure 55) and are mainly because of axial misalignment between the first and second lenses. To have λ/40 waves of defocus for an axial alignment by hand is still impressive. The aberrations caused by the beam expander will be much less since the primary function of the system is to measure microlenses whose diameters are less than 1 mm.

Also, the aberrations due to the beam expander can be saved and then subtracted from subsequent measurements of any microlens under test.

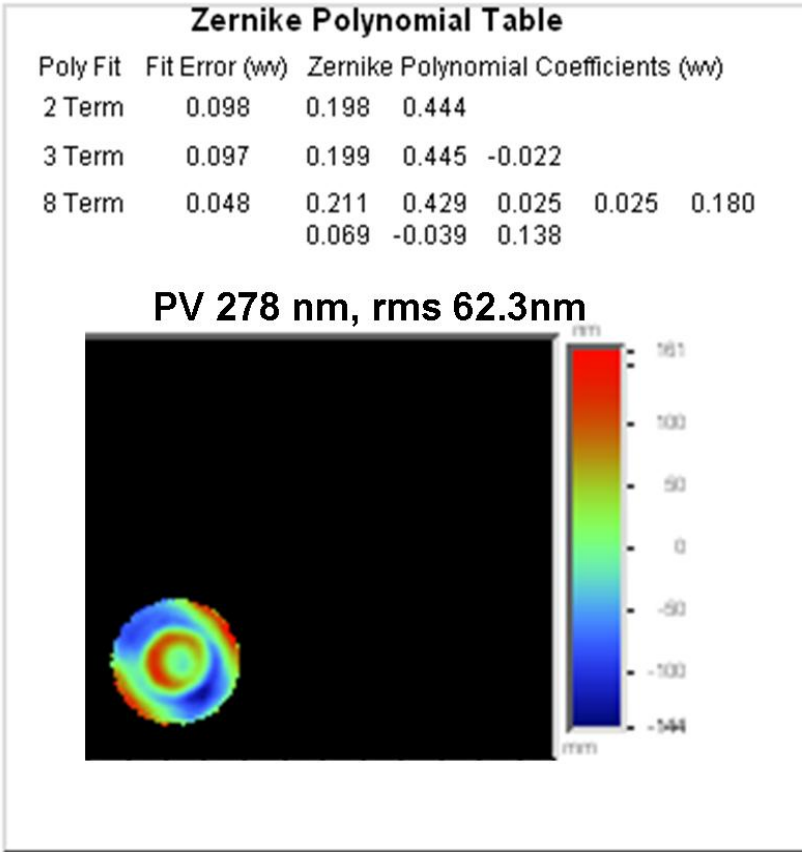

Figure 59: Transmitted wavefront error of beam expander system tested on a WYKO RTI Fizeau interferometer.

CHAPTER 4: RESULTS

As mentioned previously, the MZ interferometer, due to its inherent advantages over a TWG interferometer was the instrument of choice for implementation of the index liquid technique. The first step was to prove that the index liquid technique could be implemented to measure an individual micro-lens. Some of the parameters of interest were sag, diameter, radius of curvature and form. The index liquid technique was used to measure each parameter of interest and then compared with a more traditional measurement technique for that specific parameter.

For the proof of concept stage a micro-lens array sample was donated to us from Tessera North America (formerly Digital Optics Corporation). From this array, one lens was identified for measurement due to the ease to which it can be repeatedly located. The lens array was made of fused silica with a refractive index of 1.4564 @ 0.6328 μm, a nominal diameter of 500 μm, nominal sag of 56.1 μm, nominal conic of zero (perfect sphere) and a normal base radius of curvature of 585 μm. This lens was made to collimate light at a wavelength of 1.3 microns for datacom applications and was fabricated using an ion beam etching technique. The pitch of the micro-lens array is 1.05 mm. Figure 60 shows an image of the microlens array and also an image of the specific micro-lens that was selected for testing.

Sag Measurement

The first parameter of interest measured was the sag of the micro-lens. The sag of

a micro-lens is of particular interest, since it can be used in conjunction with the diameter to calculate the radius of curvature of a spherical micro-lens (equation 12). Certified water (n=1.333) was chosen as the index liquid due to its viscosity, wettability, non-toxicity, and ease of use. The water is placed between a cover glass slide and the micro-lens array as shown in Figure 46. The cover-glass was necessary for measurement ease of use as well as to keep the index liquid from forming a spherical shape due to surface tension.

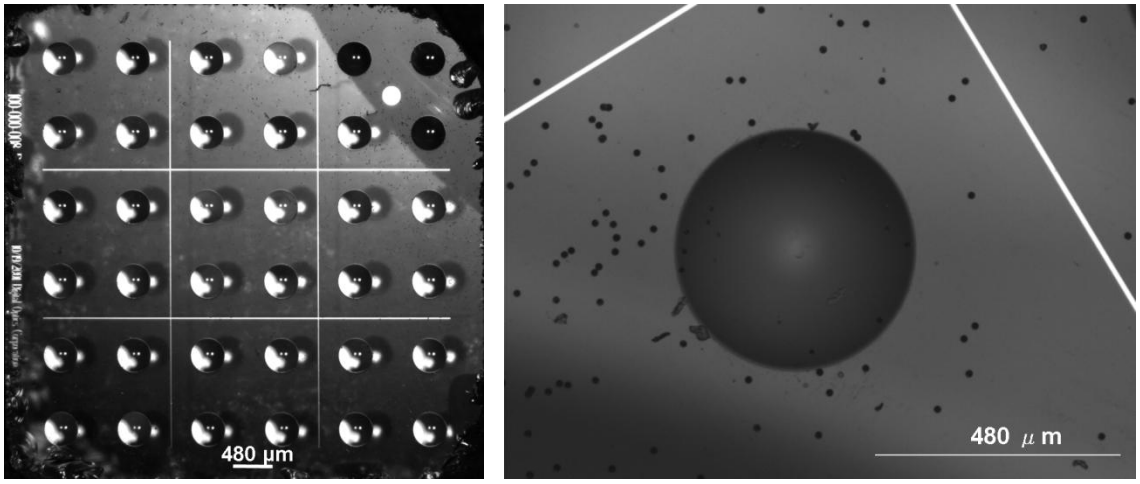

(a) (b)

Figure 60: (a) Image of Digital Optics Corporation microlens array. (b) Enlarged image of individual micro-lens.

Ten measurements were taken on the MZ interferometer and the results were compared to measurements taken with the WYKO NT 2000 profilometer. The profilometer was used in the vertical scanning interferometric (VSI) mode to measure the lens height. A 50X microscope objective was used with a FOV of 581 x 528 μm^2 with a pixel size of 0.315 microns. The WYKO NT 2000 measurement had significant data drop out in the high slope regions of the surface, which is a common limitation with optical profilometers measuring in reflection. A higher magnification microscope could be used

in conjunction with stitching to maybe increase the slope capture and maintain the field of view. There is an asymmetry in the instrument due to non-square pixels in the camera that causes more data drop out on the right-left sides of the micro-lens array than the top-bottom sides. There is no such data drop out with the index liquid technique as evidenced in Figure 62b. This measurement was obtained with the 10X imaging objective. Even

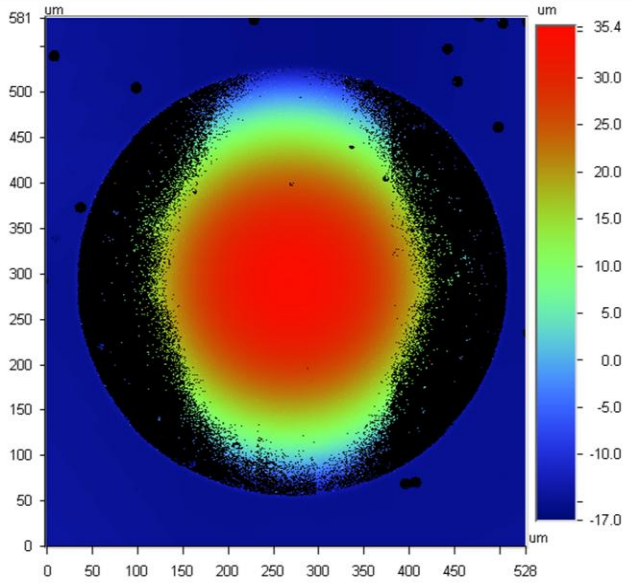

Figure 61: Contour map of the micro-lens obtained by using a WYKO NT 2000 profilometer.

with the data drop out, we can compare the sag values between the MZ and WYKO NT profiler. The optical profilometer measured a sag of 52.22 μm with a standard deviation of 0.2 μm. The index liquid technique measured a sag of 52.15 μm with a standard deviation of 0.2 μm. These measured values are consistent between the two measurements and agree to within 0.1%. The repeatability of the index liquid technique is also comparable to the WYKO NT profilometer and shows very good stability even though water was used as the index liquid and has a low viscosity. The repeatability outlined above was static repeatability in which ten successive measurements were taken

without removing the micro-lens. These measurements also indicated a 7% difference with respect to the nominal sag. Because these micro-lenses are made by ion beam

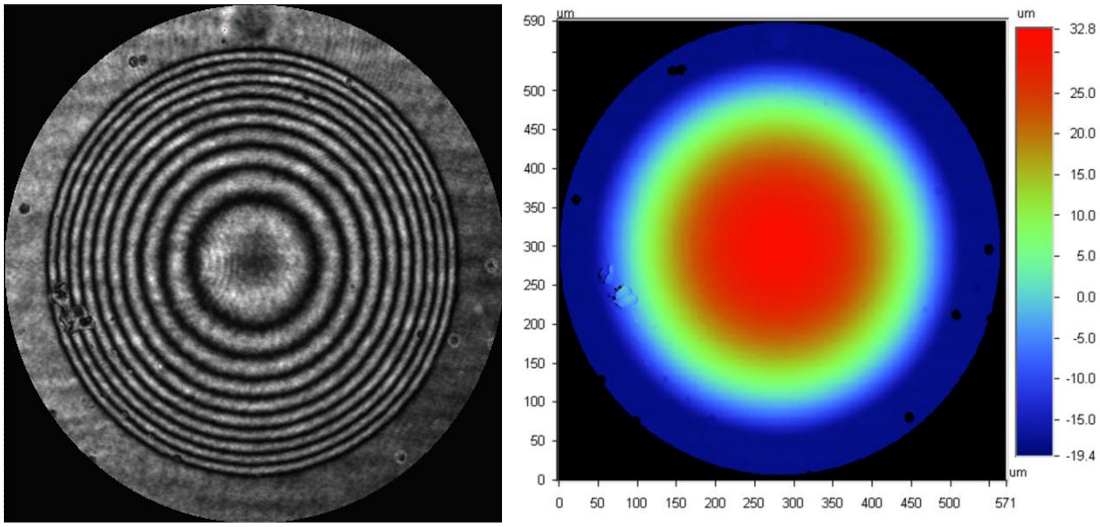

(a) (b)

Figure 62: (a) Interferogram of micro-lens. (b) Contour map of micro-lens obtained by using the MZ interferometer with water as the index liquid.

etching, the sag difference may occur due to edge taper of pedestal, solvent evaporation and contact angle effects [108]. It is also interesting to note, that even without the use of PSI, that one can still get a fairly reliable measure of the sag of the micro-lens by simply counting the number of fringes within the micro-lens aperture. In this case, there are 10 fringes which correspond to an OPD (mλ) of 6.32 microns. Using equation 47, the sag measured from counting fringes is approximately 50 μm which is in good agreement with the PSI technique.

Diameter Measurement

The next parameter of interest is the micro-lens diameter. This is another important parameter to the micro-lens manufacturer as is directly impacts the ROC and focal length calculations. There a number of techniques that can be used to measure the micro-lens diameter. One way is implementing a masking technique in Vision32 which is

an optical testing software. Another method involves using the various image processing (edge-detection) techniques in Matlab to find the aperture of the micro-lens. The masking technique is more intuitive but less accurate than using the image processing technique since estimating where the micro-lens meets the substrate is a very subjective process. However, the masking technique was chosen because one has more control over this method than image-processing. Before the diameter can be calculated, the pixel size of the camera associated with the WYKO NT profilometer and the MZ interferometer first has to be measured by performing a lateral calibration. This was implemented using a lateral calibration artifact that was supplied with the WYKO NT profiler. It consisted of a transparent glass substrate with finely-divided etched line gratings. After lateral calibration of the WYKO profiler the x pixel size was 0.315 μm whilst the y pixel size was 0.297 μm for the 10X objective. Since the lateral calibration artifact was transparent it could be also used to determine the pixel size in the x and y direction for the MZ interferometer. The x pixel size measured was 1.154 μm and the y-pixel size was 1.116 μm. Notice that the lateral resolution of the WYKO profilometer is much greater than that of the MZ interferometer. This is because a larger magnification objective was used in the case of the WYKO profilometer. The WYKO profilometer (1678 x 1582) also had a greater camera array size than the MZ interferometer (571 x 735). A larger magnification imaging objective could have been used for the MZ interferometer, but this would have narrowed the field of view to such an extent that the entire micro-lens aperture would have not been visible hence restricting the diameter measurement.

For the masking technique, a circular mask was used in the Mask Editor control

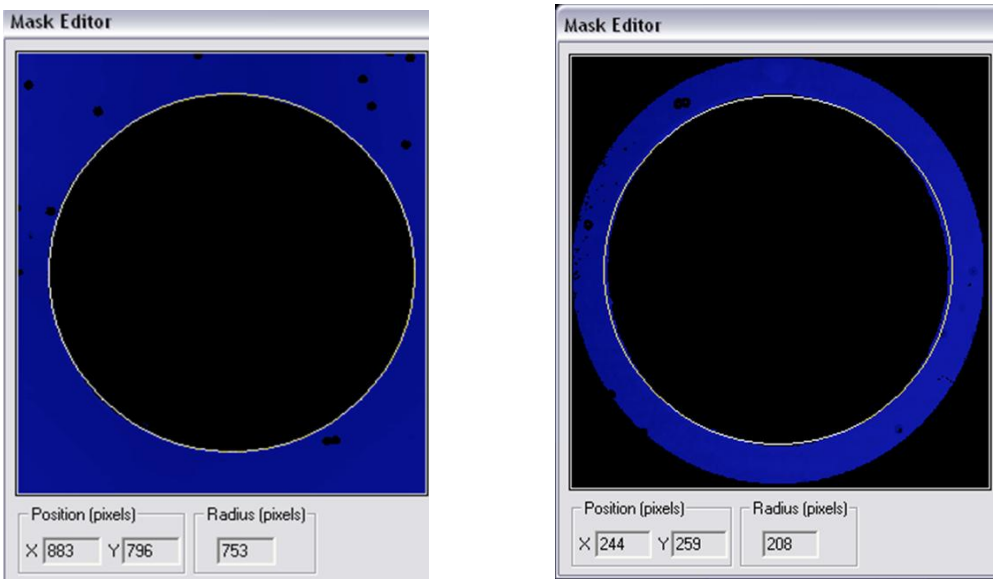

(a) (b)

Figure 63: (a) Mask circle for micro-lens measured on WYKO NT profiler. (b) Mask circle for micro-lens measured on MZ interferometer with 1.33 index liquid.

box of the Vision software. The masking circle can then be manipulated in terms of center position and size until it fits the aperture exactly. The measurement data was also subjected to filtering to exclude the lens data and hence leave the substrate, enabling the diameter to be found more accurately. Figure 63 illustrates the masking circle for both the WYKO NT and MZ measurements. The radius in pixels for the WYKO profilometer measures 753 pixels while the MZ interferometer measures 208 pixels which corresponds to a diameter of 474.4 µm and 480.1 µm respectively. These measurements once again have very good agreement (~1%). On comparing these measurements to the nominal diameter (500 µm) there is a 4% difference. Fresnel diffraction effects generated by the photo-lithographic mask being held away from the substrate due to the relatively thick resist can account for this diameter difference [108].

Radius of Curvature

The radius of curvature (ROC) can be derived indirectly from known parameters

or directly by using a TWG interferometer. Equation 12 can be re-arranged to solve for ROC once the sag and diameter of the micro-lens under test is known.

$$R = \frac{h}{2} + \frac{d^2}{8h} \tag{59}$$

As an example, by using the diameter and sag calculated by the index liquid technique, the calculated ROC is 580 μm. It is smaller than the nominal ROC because both the sag and diameter are also smaller than their nominal values.

The most accepted method to measure the ROC of a micro-lens is measure the difference between the cat's eye and confocal positions in a TWG interferometer (Chapter 3). Of course ROC measured in this way depends on the accuracy and precision of the mechanical Renishaw stage. The TWG interferometer built at Erlangen University was used to measure the ROC of the micro-lens repeatedly for ten measurements. Figure 64(a) and (b) illustrates the fringe patterns in the confocal and cat's eye positions respectively. The fringes were nulled as best as possible in both positions. Due to the fact that there might be actual tilt or form errors in the micro-lens the confocal position may exhibit residual fringes. Fringes may also be visible in the confocal position due to the fact that the micro-lens might be aspheric in surface profile. Tilt fringes may be present in the cat's eye position due to either tilt in the interferometer optics, form errors or because the cat's eye reflection was not directly at the apex of the micro-lens. The average ROC obtained for the TWG interferometer was 592.18 ± 2 μm. The index liquid technique could also be used to calculate the ROC by fitting a 3-D best fit sphere (Gauss-Newton method) to the same surface profile obtained with water as the index liquid. The ROC measured by the index liquid technique was 567.2 ± 0.1 μm. These values agree to within

~ 4%.

The ROC measured by the TWG was ~1% greater than the nominal value, whilst the ROC measured by the MZ interferometer was ~3% smaller than the nominal value

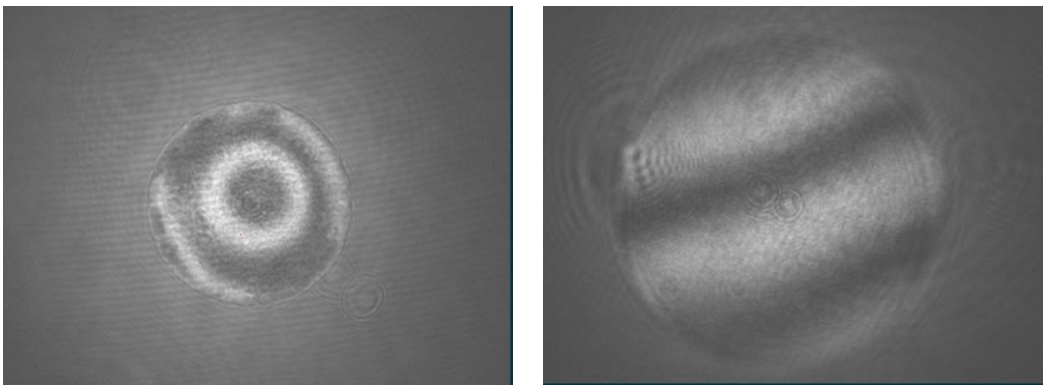

(a) (b)

Figure 64: (a) Confocal position for micro-lens. (b) Cat's eye position of micro-lens.

(585μm) of the micro-lens. Also the ROC measured by the index liquid technique is significantly lower than that measured with the TWG interferometer. This discrepancy may be due to numerous factors. One factor to consider is that in the index liquid technique, it is assumed the micro-lens under test is a perfect sphere. Hence in fitting the surface profile to a best-fit sphere, the following equation was implemented:

$$z = \sqrt{R^2 - x^2 - y^2}\ . \tag{60}$$

Because these micro-lenses were etch into fused silica, it is imperative that the etch rate and etch gas composition is very well-controlled. If not, it is entirely possible that an asphere is generated instead of a sphere [108]. Hence if a best-fit sphere is fit to an asphere the ROC measured may be inaccurate. To prove this, an aspheric micro-lens with a ROC of 206 microns and a clear aperture of 230 microns was simulated in Matlab using equation 35 with different conic values. Equation 60 was then implemented using the Gauss-Newton least squares fitting algorithm [109]. Figure 65 shows that if a best-fit

sphere is fit to any surface profile that does not have a conic of zero (perfect sphere), the calculated ROC will be inaccurate by as much as 38 μm. The higher the conic of the aspheric microlens, the larger the calculated ROC value. It is also seen in Figure 65, that none of the curves match the k = 0 at the micro-lens vertex which is precisely where the base ROC is defined. This comes from the fact the least-square algorithm is minimizing

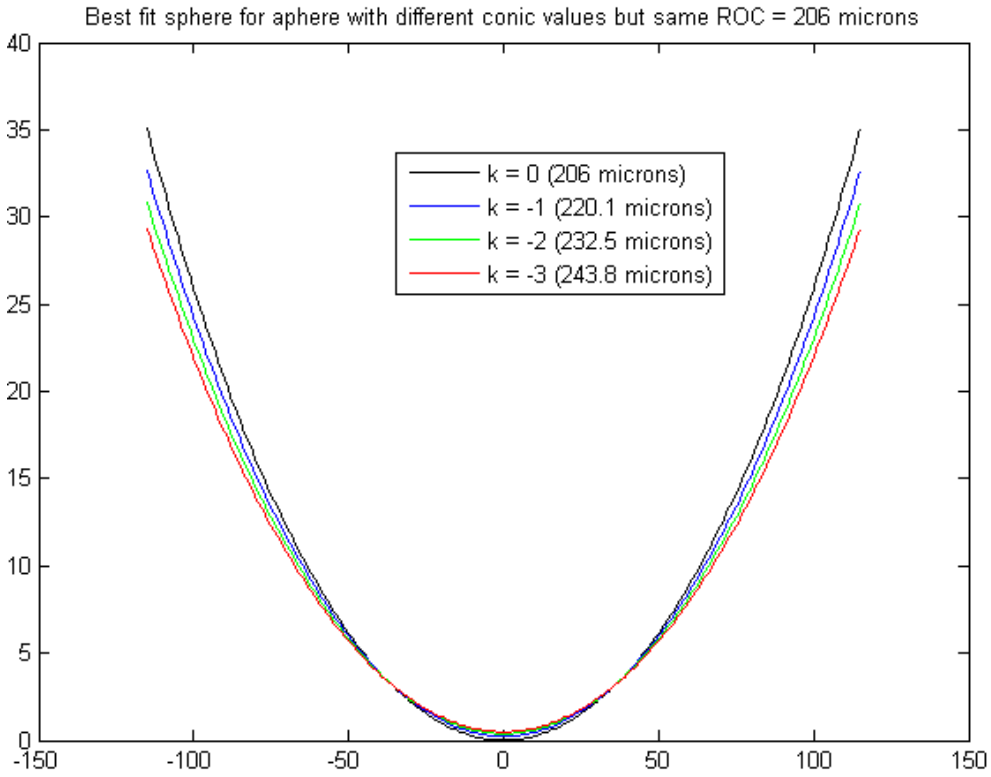

Figure 65: ROC as a function of conic values when fitting to a best-fit sphere.

(balancing) the sum of the squares between the fit and the actual data. Because the difference between the fit and measured sag is larger at the edge of the microlens the algorithm has to compensate at the vertex therefore resulting in a larger ROC. Hence the best-fit sphere algorithm over compensates for the ROC when trying to fit an aspheric surface. If the clear aperture is reduced or cropped, the best-fit ROC will approach the base ROC. This concept is shown in Figure 66. Here it can be seen that a 78 % reduction

in the clear aperture will result in a ROC of 206 μm. Notice that in Figure 65, the conic values were negative and represented a hyperbolidal surface. It can also be similarly

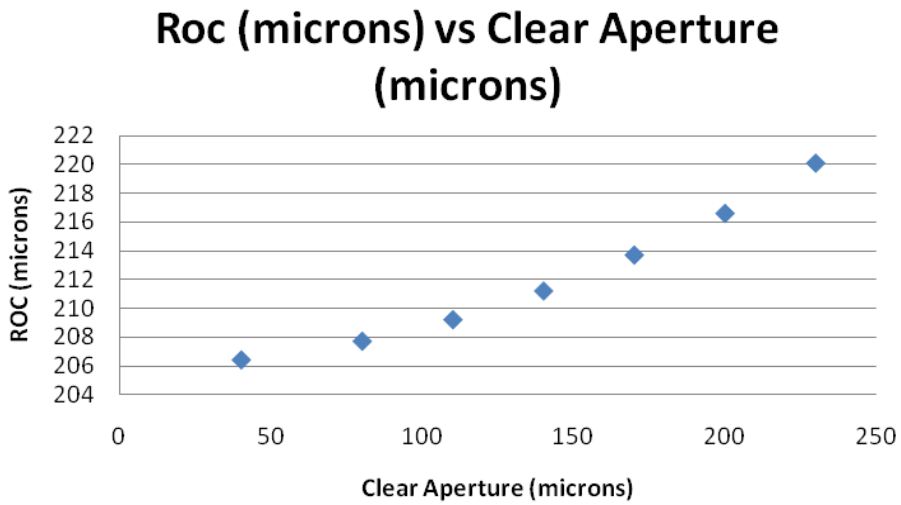

Figure 66: Best fit sphere ROC vs. clear aperture of aspheric micro-lens for a conic of -1.

shown that for conic values larger than zero (oblate spheroid), that the best-fit sphere algorithm will under compensate hence producing ROC values which are smaller than the true value. Figure 67 illustrates this concept.

Of course, if one is given a micro-lens both the ROC and conic constant will be unknown. Therefore, a more rigid technique will have to be employed to calculate the base ROC. This can be done by fitting (non-linear methods) the surface profile obtained with the index liquid technique by employing equation 35 instead of equation 60. Of course this type of fitting is more complex, since equation 35 has two unknowns which are inter-dependent whilst equation 60 has only one unknown. Figure 68 examines the 2-D case for a fit to the surface profile obtained with the index liquid technique using equation 35 (aspheric equation) and equation 60 (best-fit sphere). The fits are so good that the individual curves are indiscernible. Table 5 lists the calculated parameters of

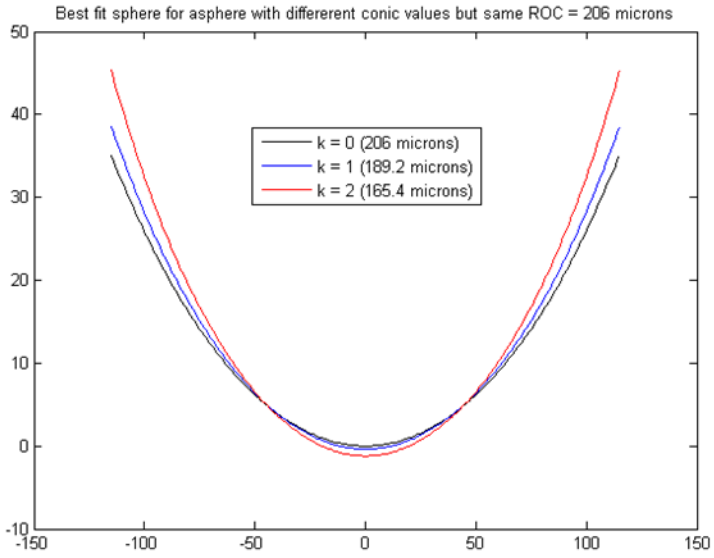

Figure 67: ROC as a function of positive conics when fitting to a best-fit sphere.

interest as well as the goodness of fit statistics. The values in brackets represent the 95% confidence level bounds for the ROC and conic values. The goodness of fit statistics (SSE, R-square, etc) illustrates how well the fits represent the raw data. The sum of squares error (SSE) measures the total deviation of the predicted values from the raw data. A value closer to zero indicates that the model has a smaller random error component and that the fit will be more useful for prediction [110]. The R-square statistic measures how successful the fit is in explaining the variation of the data. The closer the

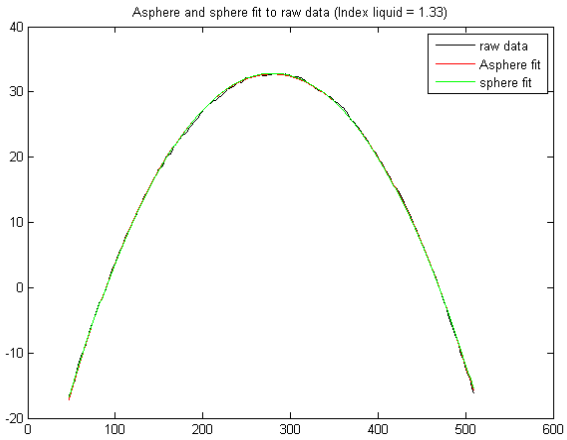

Figure 68: Asphere fit vs. best-fit sphere for index liquid technique.

Table 5: Fit statistics

Parameters	Asphere Fit	Sphere Fit
ROC(μ m)	582.4 (579.9,585)	568.2 (567.4,569)
k	0.6749 (0.5598, 0.79)	NA
SSE	16.03	21.31
R-square	0.9998	0.9998
Adjusted R-square	0.9998	0.9997
RMSE	0.2009	0.2314

value is to 1 indicates that a greater proportion of variance is accounted for by the model [110]. The adjusted R-square statistic takes into account the number of fitted coefficients and adjusts the R-square value based on the degrees of freedom [110]. Again a value closer to 1 indicates a better fit. The RMSE parameter describes the standard error in the fit and a value closer to zero indicates that the fit is more useful for prediction [110].

The first point to note is that ROC obtained using the asphere fit is different (~3%) than that obtained using the best fit sphere as might have been expected since the micro-lens under test may not be a perfect sphere. It is also important to note that the ROC calculated by the asphere fit is larger than that for the best-fit sphere. This can be compared to the simulated best fit curves shown in Figure 67. Hence, we expect the conic constant for the micro-lens under test to be greater than zero, which in this case it was calculated to be 0.67. Also notice, the ROC obtained by the 2D best fit sphere has a very strong agreement to the ROC obtained by the 3-D best fit sphere (less than 0.2%).

On closer inspection of Figure 64a there is residual defocus, coma, tilt and spherical aberration present in the fringes which may cause inaccurate ROC measurements on the TWG interferometer since the operator may find it hard to visually null the fringes. Theoretically, for a perfect sphere, the only fringes present should be due

to spherical aberration. Defocus is a misalignment error; whilst tilt can be due to misalignment or actual tilt cause by coma in the lens. Unfortunately, the TWG interferometer constructed at Erlangen University did not have a tip/tilt stage. This would have allowed the decoupling of tilt from coma.

Because nulling fringes (defocus = 0) in the confocal and cat's eye positions is virtually impossible, many techniques have been developed to compensate for this positioning error known as null cavity error. One technique determines the distance the part is offset from the null condition based on the NA and defocus calculation [112]. Another method involves taking multiple measurements through confocal and cat's eye and plotting defocus vs. position allows the ROC to be extracted [112]. It is this method that will be used to extract a more robust ROC measurement from the TWG interferometer. After the defocus (power) Zernike coefficient (z3 from Astigmatism is defined by the third term in equation 15 and increases with the off-axis object and image distances from the optical axis h' as well as with the aperture radius, r. This aberration also becomes more severe with increases in θ. Astigmatism results when rays from an off axis object point that lie in the sagittal plane come to focus at a different distance than rays that lie in the tangential plane. This is shown in Figure 26 for an off-axial point P. To eliminate astigmatism in an optical system, the tangential and sagittal surfaces must be made to coincide. This can be achieved by altering the curvatures and spacing between lenses. The resulting surface is then called a Petzval surface. Although in a Petzval surface astigmatism is eliminated, field curvature (h'^2r^2) still remains because the Petzval surface is curved. This means that the focus changes from the center out to the edge of the field of view. This aberration causes flat objects to

be imaged onto a curved surface rather than a plane. To eliminate field curvature, an

Table 2) is plotted against position a linear fit is performed on the data and the intercept (defocus = 0), denotes the null position. This is done for both the confocal and cat's eye positions whereby the difference between the two intercepts gives the radius of curvature. Figure 69 illustrates the implementation of the null cavity correction. Using the linear fit in the confocal position, the z-position for a null cavity is -60.208 mm. The z-position for null cavity in the cat's eye position is -59.63 mm. Hence the ROC for the micro-lens is 577.8 μm. The ROC values that were calculated using the index liquid technique in conjunction

with the asphere fit (582.4μm) and the null cavity correction (577.8μm) method agree to within ~1%. Also note that both ROC values are also smaller than the nominal ROC (585 μm) of the micro-lens which was expected due to the smaller diameter and sag. It is also important to note that aberrations in the TWG interferometer could affect the

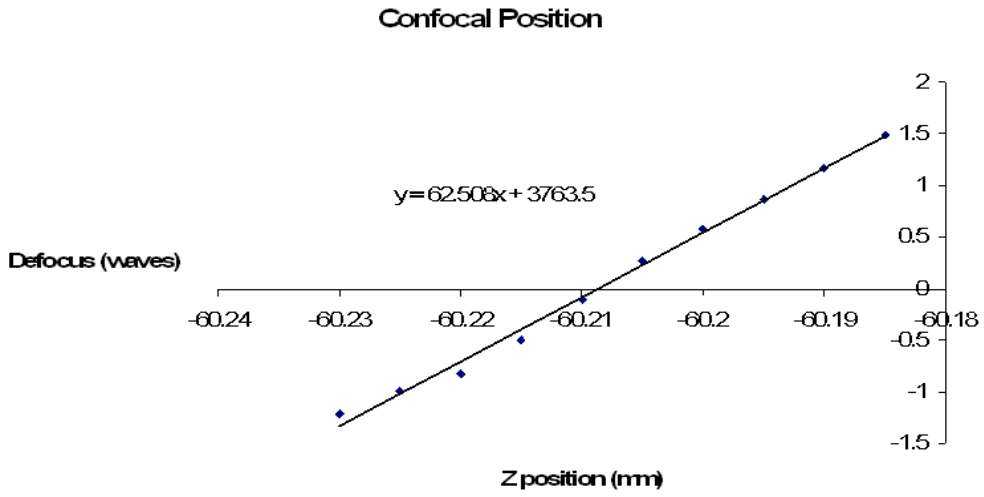

(a)

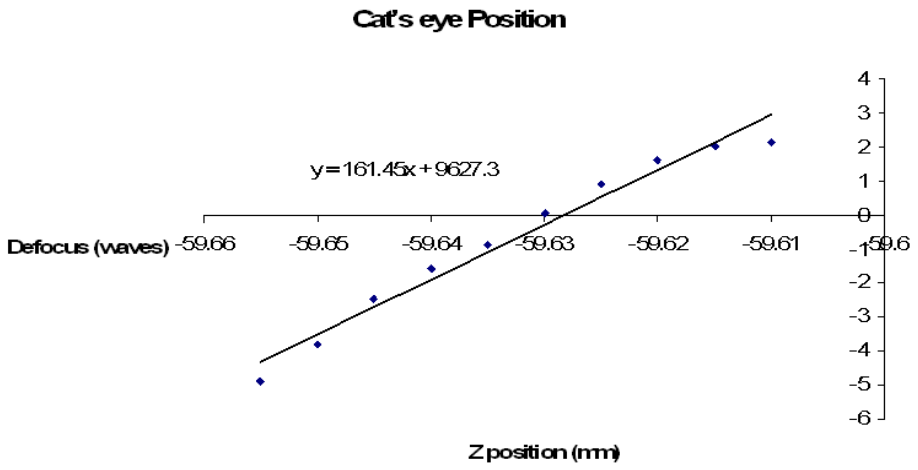

(b)

Figure 69: Null cavity correction for the confocal and cat's eye positions.

determination of the cat's eye position whilst aberrations caused by re-trace errors could affect the determination of the confocal position. Interferometer and re-trace errors can also affect the wavefront and hence the ROC calculation in the MZ interferometer [106]. Uncertainties in the ROC measurements for the TWG interferometer can also be caused by mechanical errors such as optical axis/mechanical misalignments and parasitic error motions [112]. All these uncertainties can give rise to the imperfect fits seen in Figure 69.

Form Errors

Our ultimate goal is to measure the form errors on the micro-lens. In order to focus on the form errors, we subtract a base sphere from the surface profile obtained from our index liquid technique. A 0.75 NA 100X microscope objective was used to test the micro-lens in the TWG configuration. For the index liquid technique, an index liquid with a refractive index of 1.80 was used to measure the micro-lens under test. This specific index was chosen since this provided the largest index difference with respect to the refractive index (1.4564) of the micro-lens sample and hence a greater vertical

resolution (~20nm) according to equation 58. Of course, the vertical resolution needed depends on the tolerance set by the manufacturer for a particular micro-lens. If the manufacturer only needs to know the departure from sphere to λ/10, then an index liquid much closer to the index of the micro-lens sample can be used. Since, there was no knowledge of the micro-lens tolerance, the index liquid that allowed the maximum resolution was chosen. Of course, the micro-lens sample could have been tested in air, but this would have violated the Nyquist theorem. Figure 70 shows the interferogram and surface profile obtained for the index liquid technique using an index liquid with a refractive index of 1.80. Figure 64a shows the interferogram at the confocal position for the TWG interferometer. Figure 71a and b illustrate the form error maps for the TWG and index liquid technique respectively. What standouts immediately in both form error maps is the presence of spherical and coma aberrations. One expects spherical aberration since the surface profile is weakly aspheric (0.67). Coma may be either due to an oblong surface profile, retrace-errors or interferometric errors. A noticeable feature of the index liquid form error map is the higher frequency structure that superimposes itself on top of the form error map. This is due to the interferometric bias of the MZ interferometer. This bias can be subtracted by removing the micro-lens sample under test taking a measurement of an empty cavity. Figure 72 (a) illustrates the interferometer bias of the MZ interferometer whilst Figure 72 (b) shows the form error map for the index liquid technique with the interferometer bias removed. The PV and rms values indicate very

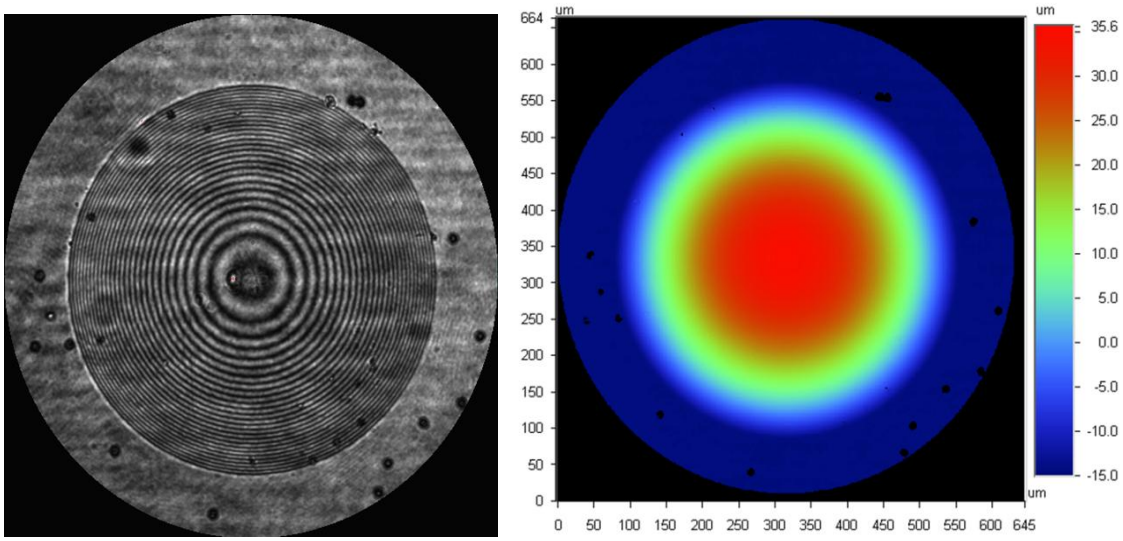

(a) (b)

Figure 70: (a) Interferogram for index liquid of 1.80. (b) Surface Profile for index liquid of 1.80.

good agreement between the TWG interferometer and the index liquid technique. The form error map for the TWG interferometer also seems to be rotated 90 degrees in a counter clockwise position with respect to the form error map given by the index liquid technique. If coma is indeed present in the micro-lens under test, rotating the sample the sample itself could have been rotated by 90 degrees between the MZ and TWG interferometer measurements. To confirm this, the micro-lens array was rotated at 90, the sample itself could have been rotated by 90 degrees between the MZ and TWG interferometer measurements. To confirm this, the micro-lens array was rotated at 90,

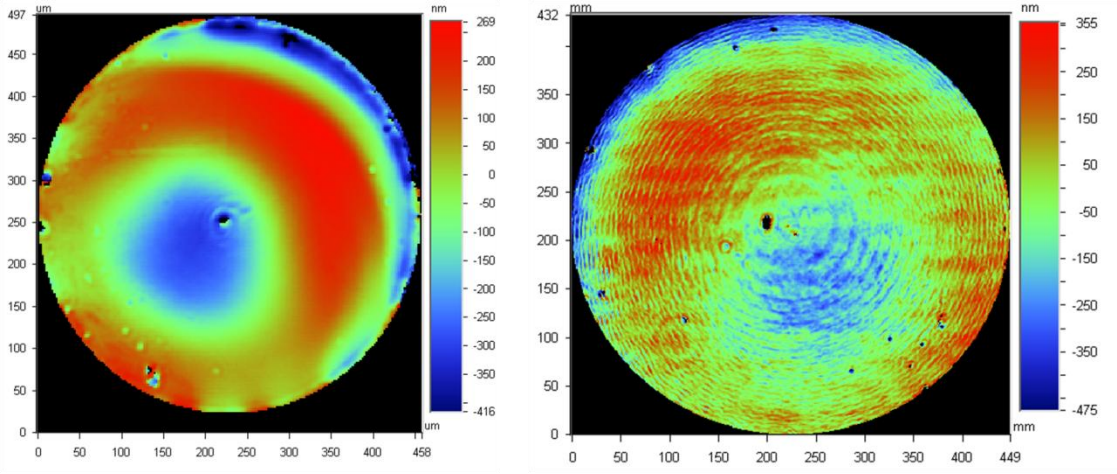

(a) (b)

Figure 71: (a) Form errors for TWG interferometer (PV = 670 nm, rms = 149.3 nm). (b) Form errors for index liquid technique (PV = 824.4 nm, rms = 133.6 nm).

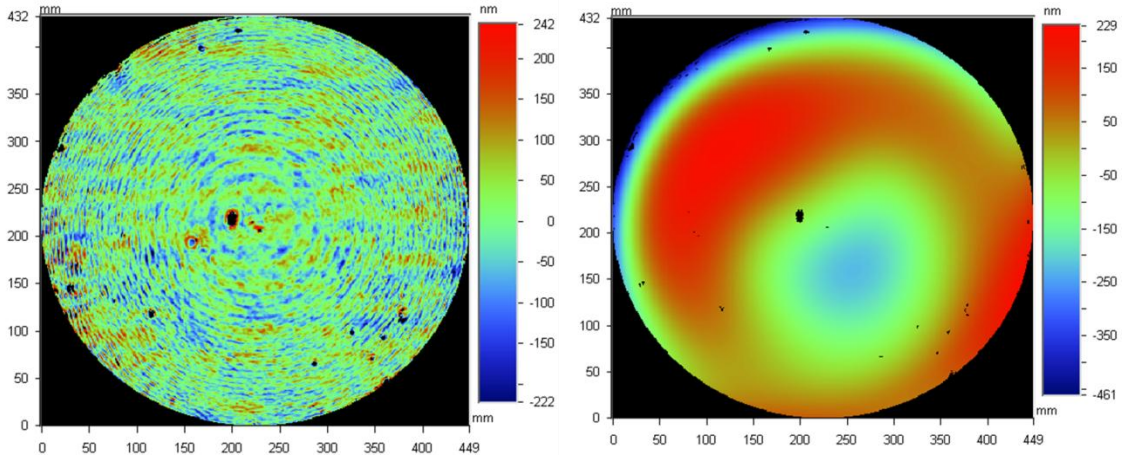

(a) (b)

Figure 72: (a) MZ interferometer bias (PV = 449.4 nm, rms = 59 nm). (b) Form error map for index liquid technique with interferometer bias removed (PV = 678.5 nm. rms = 121.9 nm).

180 and 270 degrees from the original orientation and measured using the TWG interferometer. Figure 73 illustrates the rotated form error maps which indeed confirm that the coma is within the micro-lens and is not due to the interferometer. Lastly, Table 6 compares the Zernike fit up to the 2nd order for the form error maps obtained for the TWG as well as the index liquid technique. There is very good agreement between the

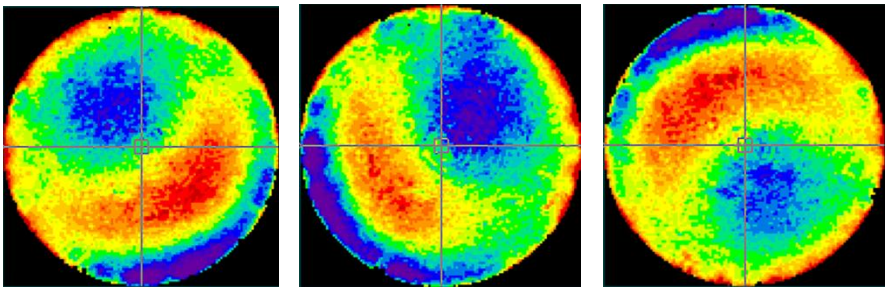

(a) (b) (c)

Figure 73: (a) 90 degree rotation. (b) 180 degree rotation. (c) 270 degree rotation.

Zernike polynomials for the two techniques. The defocus values for both techniques are less than λ/20 which is good since this indicates that the correct base sphere was indeed removed in the case of the index liquid technique. It also indicates that the confocal position for the TWG interferometer was very close to the null position. The differences in the magnitude between the Zernike coefficients can be due to interferometer bias, re-trace and masking errors in the TWG as well as the MZ interferometer. The difference in the asymmetric Zernike coefficients can alos be due to different rotational orientations when the part was tested on the TWG compared to the MZ interferometer. These errors with respect to the index liquid technique will be explored in the uncertainty analysis section.

Micro-Pyramid Testing

As previously mentioned, we would also like to investigate how the index liquid technique can be used to measure non-spherical microstructures [113]. To this end, we interacted with Reflexite, a company that specializes in the fabrication of retro-reflective materials, namely glass beads and micro-prism arrays. The main applications of these materials are as visibility enhancers for a variety of products. Figure 74 shows the comparison of interferograms obtained with and without the use of an index liquid when measuring a micro-pyramidal array. Notice that without the index liquid the fringe

Table 6: 2nd Order Zernike comparison between TWG and MZ interferometer.

2nd Order Zernike Coefficients	TWG	MZ (index liquid technique)
Defocus (waves)	-0.0076	-0.03
Astigmatism, axis at 0° or 90° (waves)	-0.01564	0.12172
Astigmatism, axis at 45° (waves)	-0.08578	0.01850
3rd order coma along y-axis (waves)	-0.37236	0.29753
3rd order coma along x-axis (waves)	-0.33312	-0.40142
3rd order spherical aberration (waves)	-0.21111	-0.20635

density is too large to allow a phase measurement. The objective was to enable measurements of arbitrary geometries and to reduce testing time compared to profilometry. Measurements were again taken on the phase-shifting Mach-Zehnder

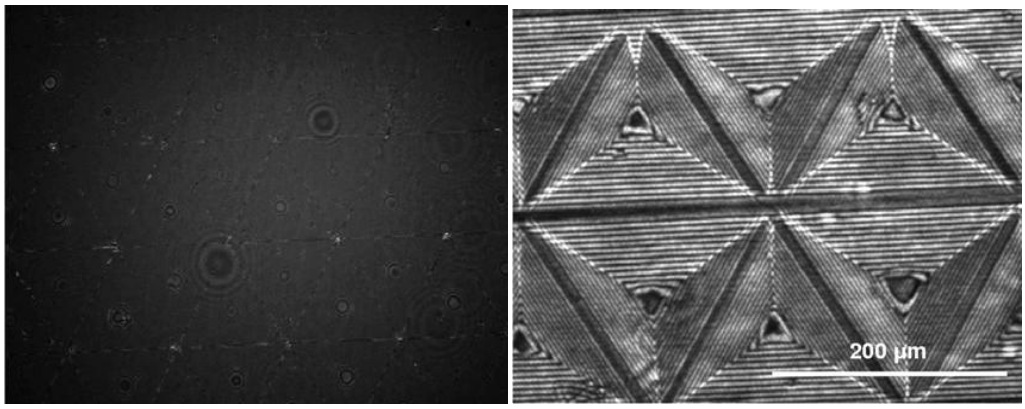

(a) (b)

Figure 74: (a) Interferogram of plane wave illumination on micro-pyramid array using no index . (b) Interferogram of plane wave illumination on micro-pyramid array obtained using an index liquid.

(MZ) interferometer (λ = 0.6328 μm) housed at the University of Vrije in Brussels, Belgium. The technique was demonstrated by measuring a micro-pyramidal array that was fabricated by Reflexite Corporation. The pyramidal array was made out of acrylic

with a refractive index of 1.58, and a nominal length (a side of the base of the pyramid) of 200 μm, and nominal height of 100 μm. An index liquid (Cargille Laboratories) with a refractive index of 1.47 was chosen to measure the micro- pyramid array. The index liquid is placed between a microscope glass slide and the micro-pyramid array as shown in Figure 75.

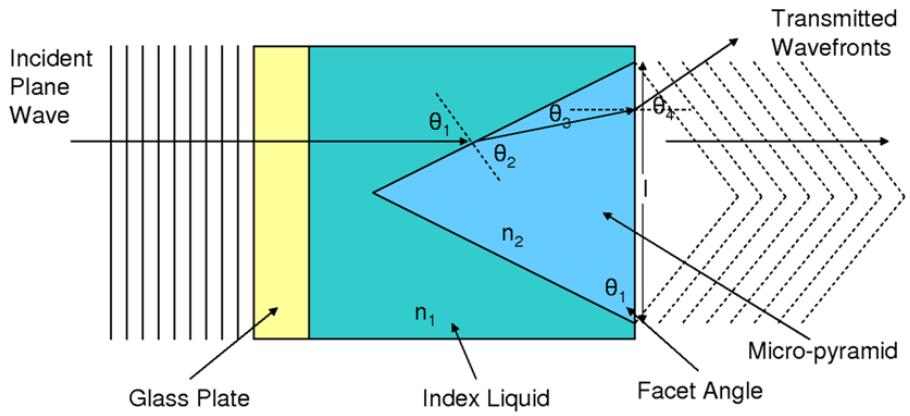

Figure 75: Schematic of micro-prism measurement set-up.

In order to measure a significant portion (0.6 mm^2) of the micro-pyramidal array, a 10X imaging microscope objective was used that has a NA of 0.2, a paraxial focal length of 45 mm, and a working distance of 5 mm. Because the depth of field is much less than the micro-pyramidal height, only a portion of the micro-pyramidal array was in focus. The interferometer is adjusted so the aperture (base) of the micro-pyramid under test is sharply in focus [64]. Edge diffraction was most significant at the pyramid base, so focusing on the base rather than another part of the pyramid yielded the best measurement. This avoids Fresnel diffraction patterns which may interfere with the phase-shifting algorithm. However, the top edges of the micro-pyramid are still susceptible to Fresnel diffraction patterns. A lower magnification and smaller NA

microscope objective could be used both to increase the depth of field and also the field of view of the array under test.

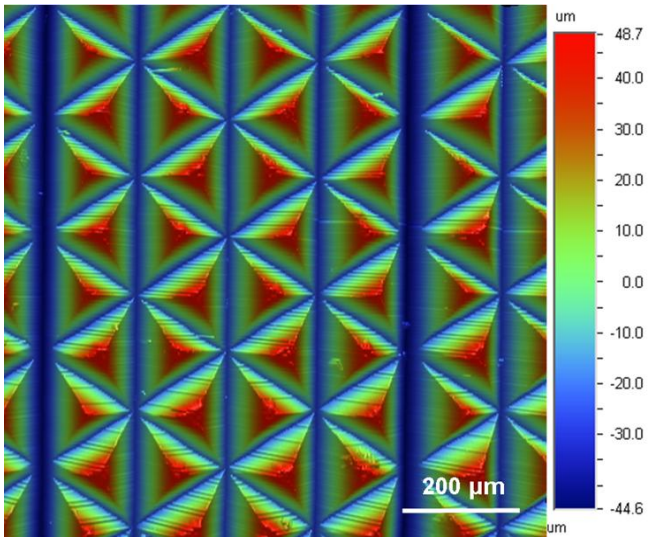

Figure 76: Surface profile obtained with the Dektak surface profilometer.

Measurements taken on the MZ interferometer were compared to measurements taken with a Veeco Dektak8 surface profilometer. The profilometer was used in a 3-D mapping mode to measure the micro-pyramidal array, see Figure 76. Due to scan speed and lateral scan resolution of the profilometer, we measured a 1 mm^2 area of the micro-pyramidal array. Figure 77 shows the surface map obtained with the MZ interferometer in the plane-wave configuration. As mentioned previously, only a 0.6 mm^2 area of the micro-pyramidal array was measured. A lower magnification objective could have been used to increase the field of view and hence measure a larger sample of the array, but this would have resulted in a reduction in lateral resolution. It was not possible to identify and measure the same region of the micro-structure with the two instruments, but we the averaged measured height, or the P-V heights were compared. The P-V height of the micro-pyramidal array as measured by the Dektak8 profilometer was 92.7 µm, and the

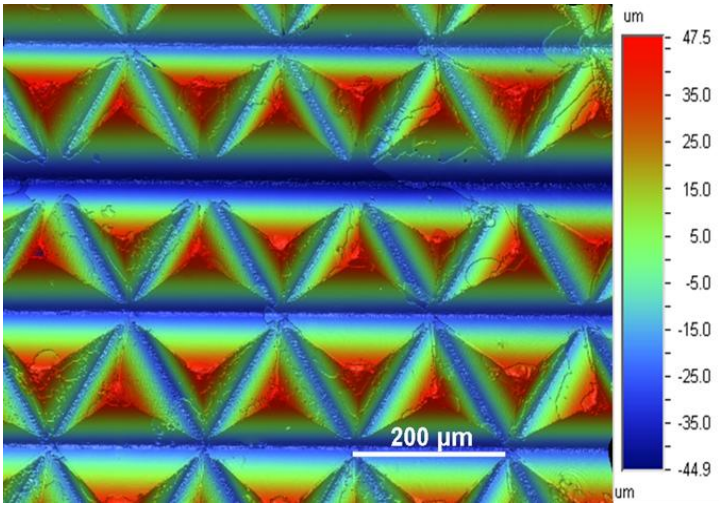

Figure 77. Surface map obtained using the MZ interferometer in conjunction with an index matching liquid.

P-V height of the micro-pyramidal array measured 93.9 µm for the index liquid technique measurement on the MZ interferometer. A smaller P-V value for the profilometry measurement is consistent with profilometry geometry limitations in reaching the lowest regions between the pyramids. It can be shown that for a tip radius of 2 µm and angle between facets of 70 degrees, that 0.86 microns of the 1.2 µm difference can be attributed to this effect. These results show good agreement between the MZ interferometer and profilometer. To extract the facet angles of the micro-pyramidal array, the surface profile map from the Dektak profilometer and the optical path difference map from the MZ interferometer are both imported into Vision32 [52]. The polygon mask feature was used to mask each facet, and this was done for both the profilometer and MZ data. Figure 78 shows an example of the polygon mask implemented for the MZ data in Vision32. The main goal of the polygon mask is to separate the three facets that make up each micro-pyramid so that the facet angle of each could be calculated. The masked data was then imported into Matlab. A best-fit plane is fit to the lowest regions between the pyramids

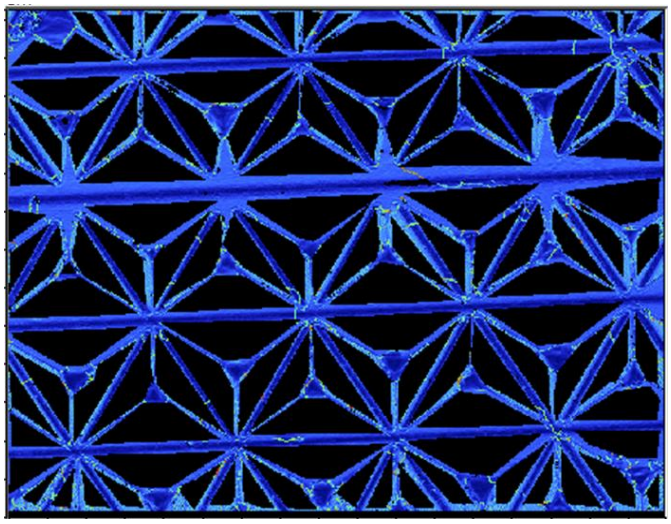

Figure 78: Polygon mask for MZ index liquid data.

by masking out the micro-pyramids themselves. This best-fit plane is then removed from the data; therefore the base of the pyramid is now the plane against which the facet angles of each micro-pyramid will be defined. The masked data after importation into Matlab is then converted into a binary image using various image processing algorithms. Each facet in the micro-pyramidal array is subsequently labeled by number. Figure 79(a) and (b) illustrates the masked binary image as well as the numbered facets in the micro-pyramid array. Each numbered facet in the binary image is first selected and then multiplied by the surface map in Figure 77. An example of the facet angle labeled 1 is shown in Figure 80. The facet angles for all labeled facets are recovered by fitting each facet to a plane which gives the gradient of the facet in both directions *(dx, dy)*. Equation 61 is then used to recover the fact angle of each facet.

$$\theta_4 = \tan^{-1}\left(\sqrt{dx^2 + dy^2}\right) \tag{61}$$

Equation 55 is then used to calculate the true facet angles (θ_1) for each facet. This is done for all facets in the micro-pyramidal array. Figure 81(a) and (b) depict the facet angle

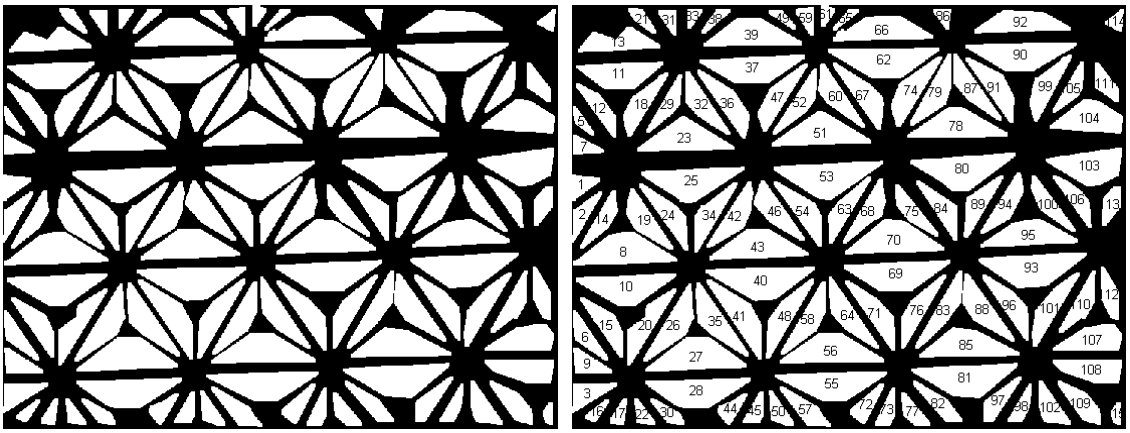

(a) (b)

Figure 79: (a) Binary image of masked MZ data. (b) Labeled facets.

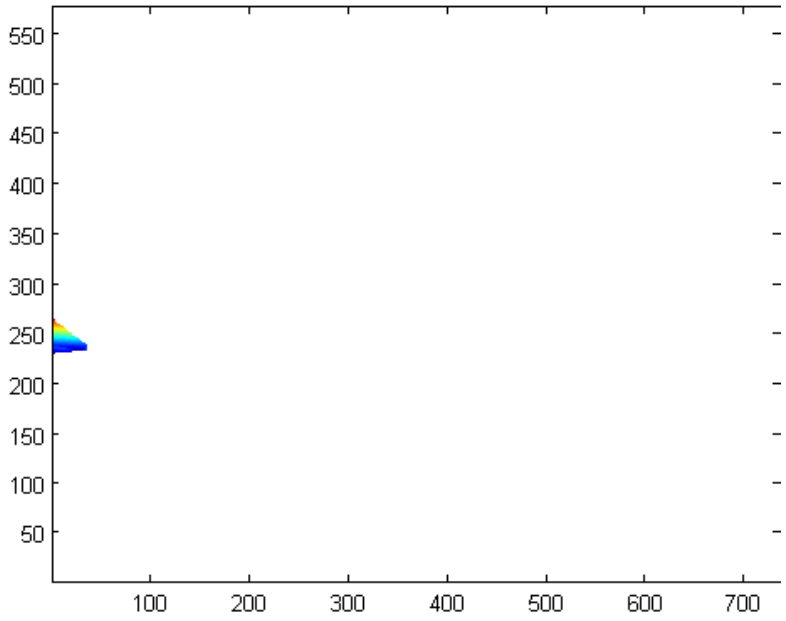

Figure 80: Example of extracted facet angle.

maps obtained with the Dektak profilometer and MZ interferometer, respectively. Table 7 compares the results for both measurement procedures. The maximum, minimum, and average facet angles are in good agreement between the profilometer and MZ measurements. By observing the facet angle map as well as the minimum and maximum values in Table 7 we see that the profilometer consistently measures higher and lower

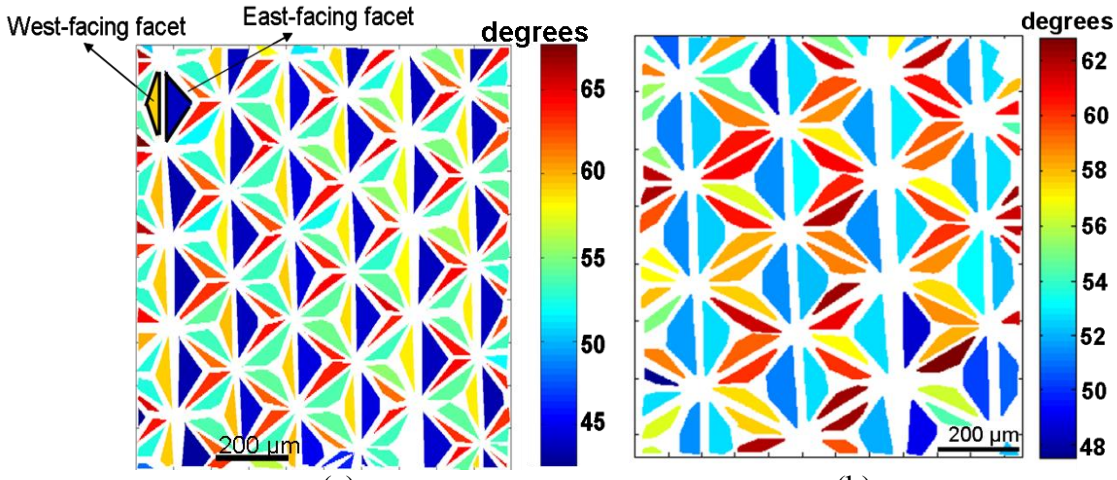

(a) (b)

Figure 81: (a) Facet angle map of micro-pyramid array obtained with the Dektak surface profilometer. (b) Facet angle map of micro-pyramid array obtained with MZ interferometer.

Table 7: Comparison between MZ interferometer and profilometer.

	MZ Interferometer (degrees)	Dektak Profilometer (degrees)
Average	55.2	53.3
Std	4	7.2
Max	62.8	67.7
Min	47.5	42.5
Range	15.3	25.2

facet angles than the MZ interferometer. This is due to the arcing motion that occurs when the stylus of the profilometer pivots and swings vertically during a scan. This arcing motion can produce errors in slope measurements as the stylus rides up one side of the slope and down the other [52]. This effect can clearly be seen by looking at the upper corner of Figure 81. This figure focuses on two adjacent facets from the profilometer

data, in which the stylus rides down the east facing facet and up the west facing facet, in a horizontal direction in multiple scans. Although adjacent to each other, these facets differed by approximately fifteen degrees, which is a very large difference. In this case the arc motion errors tend to lower the facet angle of the east facing facet from its actual value. Also, the west facing facet tends to be higher than its actual value. For comparison, adjacent facets on the MZ interferometer only varied by three degrees. These arc motion errors can be compensated to an extent depending on the slope of the artifact under test by implementing various algorithms or filters, none of which were applied to the profilometer data.

Because of the lateral resolution and scan length, the Dektak profilometer took six hours to measure the 1 mm^2 area of the micro-pyramidal array. On the other hand, the measurement time for the MZ interferometer was only 5 seconds. This disparity in measurement times makes the index liquid technique more suitable to high volume manufacturing processes where measurement speed is critical.

Micro-corner cube Testing

As a final example, it can be shown that the index liquid technique can be used to measure a micro-corner cube array with concave pyramidal micro-cavities. Interferometric measurements of these types of micro structures have not been shown previously in literature to our knowledge. These micro-corner cube arrays were fabricated at the University of Bremen from nickel using a new diamond micro chiseling process that produce these arrays with hexagonal apertures [94]. These structures could not be measured on the Dektak8 profilometer, because the probe tip would easily damage the surface and compromise the reflection efficiency of these structures. Because our

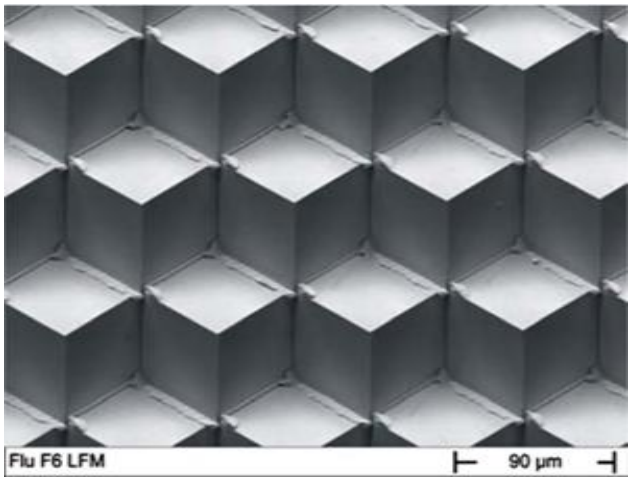

Figure 82: SEM image of micro-corner cube array fabricated at University of Bremen.

measurement works in transmission it is necessary to replicate this structure with a transparent material and measure the replicated structure. We used poly(dimethylsiloxane) PDMS (n = 1.430) for the replication, a widely used optically transparent polymer known for its excellent repeatability and reproducibility in replicating micro-structures [114]. This replication procedure is a low-cost alternative to other exotic procedures [115]. The replicated micro-cube corner array was measured with an immersion liquid with an index of 1.47. Figure 82 shows an SEM image of the micro-corner cube array. Figure 83 a) and b) show the interferogram and surface maps respectively, measured using the MZ interferometer. The forthcoming analysis of these micro-corner cube arrays is quite different from that used for the micro-pyramidal array due to the fact that unlike the micro-pyramidal array, the micro-corner cubes are structured and packed in such a way that there is no clear reference plane or substrate. Hence, calculating the facet angles relative to some reference substrate would not make sense in this case. Secondly, micro-corner cubes due to its very nature should have 90 degree apex angles, in order to reflect light back on itself if used in retro-reflector

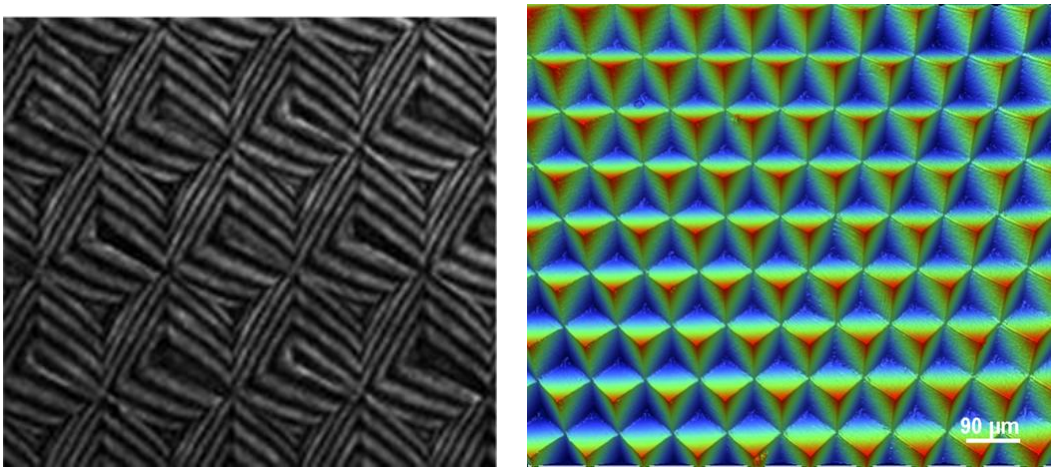

Figure 83. (a) Interferogram of micro-corner cube array measurement. (b) Surface profile of replicated micro-corner cube array obtained with MZ interferometer in conjunction with an index matching liquid.

applications. Hence, a necessary analytical study is to calculate the angles between neighboring facets in a corner-cube structure. This can be done with the same image processing algorithms and equations used previously for the micro-pyramid example. In this case we make use of the following equation

$$\cos\theta = \frac{|n_1 \cdot n_2|}{\|n_1\|\|n_2\|}, \tag{62}$$

where n_1 and n_2 are normal vector to the adjacent facets and θ is the apex angle between the two planes. Figure 84 shows the mask used to separate five randomly selected micro-corner cubes. Each facet in the micro-corner cube is numbered in a systematic way for ease of analysis. Also, to keep the results streamlined and easily comprehensible, each facet is color and letter coded. This is illustrated in Figure 85. Therefore facets *1, 4, 7, 10, 13* are all colored light blue and lettered *A*. Facets *2,5,8,11, 14* are colored red and lettered *B*, and so on. contains the angles between each facet for the five selected micro-cube corner arrays. $A \llcorner B$ means the apex angle between facet *A* and facet *B*. Note that in

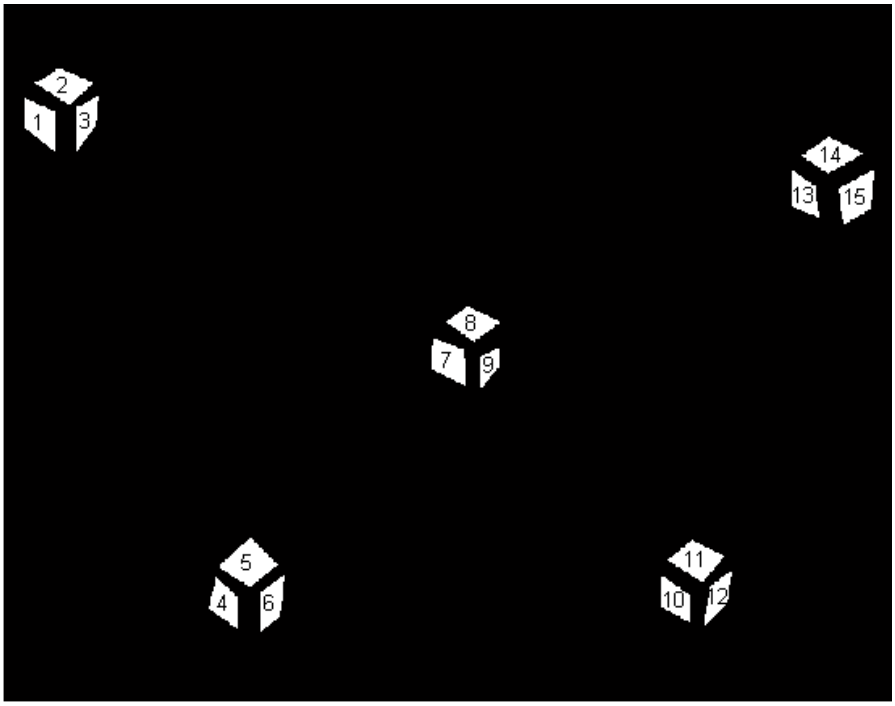

Figure 84. Mask used for analysis of five randomly selected micro-corner cube arrays with its numbered facets.

some instances the angles between facets can differ by as much as 10 degrees from a nominal apex angle of 90 degrees whereas, there are apex angles that differ by as little as 1 degree. In these cases, one can expect the reflection efficiencies to be higher.

So far it was shown that the index liquid technique demonstrates very good agreement with well established techniques such as white light and TWG interferometry in measuring sag, diameter, ROC and form errors of a micro-lens. The index liquid technique was also shown to have good agreement with a Dektak profilometer in measuring the facet angles of a micro-pyramid array.

Micro-lens Array Testing

The index liquid technique can be expanded further by measuring several micro-lenses in an array at once, similar to what was done for the micro-pyramid array. In the following section, it is shown that some of these same parameters such as sag, ROC and

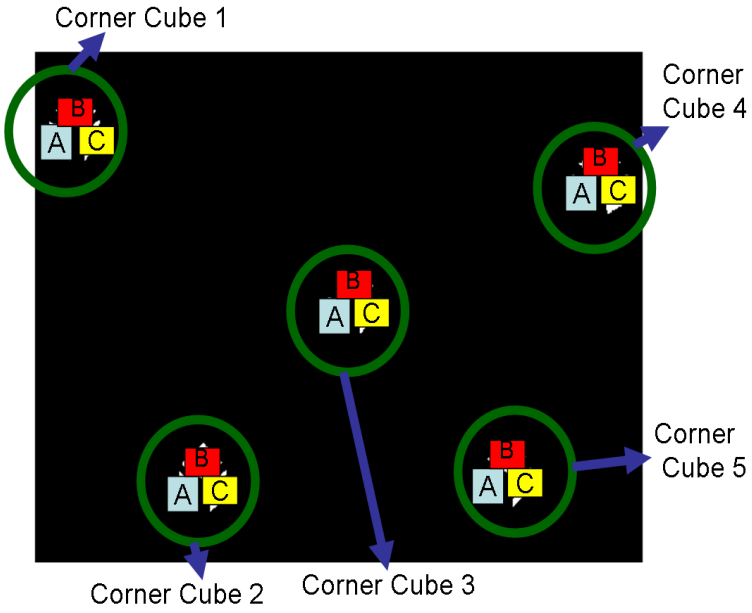

Figure 85: Diagram illustrating the color and letter format for each micro-corner cube.

Table 8: Angles between facets for micro-corner cubes.

	A∟B	B∟C	A∟C
Corner cube 1	93.07	97.91	95.58
Corner cube 2	95.06	99.96	96.19
Corner cube 3	93.16	96.31	95.59
Corner cube 4	92.31	95.93	95.20
Corner cube 5	92.63	98.00	90.88

form errors could be measured simultaneously on an array of micro-lenses by implementing various image processing techniques.

A fused silica micro-lens array donated by Vrije University was used instead of the micro-lens array from DOC due to the fact that the pitch of the Vrije lens array was

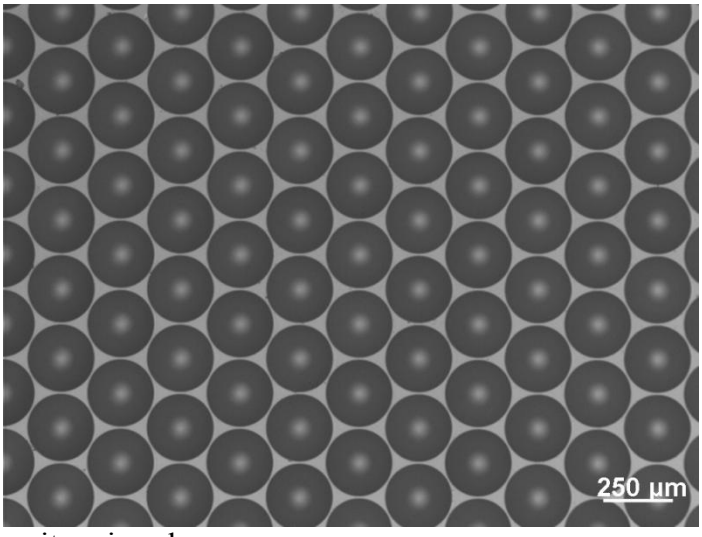

Figure 86: Vrije University micro-lens array.

0.250 mm whilst that of the DOC array was 1.00 mm. Therefore, more micro-lenses from the Vrije array can be measured in the field of view (5X objective) than the DOC micro-lens array. Figure 86 shows the image of the Vrije micro-lens array. Notice the hexagonally packed array. This array has nominal sag of 20 μm with a nominal ROC of 400 μm and a nominal diameter of 250 μm. Figure 87 shows an interferogram for the Vrije micro-lens array tested with and without an index liquid using the MZ interferometer under plane-wave illumination. Without the index liquid, the fringe density is too large to be measured. Figure 87b shows the observed interferogram when certified water (n=1.333) is applied to the surface. One can immediately see that the fringe density is greatly reduced and hence many structures can now be measured. Figure 88 illustrates the contour map of the micro-lens array as measured with an index-liquid of 1.33. The PV height of this array was 19.995 μm. If this micro-lens array was to be used in an application such as integral imaging in which the whole array was functional, the uniformity of the micro-lenses in the array becomes of paramount importance. To

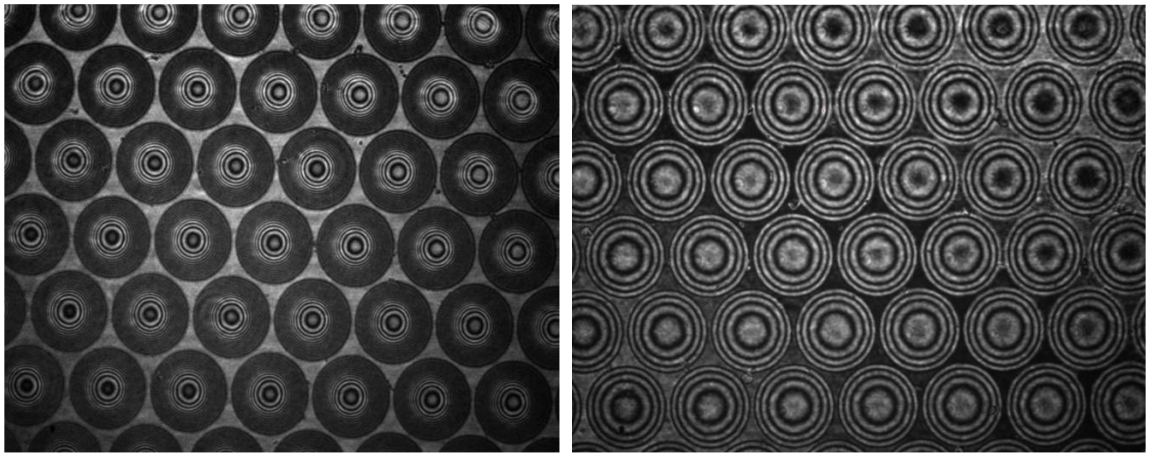

Figure 87: (a) Interferogram for micro-lens array with 20 μm sag tested in air. (b) Interferogram for micro-lens array with 20 μm sag tested with water as the index liquid.

investigate this, the same image processing algorithms that were applied to the micro-pyramid analysis, were used to calculate the uniformity of the some of the important micro-lens parameters such as sag, ROC, and form errors. Figure 89, Figure 90, and Figure 91 illustrates the sag, ROC and PV deviation from a sphere map respectively of the Vrije micro-lens array. Table 9 outlines the uniformity and statistical results for the various micro-lens parameters. Figure 92 shows the form error map for the Vrije micro-lens array. It is interesting to note that higher order spherical aberration dominates these maps. In fact, if one looks at the Zernike terms for one of these maps, it is clearly seen that 4th and 5^{th} order spherical aberration are the main contributors (Figure 93).

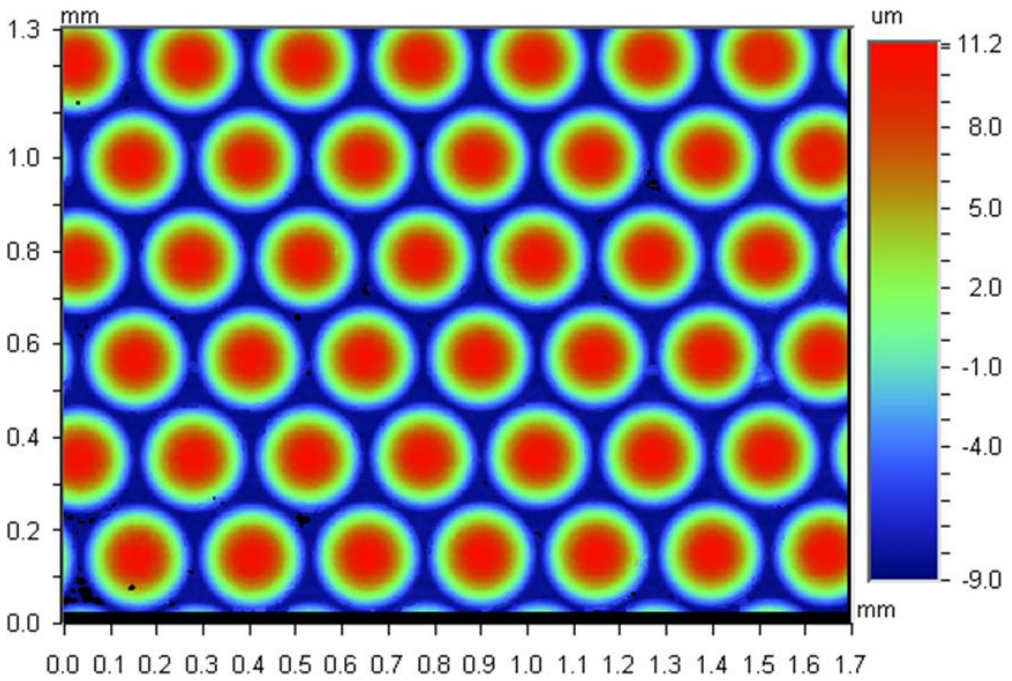

Figure 88: Contour map of the Vrije micro-lens array using the plane wave geometry in the MZ interferometer with water as the index material.

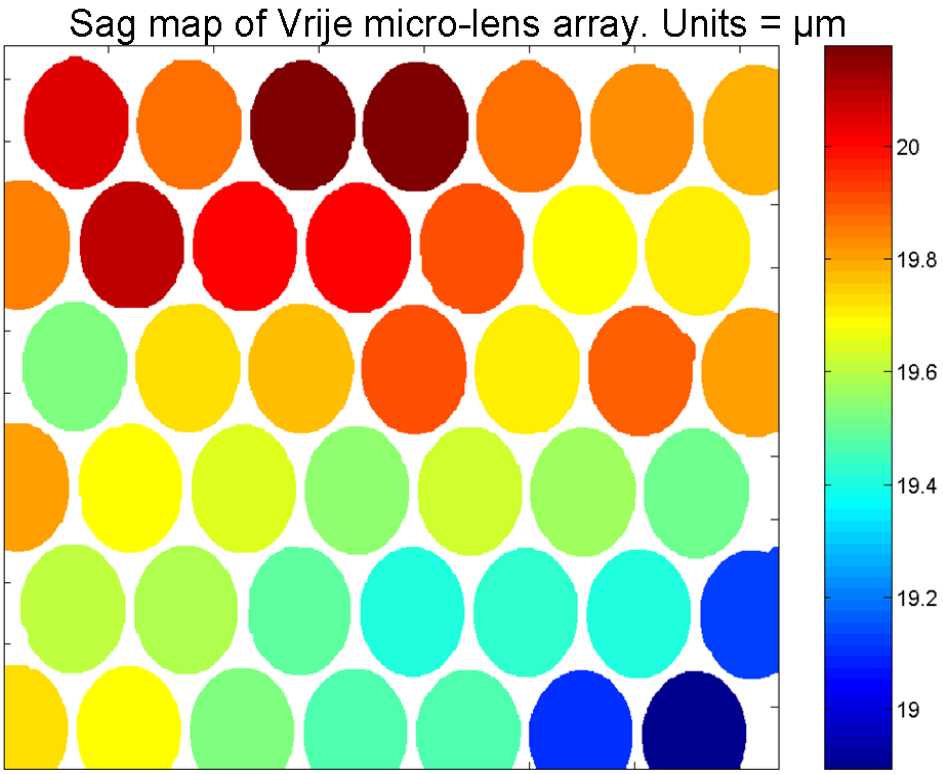

Figure 89: Sag map of the Vrije micro-lens array.

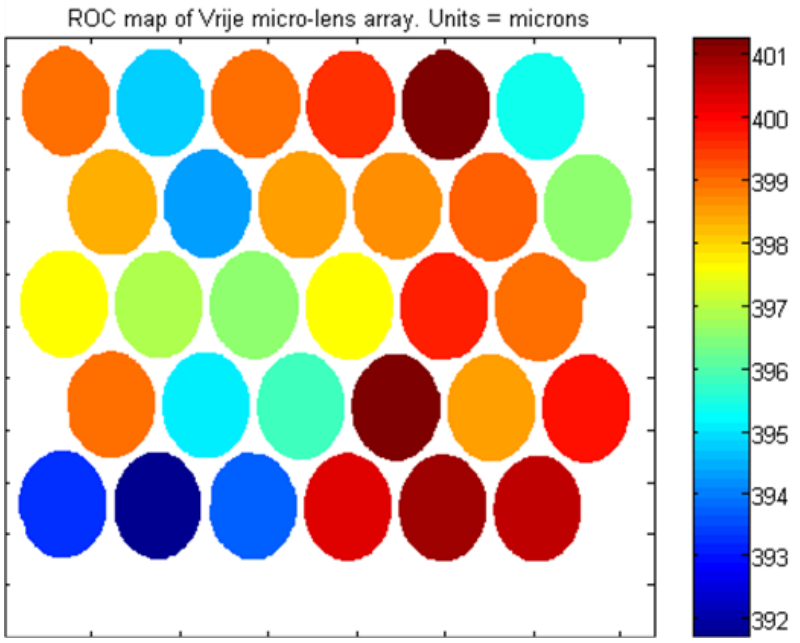

Figure 90: ROC map of Vrije micro-lens array.

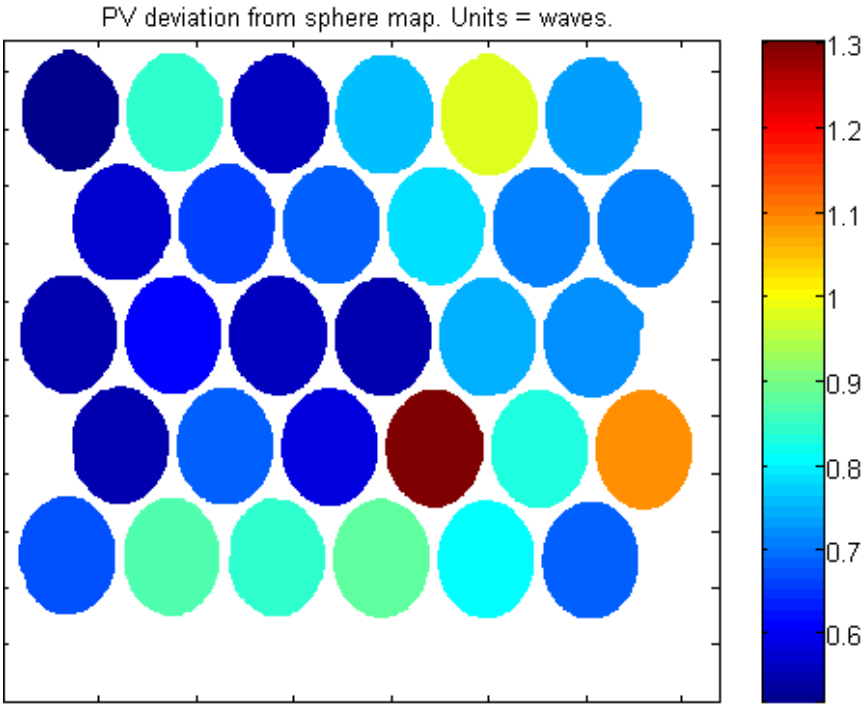

Figure 91: PV deviation from sphere map for Vrije micro-lens array.

Table 9: Summary of statistical results for micro-lens parameters.

	PV (microns)	ROC (microns)	PV deviation from sphere (waves)
Max	20.43	401	0.88
Min	19.22	392	0.52
Range	1.20	9	0.36
Average	19.79	398	0.69
Uniformity	6%	2.4%	52%

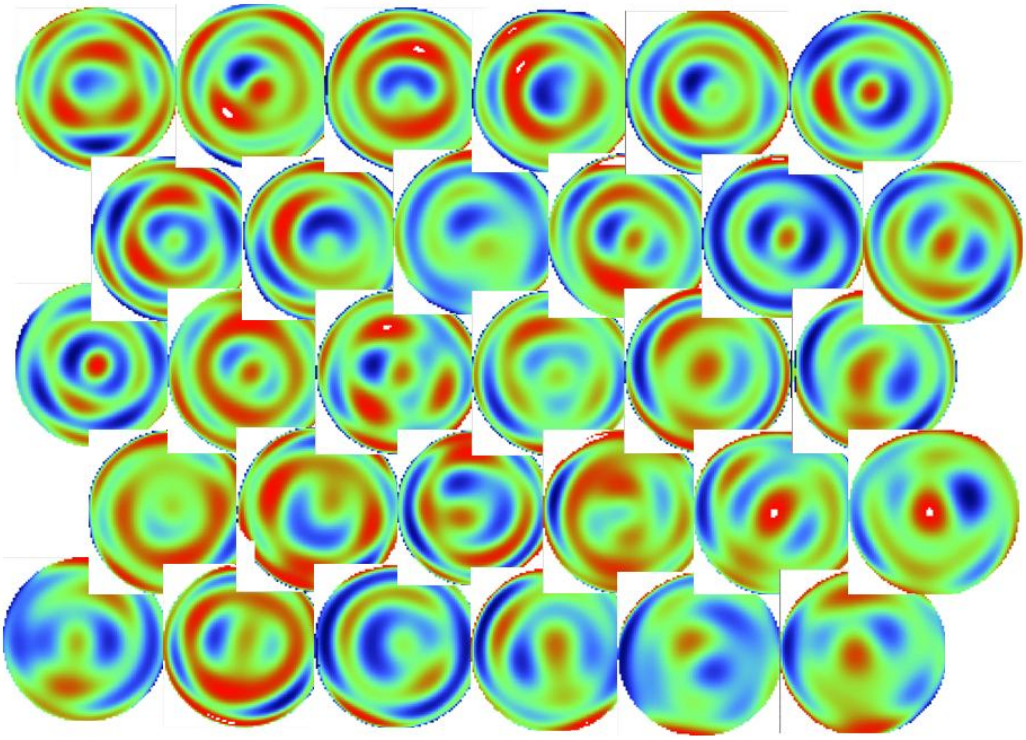

Figure 92: Form error map of Vrije micro-lens array.

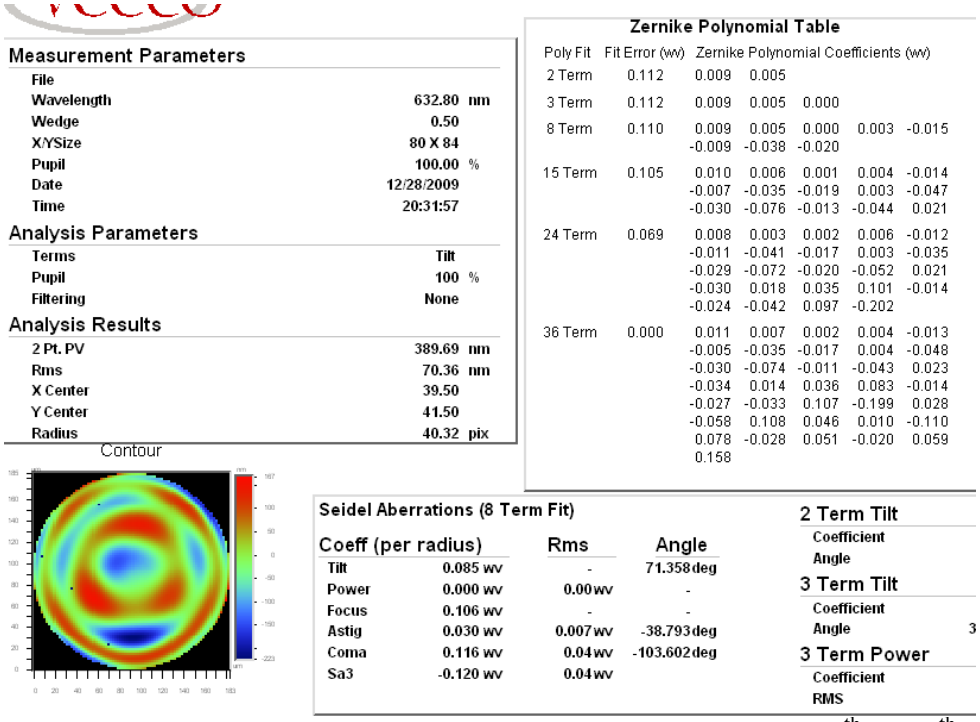

Figure 93: Zernike coefficients showing form error map dominated by 4th and 5th order spherical aberration.

CHAPTER 5: UNCERTAINTY ANALYSIS

In this chapter, we will explore the accuracy of the index liquid technique by performing an uncertainty analysis that treats the case for measuring both the sag of a micro-lens and the facet angle in the micro-pyramid. This chapter also explores some of the higher order effects that may affect the measurement, such as interferometer bias, refraction and retrace errors.

In Chapter 2, equations 43 and 55 described equations relating the sag and facet angle to the refractive index of the liquid, refractive index of the sample, as well as the *OPD* map of the sample and the slope of exiting wavefront. To understand the uncertainty in measuring the sag of a micro-lens as well as the facet angle of a micro-pyramid, one can propagate the uncertainties in the measured variables, namely n_1, n_2, *OPD*, θ_4 to determine the uncertainty in the dependent variable *sag*, and θ_1. This is done by expanding *sag* or θ_1 about the measured variables in a Taylor series [116]. The combined standard uncertainty, for example the sag of a micro-lens, $u_c(sag)$, as defined by the International Organization for Standardization is the positive square root of the combined variance $u_c^2(sag)$, which is given by [117]

$$u_c^{\,2}(sag) = \sum_{i=1}^{N} \left[\frac{\partial f}{\partial p_i} \right]^2 u^2(p_i), \tag{63}$$

where f is a function relating for instance the sag of a micro-lens to parameters n_1, n_2, *OPD*, θ_4. This relation can be accomplished by combining equations 43-44 to get l/

$$sag = \frac{OPD\left[\frac{n_2^{\,2} - 1 + \cos(\theta_4)^2}{n_2^{\,2}}\right]^{1/2}}{\left(\frac{n_2 - n_1}{1}\right)\left[\frac{n_2^{\,2} - 1 + \cos(\theta_4)^2}{n_2^{\,2}}\right]^{1/2}} \tag{64}$$

Each $u(p_i)$ in equation 63 is the standard uncertainty of the parameters n_1, n_2, OPD, θ_4 which can be evaluated with a Type A or Type B analysis. Type A evaluation is based on a statistical analysis of a series of observations, while a non-statistical analysis is considered a Type B evaluation [117].

Micro-lens Sag Uncertainty

The uncertainties in the refractive index of the liquid and micro-lens sample were evaluated from the manufacturer's specifications and hence fall under Type B evaluation. The uncertainty due to the *OPD* is related to the phase of the micro-lens under test which is recovered from phase-shifting techniques. There are numerous sources of error that affect the accuracy of phase measurements determined by the phase-shifting algorithms. These errors are well documented in the literature through simulations and experimental results [7, 118]. However, most of these error sources assume a systematic error. Random errors that affect phase-shifting interferometry can be quantified by repeatability tests which fall under Type A evaluation. Hence in quantifying the uncertainty in the OPD both Type A and Type B evaluations are undertaken. The slope of the exiting wavefront θ_4, depends on the lateral calibration of the MZ interferometer since this is used to calculate the gradient and hence slope of the wavefront. This lateral calibration was measured under repeated measurements using a circular calibration standard in conjunction with a software line mask. This therefore was a Type A evaluation.

The index liquids used came with a specification sheet which provided information on both optical and physical properties of the index liquid. These useful sheets contained a Cauchy dispersion equation, the refractive index and percent transmittance at various wavelengths, the temperature coefficient of refractive index, stability information, compatibility (with common plastics, rubbers, and metals), coefficient of thermal expansion, solubility with various solvents, and more. The refractive index for each liquid is specified at a specific wavelength (589.3 nm) and temperature (25^0C). For optical liquids, it is found that as wavelength goes up, refractive index goes down. Higher refractive index liquids tend to have higher dispersion.

Using the Cauchy dispersion equation, the refractive index of the liquid at the test wavelength of 0.6328 μm can be calculated. The uncertainty in the refractive index due to wavelength variation in the laser source can also be calculated from the dispersion equation. Another parameter that affects the refractive index is the temperature coefficient of the index liquid. The temperature coefficient (the change in refractive index for a given change in temperature) for liquids is always negative, almost always much larger than for solids, and almost always around -0.0004 refractive index units per degree centigrade. The accuracy of the refractive index value for a liquid is dependent on the accuracy and control of the temperature.

The Cauchy dispersion equation can be written as follows:

$$n(\lambda) = A + \frac{B}{\lambda^2} + \frac{C}{\lambda^4}, \tag{65}$$

where n is the refractive index, λ is the wavelength, A, B, C, etc., are coefficients that can be determined for the liquid by fitting the equation to measured refractive indices at known wavelengths. The coefficients were provided by Cargille Labs for each index

liquid. Table 10 illustrates the refractive index of the liquids used primarily in testing for this dissertation at the test wavelength at 0.6328 μm as well as the coefficients *A, B, C*.

Table 10: Refractive index and coefficients of index liquids.

λ @ 5839 Å, 25^0C	λ (@6328 Å)	A	B (Å^2)	C (Å^4)
1.33	1.3313	1.322412	383859	-1.142157E+12
1.47	1.4682	1.4567807	440231	6.542733E+11
1.80	1.7897	1.72220029	2736316	-9.610705E+11

The variance in the refractive index of the liquid which depends on both dispersion and temperature can be calculated according to the "law of propagation" as [117]:

$$u_n^{\,2} = \left[\left(\frac{\partial n}{\partial \lambda}\right)u(\lambda)\right]^2 + \left[\left(\frac{\partial n}{\partial T}\right)u(T)\right]^2 \qquad (66)$$

.

The first part of equation 66 can be evaluated from the Cauchy dispersion relation. The second part of equation 66 involves the temperature coefficient and is specified within a range of 15^0C – 35^0C by the manufacturer. The average temperature of the room which houses the MZ interferometer was 20^0C. The temperature in the room also varied by as much as 1^0C during the day, and we can take this value as the uncertainty in the temperature since a rigorous check of temperature was not done every time a measurement was taken. The temperature coefficient for 1.80 index liquid as given by the spec sheet is -7.11x$10^{-4}/^0$C. Hence the refractive index of the index liquid at 20^0C is given by

$$n_{20^0C} = 1.7897 + \frac{\partial n}{\partial T}(T - 20^0 C), \tag{67}$$

where T is the measurement temperature. Therefore the refractive index of the index liquid becomes 1.7861. The wavelength of the HeNe laser source used in the MZ interferometer was assumed to vary by 1 part in 10^{10}. This is a very conservative estimate of the uncertainty in the wavelength since conventional frequency stabilized lasers enable the wavelength to be maintained within about 2 parts in 10^{12} for months and years of continuous operation [119]. $\delta n/\delta\lambda$ was derived for each index liquid by taking the partial derivative of equation 64 and substituting the test wavelength (0.6328 μm) and the coefficients from Table 10 into the resulting equation. Table 11 illustrate the uncertainty in the refractive index u_n of the liquid due to the uncertainty in wavelength u_λ and temperature u_T. The temperature as expected has the biggest effect on the uncertainty of the refractive index of the liquid.

Table 11: Uncertainty in refractive index of liquid due to wavelength and temperature.

n@6328Å	u_λ(Å)	$\delta n/\delta\lambda$(/Å^{-1})	Temperature Coefficient ($\delta n/\delta T$) (/^{0}C)	u_T	$u_{index\ liquid}$
1.3313	6.328E-8	-2.5795e-006	-1.04E-4	1^{0}C	-1.04E-4
1.4682	6.328E-8	-3.7326E-6	-3.92E-4	1^{0}C	-3.92E-4
1.7897	6.328E-8	-2.1220E-5	-7.11E-4	1^{0}C	-7.11E-4

Similar analysis could be applied to determining the refractive index of the micro-lens sample which is made of fused silica. However, DOC provided the refractive index

of the sample as 1.4564 @ a wavelength of 0.6328 μm with an uncertainty of 7x10E-4 refractive index units.

The *OPD* of the micro-lens under test is calculated using a 5-bucket phase-shifting algorithm [49]. Error contributions specific to this algorithm has been conveniently tabulated as linear approximations due to laser source, the phase-shifter, the detector and the environment [120]. Phase-shifter errors result from both the mis-calibration of the phase-shifter and non-linearity in the phase-shifter. High-order nonlinearities caused by hysteresis in the piezo-electric transducer (PZT) can result in measurement error in the calculation of the phase. The five-bucket algorithm used in recovering the phase of the micro-lens is insensitive to phase-shift mis-calibration [49]. Laser source instability can cause fringe pattern instability which can reduce the accuracy of the measured wavefront. However, the long coherence length of a He-Ne laser makes this negligible. Linearity in the detector, can contribute to the error in the phase calculation due to high contrast fringes which saturate the detector. Contemporary CCD cameras however, have a very large dynamic range; hence the linearity should be very close to one. Air turbulence and vibration fall under environmental errors. Vibration errors can occur though mechanical instability and can cause the fringes to 'chatter' or completely wash out. The MZ interferometer sat on top a passive vibration isolation table, hence reducing the effects of large amplitude vibrations. Air turbulence contributes a slowly varying phase error which can be minimized by reducing the time between captured frames. Thermal gradients in the structural components of the interferometer itself can also cause time-dependent changes in the optical path over the wavefront.

Combining the uncertainties in the phase-shifting error sources in quadrature according to the law of propagation of uncertainty, the resulting uncertainty in phase is ±0.012 radians, which correspond to ±0.0012 μm in the *OPD* map [121]. However, errors such as hysteresis effects in the PZT, as well as air turbulence, temperature gradient effects and quantization errors are random, and hence can affect the *OPD* map of the micro-lens sample. To assess the random error in the OPD map, ten measurements were

Table 12: Dynamic repeatability measurements of OPD

Measurement #	20Pt P-V OPD of microlens sample (μm)
1	17.258
2	17.276
3	17.253
4	17.275
5	17.298
6	17.298
7	17.302
8	17.205
9	17.252
10	17.246
Average	17.266
Standard deviation	0.0299

taken of the micro-lens sample. Between each measurement the sample was removed and placed back into the testing position. This therefore represents dynamic repeatability.

From the data in Table 12, the best estimate of the OPD is the 20pt P-V averageof the 10 maps which is 17.266 μm. The standard deviation of these ten results is 0.0299 μm. This is the Type A uncertainty estimate of the *OPD* due to random errors in the measurement process. The uncertainty due to the systematic errors in phase-shifting interferometry is so much smaller than the standard deviation of the ten *OPD* measurements, that one can ignore it and take as the uncertainty of the *OPD* (u_{OPD}) map as the standard deviation of these measurements.

The slope of the exiting wavefront θ_4, is given by equation 46 and depends on the pixel size in the *x* and *y* directions respectively. These pixels sizes can be calibrated for a specific microscope objective magnification by using appropriate calibration standards. Because equation 46 is complex, implementing error propagation may prove difficult. However the uncertainty in the wavefront slope θ_4 may be calculated by employing Monte Carlo techniques. Monte Carlo simulation is a method for iteratively evaluating a deterministic model using sets of random numbers as inputs. This method is often used when the model is complex, nonlinear, or involves more than just a couple uncertain parameters [116]. A simulation can typically involve over 10,000 evaluations of the model. When using the Monte Carlo technique for analyzing uncertainty propagation, the goal is to determine how random variation, lack of knowledge, or error affects the sensitivity, performance, or reliability of the system that is being modeled. Monte Carlo simulation is categorized as a sampling method because the inputs are randomly generated from probability distributions to simulate the process of sampling from an actual population [122]. For a successful simulation, the distribution for the inputs must be correctly represented. The output from the simulation can be represented as

probability distributions (or histograms) or in this case error bars which represent the uncertainty in the wavefront slope. The input data for the Monte Carlo simulation in this case is the lateral scale factors in the *x* and *y* directions. One can assume a normal distribution for these inputs because these inputs were obtained by repeatedly measuring the diameter of a calibration artifact.

However the uncertainty in the calibration of the *x* and *y* pixel sizes must first be determined before implementing the Monte Carlo simulation. The calibration artifact was a circular mask aperture with a diameter of 0.03007 inches (763.8μm). The uncertainty in the diameter (u_{dia}) was provided on the calibration sheet as ±1 μm. A line mask tool in the software (PSI Version 5.3 [101]) was used to measure the diameter of this mask ten times

Table 13: Calculation of lateral scale factor in *x* and *y* direction.

Measurement #	Length of line mask in x-direction (pixels)	Length of line mask in y-direction (pixels)
	663.06	683.20
	663.31	681.51
	659.56	684.15
	661.25	687.03
	660.77	686.57
	659.34	684.56
	662.19	684.14
	659.30	685.69
	661.05	682.58
	664.64	684.12
Average	661.45	684.36
std	1.83	1.72
lateral scale factor (μm/pixel)	1.15	1.12

at the appropriate magnification (10X) setting. This was done both in the horizontal (*x*) and vertical directions (*y*). The length of the line tool was recorded in pixels. Table 13 shows the ten measurements taken as well as the calculation of the lateral scale factor in

both the *x* and *y* direction for the 10X magnification. The lateral scale factor is calculated by dividing the diameter of the circular mask by the length of the line mask in the horizontal and vertical directions respectively. Notice the camera pixels are not square but rectangular. This has serious implications when examining parameters such as form error, as well will see later on in this chapter. The uncertainty in the later scale factor in the *x* and *y* directions (u_{px}, u_{py}) can be calculated as follows

$$u_{px} = p_x \sqrt{\left(\frac{u_{dia}}{D}\right)^2 + \left(\frac{u_{lx}}{L_x}\right)^2}, \tag{68}$$

where p_x is the lateral scale factor in the *x*–direction as calculated in Table 13, D is the diameter of the circular mask, u_{lx} is the uncertainty in the length of the line mask and L_x is the average value of the line mask as calculated in Table 13. The uncertainty in the length of the line mask is assumed to be the standard deviation of the 10 length measurements. An uncertainty in the lateral scale factor in the *y*-direction can also be derived similar to equation 68,

$$u_{py} = p_y \sqrt{\left(\frac{u_{dia}}{D}\right)^2 + \left(\frac{u_{ly}}{L_y}\right)^2}. \tag{69}$$

Using equations 68 and 69, the uncertainty in the lateral scale factor in the *x* and *y* directions are ±0.004 μm and ±0.003 μm respectively. Now that the uncertainty in the lateral scale factors is known, one can use equation 46 as a model for the Monte Carlo simulation. The gradient of the OPD map can be calculated by using the *gradient* syntax in Matlab. This is as follows

$$[\mathrm{f_X}, \mathrm{f_Y}] = \mathrm{gradient}(\mathrm{OPD}, \mathrm{p_x}, \mathrm{p_y}), \tag{70}$$

where f_x and f_y are the gradient in the x and y direction respectively. θ_4 can then be calculated using the following equation,

$$\theta_4 = \tan^{-1}\left(\sqrt{f_x^{\,2} + f_y 2}\right). \tag{71}$$

The random number generator in Matlab used to create the inputs (p_x and p_y) uses the following syntax for a normal distribution,

$$p_x = \left(randn(n,1) * sd\right) + mu, \tag{72}$$

where n is the sample size, sd is the uncertainty in the lateral scale factor (u_{px}) and mu is the average value of the lateral scale factor. The sample size, used for the Monte Carlo simulation was 100,000. This large sample size was chosen since the standard error is inversely proportional to the square root of the sample size [116]. Using equations 70 and 71, as well as a representative *OPD* map of the DOC sample micro-lens sample, the Monte Carlo simulation was executed. Figure 94 illustrates the histogram for the 20pt PV values for the simulated θ_4 maps. Although, there is some skewness in the histogram, it does appear to be a normal distribution. The mean and standard deviation calculation from the simulated results are 9.65 ± 9.30E-4 degrees. We are finally in a

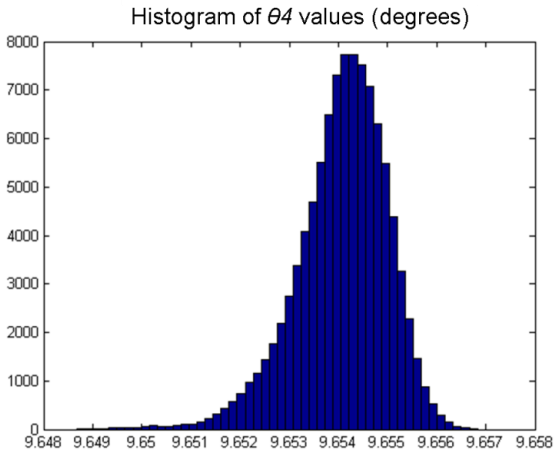

Figure 94: Histogram illustrating 20Pt P-V values for θ_4.

position to calculate the uncertainty in sag of the micro-lens measured using an index liquid with a refractive index of 1.80. Applying equation 63 to

equation 64, we get

$$u_{sag}{}^2 = \left[\left(\frac{\partial sag}{\partial n_{liquid}}\right)u\left(n_{liquid}\right)\right]^2 + \left[\left(\frac{\partial sag}{\partial n_{sample}}\right)u\left(n_{sample}\right)\right]^2 + \left[\left(\frac{\partial sag}{\partial OPD}\right)u\left(OPD\right)\right]^2 + \ldots \left[\left(\frac{\partial sag}{\partial \theta_4}\right)u\left(\theta_4\right)\right]^2, \quad (73)$$

which gives the uncertainty in the *sag*, u_{sag} of the micro-lens array. Table 14 gives the average or nominal values of the measurement parameters along with the uncertainty in each parameter and the standard uncertainty contribution to the sag for each parameter. The standard uncertainty contribution for each parameter is given by

$$\sqrt{\left(\frac{\partial f}{\partial p_i}\right)^2 \left(u\left(p_i\right)\right)^2}\ . \quad (74)$$

Table 14: Uncertainty in sag measurement.

Parameter	Average or Nominal Value	Uncertainty in Value	Standard Uncertainty
n_1	1.7861	-7.11E-4	0.12
n_2	1.4564	4.04E-4	0.07
OPD (μm)	17.27	0.03	0.09
θ_4 *(degrees)*	9.65	9.30E-4	1.67E-4
sag (μm)	52.85		0.28

Table 14 shows that the uncertainty in the sag using standard error propagation is 0.28 μm. The largest contributor is the uncertainty in the refractive index of the liquid which is

due to the temperature coefficient as well as the uncertainty of the measurement temperature. To reduce this uncertainty, an index liquid could be used with a smaller temperature coefficient or measurements can be taken in a better temperature controlled environment.

Micro-pyramid Facet Angle Uncertainty

The uncertainty in the facet angle θ_1 can be calculated by similar methods. From equations 55 and 56, we know the facet angle can be calculated using the following equation

$$\theta_1 = a\tan\left[\frac{\sin(\theta_4)}{n_1 - n_2\left(1 - \frac{\sin(\theta_4)^2}{n_2{}^2}\right)^{1/2}}\right]. \tag{75}$$

Applying equation 63 to equation 75, we get

$$u_{\theta_1}{}^2 = \left[\left(\frac{\partial\theta_1}{\partial n_{liquid}}\right)u(n_{liquid})\right]^2 + \left[\left(\frac{\partial\theta_1}{\partial n_{sample}}\right)u(n_{sample})\right]^2 + \left[\left(\frac{\partial\theta_1}{\partial\theta_4}\right)u(\theta_4)\right]^2, \tag{76}$$

which gives the uncertainty in the facet angle of the micro-pyramid array. The refractive index of the liquid (1.47) used to measure the micro-pyramid at a wavelength of 0.6328 μm is give in Table 11 as 1.4682. Taking the temperature coefficient into account, the refractive index of the liquid becomes 1.4662. The uncertainty in the refractive index liquid is given in Table 11 as -3.92E-4. The nominal value of the acrylic micro-pyramid sample was given by Reflexite as 1.58 with an uncertainty of ±0.005. The uncertainty in the slope of the exiting wavefront θ_4 is calculated using the Monte Carlo simulation which gives an uncertainty in θ_4 as 0.001 degrees. The nominal value for θ_4 was

calculated from a facet angle of θ_1 of 60 degrees, which gives a value of 10.31 degrees. Table 15 gives the average or nominal values of the measurement parameters along with the uncertainty in each parameter and the standard uncertainty contribution to the facet angle for each parameter. Table 15 shows that the uncertainty in the facet angle using standard error propagation is 0.02 degrees. The largest contributor is the uncertainty in the refractive index of the sample which was provided by Reflexite.

Table 15: Uncertainty in facet angle measurement.

Parameter	Average or Nominal Value	Uncertainty in Value	Standard Uncertainty
n_1	1.4662	-3.92E-4	1.60E-3
n_2	1.58	0.005	2.11E-2
θ_4 *(degrees)*	10.31	0.001	2.86E-3
θ_1 *(degrees)*	60		0.02

Retrace Errors

The index liquid technique is a non-null test and hence is susceptible to retrace errors. These errors occur because rays from different pupil regions in the micro-optic follow different optical paths throughout the interferometer. The aberrations induced are dependent of the part that is being tested. In the case of a micro-lens, the rays at the edge of the aperture will be deviated more due to refraction and will contribute more to the induced aberration in the interferometer than rays that pass through the apex of the lens. In order to obtain, the true test surface using a non-null test, the induced aberrations must be removed. This can be done using reverse ray tracing techniques although specific knowledge of the optics in the interferometer is needed [61]. Our goal is to quantify and correct for these retrace error experimentally in the index liquid technique. For this

purpose, the micro-optic and reflection transmission interferometer (MORTI) housed at UNC Charlotte will be used.

Since the induced aberrations caused by retrace errors increase with the slope of the surface, the magnitude of these errors in the index liquid technique can be quantified by testing the same micro-lens with different index liquids. The greater the difference in refractive index between the liquid and sample, the greater the refraction at the interface and hence the greater the slope leading to induced aberrations. Seven index liquids (1.33, 1.34, 1.35, 1.36, 1.37, 1.40, 1.43), were tested on one specific micro-lens from the sample given to us by DOC (index = 1.4564). Each index liquid measurement was repeated three times. Defocus and 3rd order spherical aberration was calculated for each surface map using the Zernike polynomial fit to the map. These are the aberrations which directly affect the sag of the micro-lens under test. A mask was used to crop the micro-lens aperture from the substrate. Figure 95 and Figure 96 show the measured dependence of defocus and 3rd order spherical aberration on the index of the liquid. The data points are the average value for each index liquid and the errors bars represent the measured repeatability (one standard deviation).. The relationship between defocus and spherical with index liquid is approximately linear. The repeatability decreases (error bars increase) as the refractive index of the liquid approaches that of the sample. This is because the measurement signal decreases (OPD gets smaller) as the liquid index approaches that of the sample. This in turn affects the repeatability of the measurement. Figure 95 shows that retrace error causes a variation of ~4.5 waves as the index liquid changes by 0.1. Similarly there is a change in spherical aberration of ~0.15 waves over the same index range (Figure 96). Retrace error goes to zero in the limit the index liquid matches that of

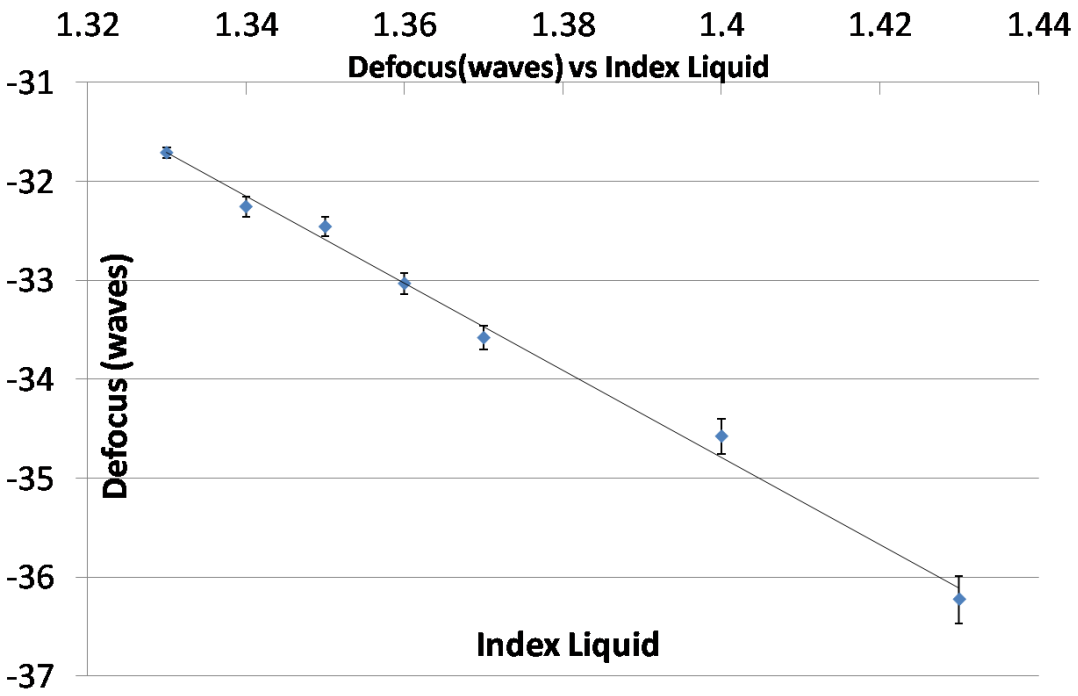

Figure 95: Defocus as a function of index liquid.

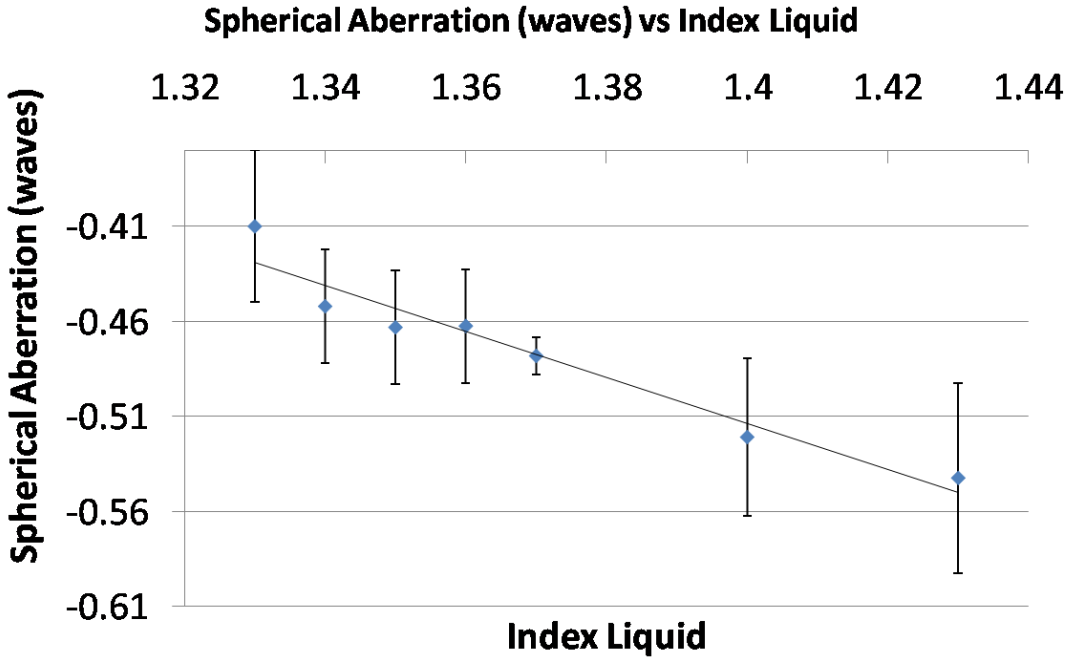

Figure 96: Spherical aberration as a function of index liquid.

the micro-lens sample, then the best-fit line to the data can be used to predict the correct value of the defocus and spherical aberration. The equation of the linear fit for defocus is given by

$$\text{defocus} = b * IndexLiquid + a, \tag{77}$$

and that for spherical aberration is given by

$$\text{spherical aberration} = b * IndexLiquid + a, \tag{78}$$

where b is the slope and a the y-axis intercept.

An uncertainty in the fit parameters leads to an uncertainty in the extrapolated defocus and spherical aberration values. The repeatability standard deviation values are taken as estimates of the uncertainties for each data point. Because the uncertainty in the defocus and spherical aberration values is different for each index liquid used, this means that standard least squares fitting algorithms cannot be used to obtain an exact fit with uncertainties in the dependent variable [123]. Hence, a weighted least squares algorithm is used to find the best fit slope and y-intercept for the data presented in Figure 95 and Figure 96 [124].

Table 16 illustrates the calculated fit coefficients which include the intercept (a), slope (b), uncertainty in the intercept (μ_a), uncertainty in the slope (μ_b) and the correlation coefficient (r) for the data presented in Figure 95 and Figure 96. Using the calculated values in Table 16, the extrapolated value for the defocus and spherical aberration coefficients can be calculated (via a Monte Carlo simulation) at the index liquid value of 1.4564, which gives the corrected defocus as -37.3 ± 3.6 waves and the corrected spherical aberration as -0.55 ± 0.4 waves. Once this calibration is completed, it can then be used to correct for retrace errors induced by any other index liquid. However, this

calibration would need to be re-done if another micro-lens with a different prescription needs to be tested. To verify these values, the same micro-lens was scanned using the 3D

Table 16: Fit coefficients for data in Figure 95 and Figure 96.

Fit Coefficients	Defocus	Spherical Aberration
a(waves)	27.0	0.65
b(waves/index units)	-44.1	-0.82
μ_a*(waves)*	2.0	0.3
μ_b *(waves/index units)*	1.8	0.17
r	0.9999	1

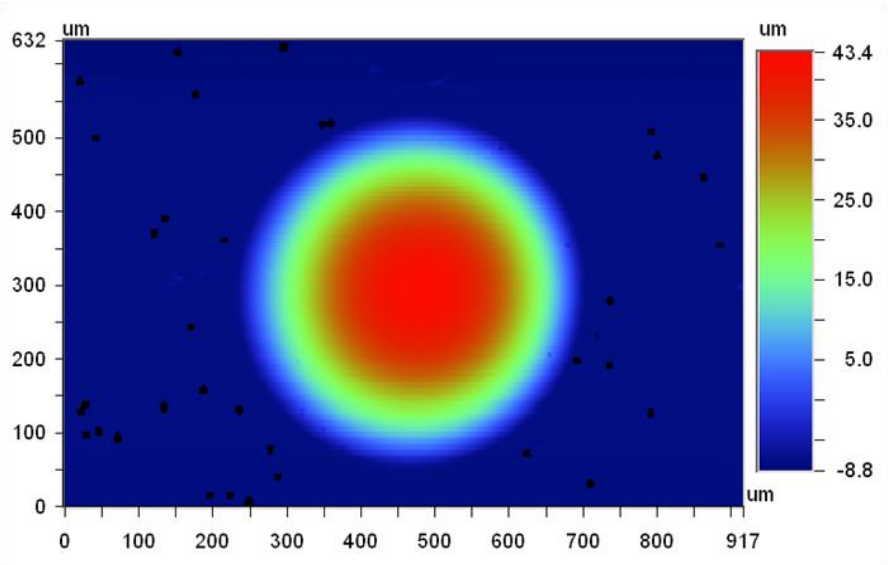

Figure 97: Surface profile of micro-lens scanned by Dektak profilometer.

feature on the Dektak profilometer. Figure 97 shows the surface profile of the micro-lens as scanned by the Dektak profilometer. Figure 98 illustrates the results of a 36 term Zernike fit to the Dektak surface profile with an aperture mask to separate the lens from the substrate. As can be seen, the defocus value for the Dektak surface profile is

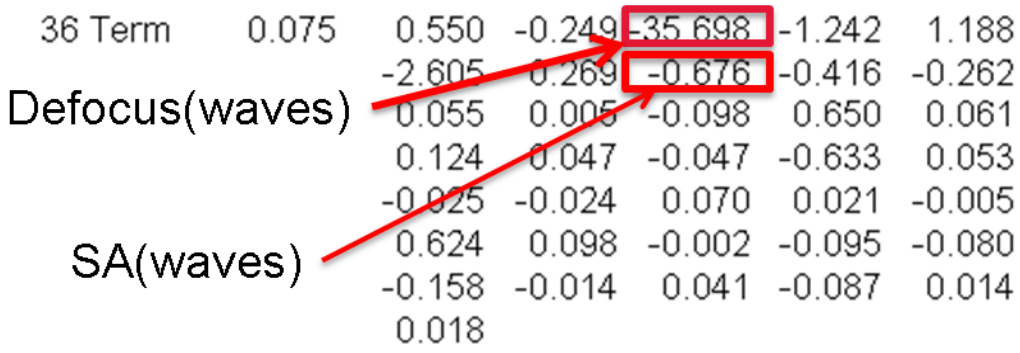

Figure 98: 36 Term Zernike fit to Dektak surface profile.

-35.70 waves and the spherical aberration coefficient is -0.68 waves. The difference between the values given by the Dektak profilometer and the calibrated index liquid measurement is within the uncertainty of the retrace error calibration values which indicates good agreement between the measurements.

To verify the sag of the micro-lens obtained by the index liquid technique, the measurement would first need to be corrected for the re-trace error bias. The re-trace error bias can be calculated from Table 16. Once this bias is calculated it can then be subtracted from the measurement to yield the corrected sag measurement. As an example, the retrace error bias for a measurement using an index liquid of 1.33 is shown in Figure 99 (b) while the uncorrected measurement is shown in Figure 99 (a). The sag of the uncorrected measurement is 54.8 μm. An index liquid of 1.33 was chose due to its relatively small uncertainty in defocus and spherical aberration compared to the other index liquids. This would then leads to an even small uncertainty in the sag calculation. After subtracting the retrace error bias the corrected measurement is shown in Figure 100. The sag for the corrected measurement is 51.8 μm. The uncertainty in the sag due to retrace errors can then be calculated from the uncertainty in the defocus and spherical

aberration values which is 51.8 ± 2 μm. The sag of the Dektak profilometer is calculated at 52.2 μm. This indicates very good agreement between the index liquid technique and

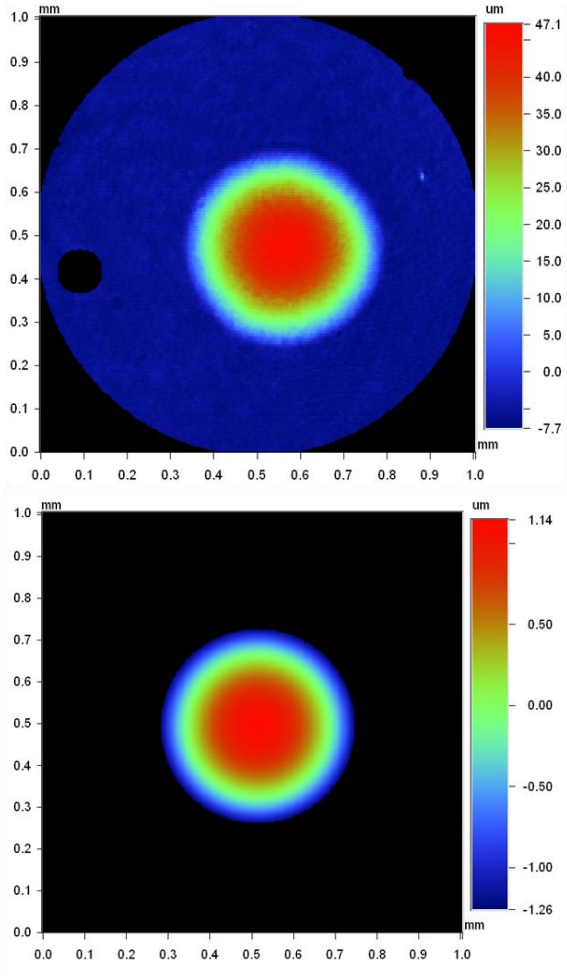

(a) (b)

Figure 99: (a) Index liquid measurement with 1.33 index liquid. (b) Retrace error bias.

the Dektak profilometer. Although the relative uncertainty in the sag obtained by calibrating the retrace error experimentally is ~4%, this method provides a viable alternative to compensating for retrace errors by reverse ray-tracing techniques. To improve the fit, the number of repeated index liquid measurements can be increased, which gives a better repeatability and hence lowers the standard deviation. Enclosing the

interferometer could also lead to a decrease in random errors caused by air turbulence and temperature gradients.

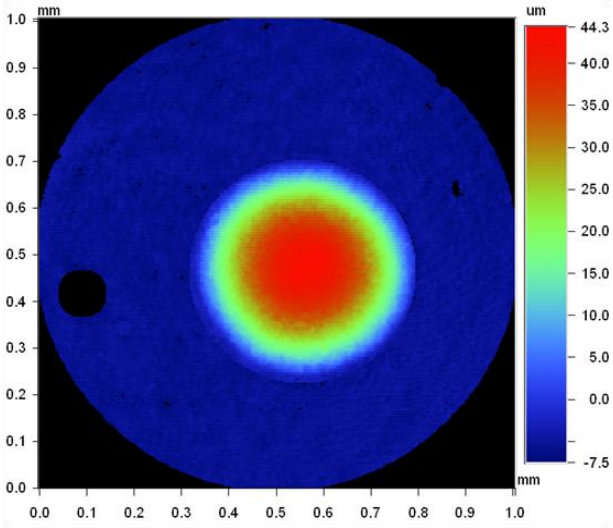

Figure 100: Correct index liquid measurement.

Interferometer Bias

It has been shown that the uncertainty in the index liquid technique due to first order parameters such as *OPD*, n_1, n_2 and θ_4, for the testing of micro-lenses and micro pyramids is negligible (<1%). However there are secondary effects that can have a detrimental effect on the accuracy of the index liquid technique if not taken into account. One of these effects is interferometer bias. For accurate index liquid measurements, the interferometer bias should be measured by removing the sample under test to outside the path of the incoming plane wavefront. The interferometer bias should then be calculated, saved and subtracted from all subsequent measurements of the micro-structure under test. If this is not done, systematic biases can affect the accuracy of the index liquid technique. The importance of subtracting the systematic bias can be proven experimentally by measuring the same specific micro-lens with different index liquids. The interferometer

bias was not subtracted for each measurement. Figure 101 illustrates the dependence of sag on the index liquid used to test the micro-lens sample. The error bars in Figure 101

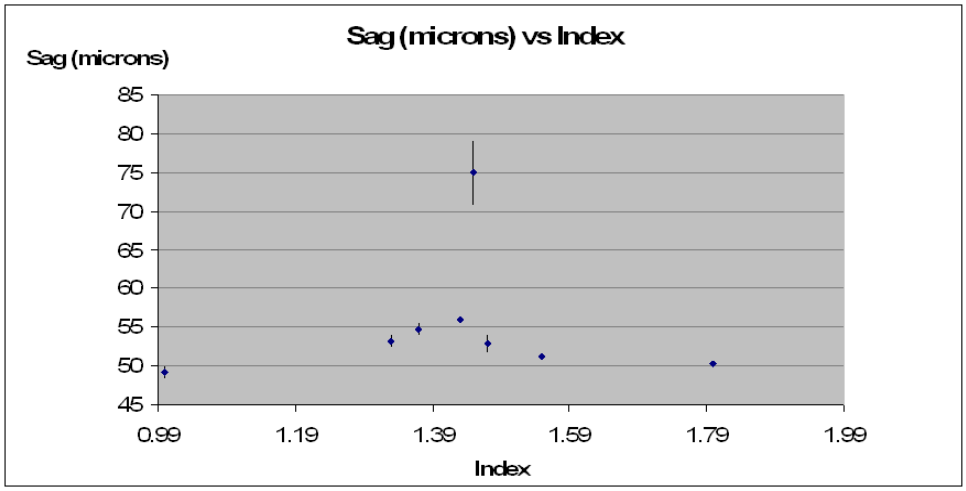

Figure 101: Dependence of sag on index liquid.

signify the standard deviation of ten measurements for each index liquid. As the refractive index of the liquid approaches that of the refractive index of the micro-lens sample (1.4564), this increases the systematic bias of the measurement. This results in an error of ~ 25 microns in the measurement of the sag of the micro-lens. Also notice that the standard deviation for each index liquid increases as the index approaches the refractive index of the micro-lens sample. To explain this phenomenon, let's first look at the interferometer bias that was measured on the MZ interferometer. This is shown in Figure 102. The interferometer bias has a PV value of ~0.160 microns and rms value of .020 microns. This may seem insignificant when compared to the sag of the micro-lens, but a closer evaluation reveals that this is not the case. If the interferometer bias is taken into account theoretically, equation 43 becomes

$$sag = \frac{(OPD_{true} + OPD_{bias})\cos\theta_3}{n_2 - n_1\cos\theta_3}, \tag{79}$$

where OPD_{true}, is the *OPD* due to the micro-lens and OPD_{bias}, is the *OPD* due to the interferometer bias. A closer examination of equation 79 reveals that as the denominator

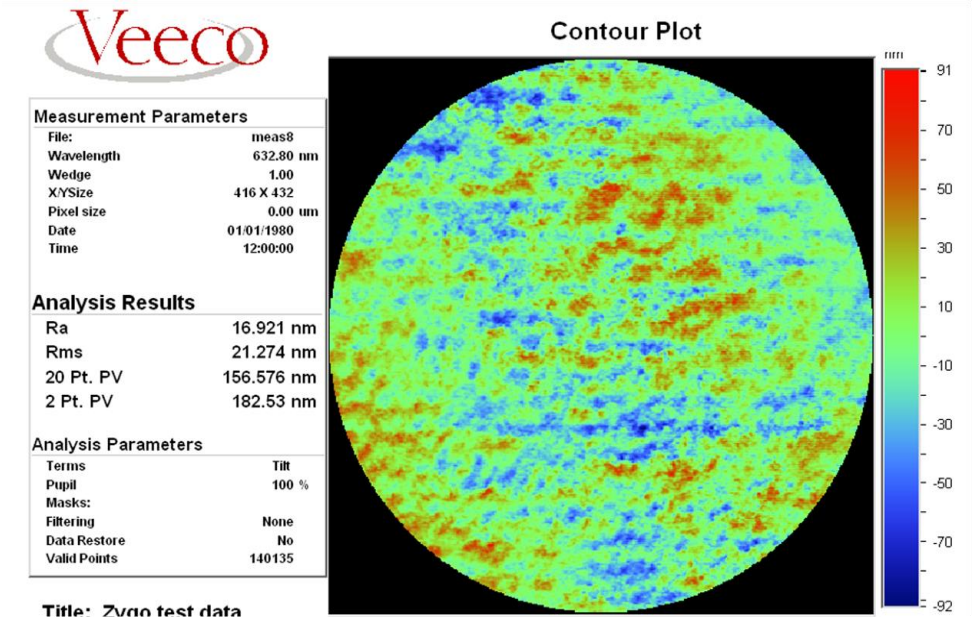

Figure 102: Interferometer bias measured on MZ interferometer.

approaches zero, the bias which stays constant is inadvertently magnified by the denominator to give an error in the sag measurement. This also explains why the measurements get less repeatable for smaller index differences because for smaller index differences, the interferometer bias dominates the *OPD* map and hence becomes susceptible to random errors such as fringe drift. Equation 79 can be visualized in Figure 103 by comparison to the experimental data, in which OPD_{bias} is given a value of 0.160 microns. From this graph one can see that the theoretical and experimental values have good agreement.

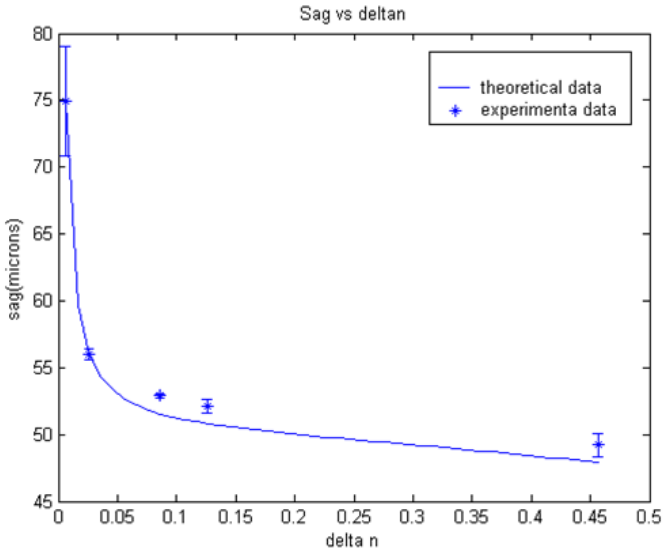

Figure 103: Experimental data compared to equation 79.

Finally, if interferometer bias is subtracted from all index liquid measurements, this results in a plot given in Figure 104. Notice how all the sag values now fall between 50 and 51.4 microns with a max percent error from the nominal value of 2.7%. This can be reduced further by examining retrace errors, which will be done later on in this Chapter.

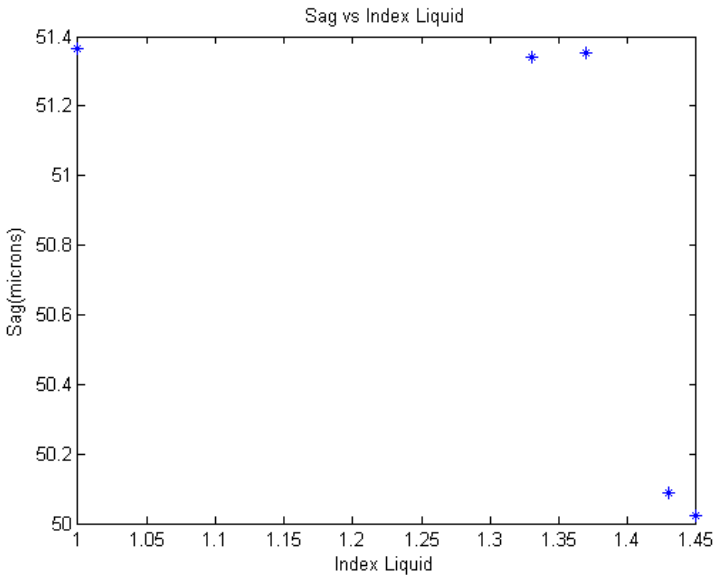

Figure 104: Corrected sag values with interferometer bias removed.

Refraction Effects

As mentioned previously, refraction plays an important role in the analysis of micro-structures. Neglecting the effects of refraction causes a systematic bias in the measurement. Taking the measurement of a micro-pyramid as an example, the first order analysis that considers changes in the optical path length due to the index alone leads to the relationship between the height of the micro-pyramid and the OPD of the micro-pyramid under test that is given by

$$h(x,y) = \frac{OPD(x,y)}{\Delta n} \tag{80}$$

where Δn is the difference in refractive index between the sample and the index liquid 55]. By taking the derivative of equation (80) the slope and hence the facet angle can be

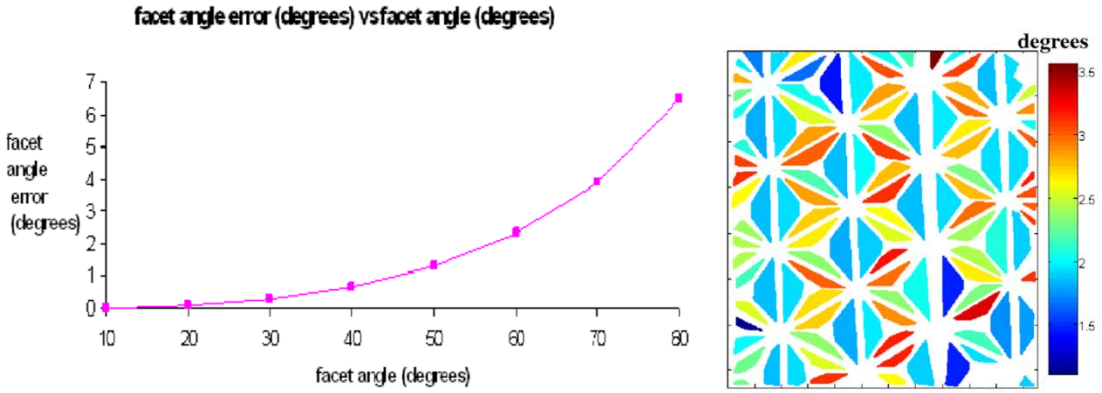

(a) (b)

Figure 105 (a) Facet angle error as a function of facet angle. (b) Facet angle error map for Reflexite sample illustrating the error in facet angle that occurs by neglecting refraction effects.

recovered. This facet angle though will be inaccurate because refraction is ignored at the sample-index interface. Figure 105 shows a graph of facet angle error versus facet angle for the situation in which refraction is ignored, that is, using equation 80 to approximately calculate facet angle versus using equation 55. As expected, the facet angle error

increases with facet angle. Figure 105(b) illustrates the facet angle error map for the Reflexite sample. To show this error, we process the measured data of the Reflexite sample and scale the OPD measurement by using equation (80) only, and then processed the height profile to extract the facet angles. This result is subtracted from the analysis result that correctly takes refraction into account (equation 55), and this difference map is shown in Figure 105(b). Ignoring the details of refraction can result in angle errors as large as 3.6 degrees.

Masking Effects

In index liquid metrology, the calculation of the sag, ROC and form errors of a micro-lens is of paramount importance. The sag is defined as the distance between the apex and substrate of a micro-lens. For this reason, when measuring the sag of a micro-lens array the substrate is included. However, from the 3-D surface map, the ROC and form error can be calculated by masking the clear aperture of the lens from the substrate. This is normally done in optical software by using the edges of the interferogram to find the center of the surface map. However, due to low modulation, low lateral resolution, or diffraction effects, the edges of the micro-lens aperture are difficult to locate. If the center of the mask does not coincide with the center of the surface profile or *OPD* map, asymmetric aberrations can be induced from symmetric aberrations (Figure 106). For example, if a micro-lens has spherical aberration, which is a frequent case, one could define a symmetric function as

$$\rho^4 = \left(x^2 + y^2\right)^2. \tag{81}$$

If the center of the mask is off from the center of the micro-lens aperture by *dy*, equation

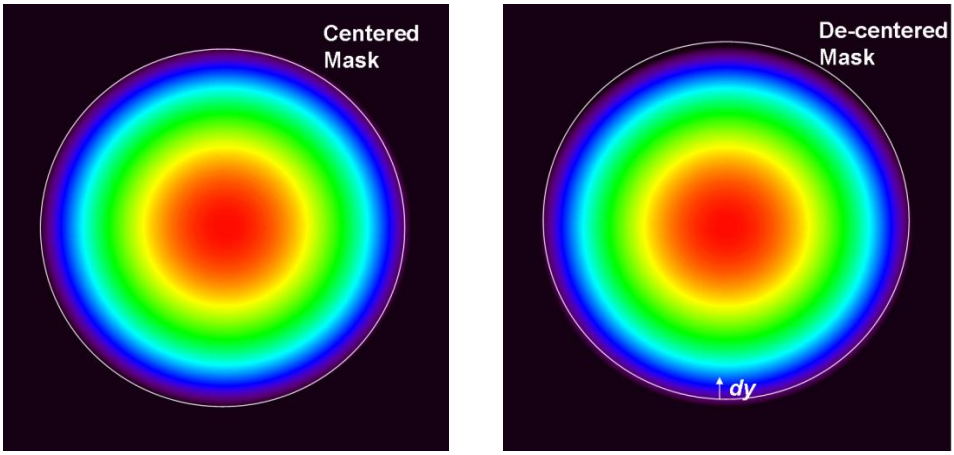

(a) (b)

Figure 106: (a) Centered Mask. (b) De-centered mask in y.

81 becomes [85]

$$\left(x^2+\left(y+dy\right)^2\right)^2 \approx \left(\left(x^2+y^2\right)+2ydy\right)^2 \approx \rho^4+\left(4dy\right)\rho^2 y\,. \tag{82}$$

Therefore, if the micro-lens has a ρ^4 shape, such as spherical aberration, by not centering the mask to the center of the micro-lens aperture, one could induce an asymmetric term $\rho^2 y$ (similar to coma). To see the magnitude of induced coma from a misaligned mask, a perfect sphere was simulated in Vision, with a ROC of 600 microns and sag of 50 microns. A Zernike mask was then intentionally misaligned across the aperture in the y-direction and the resulting coma noted. Figure 107 illustrates that for a misalignment in the mask of 1 pixel, 0.067 waves of coma could be induced in the surface profile. This could lead to erroneous information when investigating the form error of a lens. It is therefore necessary to check on the sensitivity of the mask alignment when measuring a micro-lens via the index liquid technique. One technique that can be employed is to observe the tilt coefficients as the mask is raster scanned across the aperture of the micro-

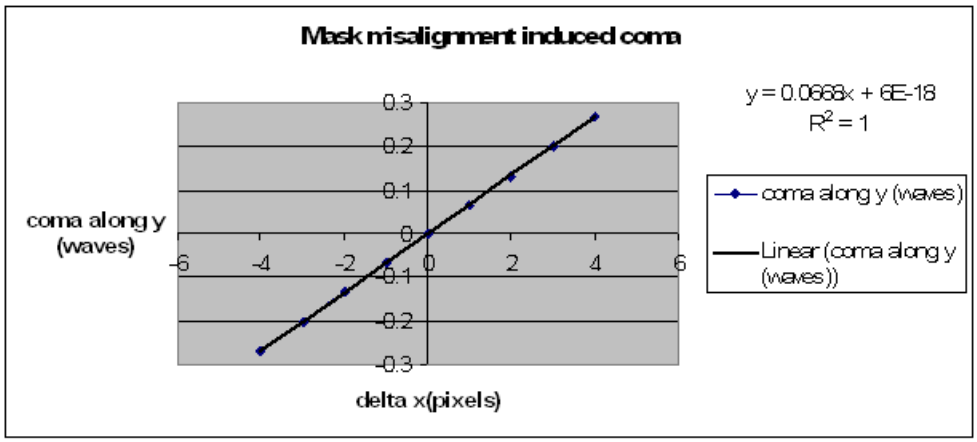

Figure 107: Coma induced by a mask-misalignment.

lens. The position of the mask which results in the minimum magnitude tilt coefficients can be safely assumed to be where the center of the mask coincides with the center of the micro-lens aperture. This technique, assumes that tilt has already been removed from the micro-lens aperture.

Pixel Calibration

As we have previously seen, it is important to calibrate the pixel size in both directions when measuring the ROC of a micro-lens array. To reveal the form errors of the micro-lens the best fit sphere is normally subtracted from the surface profile of the lens. If the calibration of the lateral dimensions is inaccurate this leads to induced aberrations in the form error map. For most cases, it is assumed that the pixel size in both the *x* and *y* directions are the same. However, most CCD cameras are rectangular in their pixel size and spacing, and if this is not taken into account, this may lead to induced asymmetric aberrations. As an example, using the surface profile of the DOC micro-lens obtained using an index liquid of 1.80, the pixel size in *x* and *y* is intentionally made the same (1.154 μm). Figure shows the form error map for this case compared to that for

which the pixel size in *x* (1.154 μm) and *y* (1.116 μm) are correctly calibrated. As one can see from the maps, astigmatism has clearly been induced into the form error maps. In fact for a mis-calibration of 38 nm we get an increase in astigmatism of ~2.9 waves. This clearly demonstrates the need for a detailed lateral calibration.

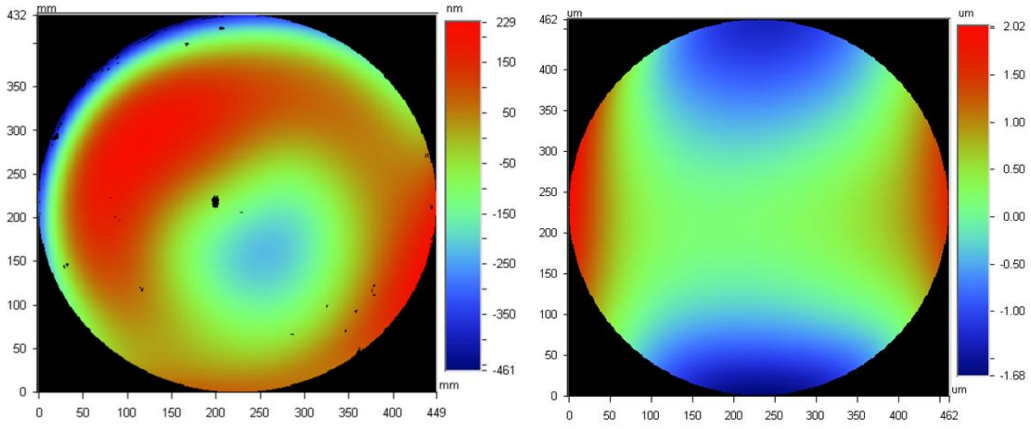

(a) (b)

Figure 108: (a) Form error map with correct lateral calibration. (b) Form error map with incorrect lateral calibration showing induced astigmatism.

CHAPTER 6: CONCLUSIONS AND FUTURE WORK

This dissertation has presented the index liquid technique as a viable option in measuring microstructures in the form of micro-lenses and micro-pyramids. A novel technique was developed that improved the capability of traditional interferometry by extending its dynamic range to enable measurements of micro-optics structures and to reduce the testing time compared to other techniques. Important micro-lens properties such as the sag, radius of curvature and form errors for a micro-lens were measured and the results compare favorably to measurements taken on a Twyman-Green interferometer, Veeco Dektak contact profilometer and an optical non-contact profilometer (WYKO NT 2000). Another goal of this dissertation was to enable measurements of arbitrary geometries and to reduce testing time compared to profilometry. It was shown that measurements of a micro-pyramid array using the index liquid technique compared favorably to measurements on a VEECO Dektak contact profilometer. Measurements took approximately five seconds to complete compared to a measurement time of six hours for the contact profilometer. Also, the index liquid technique allowed a measurement of the angle between facets of a nickel micro-corner cube hexagonal array, a combination not previously demonstrated in the literature. Lastly, a detailed uncertainty analysis was carried out on the index liquid technique to determine any limiting factors that need to be taken into account when implementing such a technique. From this analysis, it was found that retrace errors had the largest effect on the

measured sag of micro-lens. As an extension to the index liquid technique, stitching routines can be added to the current procedure which will significantly increase the measurement area. Although this will increase the time taken to conduct an entire measurement, this setback will be significantly outweighed by the benefits to the process engineer who will now have more data to increase the quality and provide feedback to the manufacturing process. One potential risk in adding stitching routines is a delay period that will need to be added that will give the sample which is immersed in the index liquid enough time to settle. This though should not be more than a couple of seconds. The retrace error calibration could be further improved by introducing an artifact with varying tilt (e.g. wedged plate) that can not only give one insight into the asymmetric aberrations introduced by retrace errors but also would give one a pixel by pixel correction for retrace error. This would eliminate the need to calibrate the interferometer every time a new micro-lens sample was introduced [125]. Another potential application is to introduce an index liquid to a PSI white light interferometer. There are many of these types of interferometers in the marketplace, and they are used for many metrology applications. However they suffer from the same drawbacks of the Nyquist sampling theorem, which then can be alleviated using an index liquid. However, a specialized afocal system will have to be designed for each field of view requirement, as well as specialized filters will have to be introduced to increase the coherence length of the light source. The sample will also have to be oriented in a particular way in order to take advantages of refraction.

REFERENCES

1. J.J. Snyder, “Cylindrical micro-optics”, Proc. SPIE, 1992, *Miniature and Micro-optics and Micromechanics*, 235-246, 1993.

2. P. Savander, H-J. Haumann, “Microlens array used for collimation of linear laser diode array”, *Measurement Science and Technology*, 4, 541-543, 1993.

3. K. Hamanka, T. Kishimoto, “Multiple imaging and multiple Fourier transformation using microlens arrays”, *Japanese Journal of Applied Physics*, 29 (7), 1277-1280, 1990.

4. J. Jahns, W. Daschner, “Optical cyclic shifter using diffractive lenslet arrays”, Optics Communications, 79 (6), 407-410, 1990.

5. J. Leggett, M.C. Hutley, “Microlens arrays for interconnection of singlemode fibre arrays”, *Electronics Letters*, 27 (3), 238-240, 1991.

6. N. T. Gordon, C.L. Jones, D.R. Purdy, “Application of Microlenses to Infrared Detector Arrays”, *Infrared Phys*., 31 (6), 599-604, 1991.

7. R. Shack, B. Platt, “Production and use of a lenticular Hartmann screen”, *Journal of the Optical Society of America*, 61(5), 656, 1971.

8. G. Artzner, “Microlens arrays for solar astronomy”, *Institute of Physics Short Meetings on Microlens Arrays*, 91-96, 1991.

9. H. Tiziani, H. Uhde, “Three dimensional analysis by a microlens array confocal arrangement”, *Applied Optics*, 33 (4), 567-572, 1994.

10. G. Lippmann, “Epreuves reversibles: Photographies integrals”, *Comptes Rendus*, 146, 446-451, 1908.

11. J. Rees, “Office applications of gradient index optics”, Proc. SPIE, 935, Gradient Index Optics and Miniature Optics, 1988.

12. H. Urey, “Common Optical MEMS Stage as a Platform for many Applications”, NEMO news, 2, pg 10, 2006.

13. I. Iga, Y. Kokubun, M. Oikawa, Fundamentals of Microoptics, Academic Press, London, 1984.

14. N. F. Borrelli, D.L. Morse, R. H. Bellman, W.L. Morgan, “Photolytic technique for producing microlenses in photosensitive glass”, Applied Optics, 24 (16), 2520-2525, 1985.

15. M. Kufner, S. Kufner, “Microlenses in PMMA by deep proton irradiation – capacity of the process”, European Optical Society Topical Meetings Digest Series: Volume 2, Microlens Arrays, 5-8, 1993.

16. F. W. Ostermayer, P.A. Kohl, R. H. Burton, “Photoelectochemical etching of integral lenses on InGaAsP/InP”, Applied Physics Letters, 43 (7), 642-644, 1983.

17. D. Daly, Microlens Arrays, CRC, 2000.

18. J. Dou, et.al, “Laser machining of micro-lenses on the end face of single-mode optical fibers,” Applied Physics A: Materials Science & Processing, 91 (4), 591-594, 2008.

19. B. T. Teipen, D.L. MacFarlane, “Modulation transfer function measurements of microjetted microlenses”, Applied optics, 38 (10), 2040-2046, 1999.0

20. M. C. Hutley, “Optical techniques for the generation of microlens arrays”, J. Mod. Opt., 37 (2), 253-265, 1990.

21. D. H. Ranguin, et.al, “Anamorphic and aspheric microlenses and microlens arrays for telecommunication applications”, Optical Fiber Communication Conference and Exhibit, 1, 2001.

22. Y. Huang, H. Shieh, and S. Wu, “Applications of multidirectional asymmetrical microlens-array light-control films on reflective liquid-crystal displays for image quality enhancement,” Appl. Opt. 43, 3656-3663 (2004).

23. G. Seward and P. Cort, “Measurement and characterization of angular reflectance for cube-corners and microspheres,” Opt. Eng. 38, 164-169 (1999).

24. G. Olson, H. Mocker, N. Demma, and J. Ross, “Coherent CO_2 laser communication system with modulable retroreflectors,” Appl. Opt. 34, 2033-2044 (1995).

25. K. Ryu, J. Rhee, K. Park, and J. Kim, “Concept and design of modular Fresnel lenses for concentration solar PV system,” Solar Energy 80, 1580-1587 (2006).

26. C. Moser, T. Mayr and I. Klimant, “Filter cubes with built-in ultrabright light-emitting diodes as exchangeable excitation light sources in fluorescence microscopy,” J. Microscopy 222, 135-140 (2006).

27. C. Gimkiewicz, et.al, "Fabrication of microprisms for planar optical interconnections by use of analog grey-scale lithography with high-energy-beam-sensitive glass," Appl. Opt. 38, 2986-2990 (1999).

28. K. Brenner, et.al, "Application of three-dimensional micro-optical components formed by lithography, electroforming, and plastic moulding", Appl. Opt. 32, 6464-6469 (1993).

29. A. Rohrbach and K.-H. Brenner, "Surface-relief phase structures generated by light-initiated polymerization", Appl. Opt. 34, 4747-4754 (1995).

30. T.A. Ballen and J.R. Leger, "Mass-transport fabrication of off-axis and prismatic gallium phosphide optics", Appl. Opt. 38, 2979-2985 (1999).

31. R.A. Hoffman, et.al, "Ion polishing as a surface preparation for dielectric coating of diamond turned optics", Opt. Eng. 17, 578-585, 1978.

32. G. C. Blough, et.al, "Single point diamond turning and replication of visible and near-infrared diffeactive optical elements", Appl. Opt. 36, 4648-4654 (1997).

33. E. Brinksmeier, R. Gläbe, C. Flucke, "Manufacturing of molds for replication of micro cube corner retroreflectors," Production Engineering 2, 33-38 (2008).

34. H. Seidel and R. Voss, "Anisotropic silicon etching techniques", VDE Verlag, *Microsystems Technologies 91*, Berlin, Germany, 291-301.

35. H. Sickinger, J. Schwider and B. Manzke, "Fiber based mach-Zehnder interferometer for measuring wave aberrations of microlenses," *Optik*, 110, 239-243 (1999).

36. D. Malacara, "Twyman-Green Interferometer," in *Optical Shop Testing*, D. Malacara, ed. (John Wiley & Sons, 1992), pp. 51-94.

37. H. Sickinger, O. Falkenstorfer, N. Lindlein and J. Schwider, "Characterization of microlenses using a phase-shifting shearing interferometer." *Opt. Eng*. 33, 2680-2686 (1994).

38. J. Schwider and H. Sickinger, "Array tests for microlenses," *Optik* 107(1), 26-34 (1997).

39. H. Schreiber and J. Schwider, "A lateral shearing interferometer based on two Ronchi-phase grating in series," *Appl. Opt*., 36, 5321-5324 (1997).

40. P. Pulaski, et. al., "Measurement of aberrations in microlenses using a Shack-Hartmann wavefront sensor," *SPIE* 2002.

41. D. Daly, M. Hutley, "Microlens measurement at NPL," *Proc IOP/NPL meeting Microlens Arrays* held at NPL Teddington, 50-54, May 1993.

42. Y. Gao, M. Hutley, "Chromatic dispersion of microlenses," *Proc IOP/NPL meeting Microlens Arrays* held at NPL Teddington, 65-69, May 1995.

43. H. Tiziani, T. Haist and S. Reuter, "Optical inspection and characterization of microoptics using confocal microscopy," *Optics and Lasers in Engineering*, 36, 403-415 (2001).

44. M. Born and E. Wolf, Principles of Optics: Electromagnetic Theory of Propagation, Interference and Diffraction of Light. Cambridge University Press 1999.

45. http://www.taylor-hobson.com/optics-pgi.html

46. A. Harasaki, J. Schmit, and J. Wyant, "Improved vertical scanning interferometry," Appl. Opt. 39, 2107-2115 (2000).

47. J. Schwider, O. Falkenstorfer, " Twymann-Green interferometer for testing microspheres," *Proc IOP/NPL meeting Microlens Arrays* held at NPL Teddington, 60-64, May 1995.

48. K. Seong, and J. Greivenkamp, "Surface figure measurement based on the transmitted wavefront with reverse raytracing," Opt. Eng. 47, (2008).

49. J. E. Greivenkamp and J. H. Bruning, "Phase Shifting Interferometry," in *Optical Shop Testing*, D. Malacara, ed. (John Wiley & Sons, 1992), pp. 501-598.

50. J. E. Grivenkamp, "Sub-Nyquist Interferometry," Appl. Opt. 26, 5245 (1987b).

51. T. Bothe, W. Li, C. Kopylow, and W. Juptner, "Fringe reflection for high resolution topmetry and surface description on various lateral scales," in *Fringe 2005: The 5th International Workshop on Automatic Processing of Fringe Patterns*, W. Osten, ed. (Springer, 2005), pp. 362-371.

52. T. Ballinger and J. Huedepohl, "Advantages of Using Dektak Surface Profilers with Vision 3D Analysis Software," Application Note 542.

53. E. Peiner, M. Balke, L. Doering, and U. Brand, "Tactile probes for dimensional metrology with microcomponents at nanometer resolution," Meas. Sci. Technol. 19, 6 (2008).

54. E. Manske, T. Hausotte, R. Mastylo, T. Machleidt, K-H. Franke and G. Jager, "New applications of the nanopositioning and nanomeasuring machine by using

advanced tactile and non-tactile probes," Meas. Sci. Technol. 18, 520-527 (2007).

55. J. Kuhn, F. Charrière, T. Colomb, E. Cuche, Y. Emery and C. Depeursinge, "Digital holographic microscopy for nanometric quality control of micro-optical components," Proc. SPIE 6475, (2007).

56. D. Purcell, A Suratkar, A. Davies and F. Farahi F, "Measuring the Wavefront Distortion of a Microlens Array Using an Index Matching Liquid," presented at Optical Fabrication and Testing Topical Meeting, NY, USA, 9–11 October 2006.

57. J. Schwider, H. Sickinger, "Arraytests for microlenses," Optik 107, 26-34 (1997).

58. Z. Yun, Z. Liu and Y. Li, "Aspheric surface testing with a liquid compensatory interferometer," Opt. Eng. 37, 1364-1367 (1998).

59. Z. Yun. Y. Li, Z. Liu, "Simple technique for testing deep aspherical surface," Opt. Eng. 38, 650-654 (1999).

60. H. Sickinger, J. Schwider, B. Manzke, "Fiber based Mach-Zehnder interferometer for measuring wave aberrations of microlenses," Optik 110, 239-243 (1999).

61. K. Seong and J. Greivenkamp, "Surface figure measurement based on the transmitted wavefront with reverse raytracing", Opt. Eng. 47, 0430602 (2008).

62. G.A. Williby, D.G. Smith, R.A. Brumfield and J.E. Greivenkamp, "Interferometric Testing of Soft Contact Lenses," Proc. of SPIE 5180, 329-339 (2003).

63. N. Gardner and A. Davies, "Retrace error evaluation on a figure-measuring interferometer," in Proc. SPIE, 2005, pp. 217-224.

64. H. Ottevaere, H. Thienpont, "Refractive optical microlenses: An introduction to nomenclature and characterization techniques," in *Encyclopedia of Modern Optics*, vol. 4, Robert D. Guenther and Duncan G. Steel, Academic Press, 2004, pp. 21-43.

65. J. Schwider, O. Falkenstorfer, "Twyman-Green interferometer for testing microspheres," Opt. Eng. 34, 2972-2975 (1995).

66. A. Olszak, M. Zecchino, "Lateral-Scanning Interferometry takes the long view," Photonics Spectra, No. 7, 2002.

67. Advanced Development Profiler Manual, Software Version 8.33 2003 *Manual Dektak 8M*, Veeco Inc.

68. E. Hecht, "More on Geometrical Optics", Chapter 6 in *Optics*, Addison-Wesley Publishing Company, 1987, pp. 243-280.

69. F. Jenkins, "Thick Lenses", Chapter 5 in *Fundaments of Optics*, 3rd edition, McGraw-Hill, 1981, pp. 62-79.

70. W. Smith, "Engineering an optical system", *SPIE OE Magazine*, pp. 49-54, July, 2002.

71. F.L. Pedrotti and L.S. Pedrotti, "Aberration Theory", Chapter 5 in *Introduction to Optics*, 2nd edition, Prentice Hall International, 1993, pp. 84-105.

72. D. Malacara and S. DeVore, "Interferogram Evaluation and Wavefront Fitting," Chapter 13 in *Optical Shop Testing*, 2nd edition, John Wiley & Sons, 1992, pp. 455-500.

73. James C. Wyant, "Zernike polynomials and phase-shifting interferometry," http://wyant.optics.arizona.edu

74. M. Born and E. Wolf, "The Diffraction Theory of Aberrations," Chapter IX in *Principles of Optics*, 7th edition, Pergamon Press, 1999, pp. 523-525.

75. M. Rimmer and J. Wyant, "Evaluation of Large Aberrations Using a Lateral Shear Interferometer Having Variable Shear," Appl. Opt., 14, 142-150 (1975).

76. E. Hecht, "Diffraction", Chapter 10 in *Optics*, Addison-Wesley Publishing Company, 1987, pp. 443-518.

77. E. Hecht, "Geometrical Optics", Chapter 5 in *Optics*, Addison-Wesley Publishing Company, 1987, pp. 151-152.

78. R. A. Buchroeder, et al, "The Design, Construction, and testing of the Optics for a 147-cm-Aperture Telescope," *Optical Sciences Center Technical Report*, No. 79, University of Arizona, 1972.

79. D. Malacara, "An Optical Surface and Its Characteristics," Appendix 1 in *Optical Shop Testing*, John Wiley & Sons, Inc, 1992, pp. 743-753.

80. P.Savander, "Microlens arrays etched into glass and silicon," Opt. Lasers Eng., 20, 97-107 (1994).

81. J. Govier, "ASPHERIC OPTICS: Technological advances ease use of aspherics," Laser Focus World, 2005.

82. M. V. Mantravadi, "Newton, Fizeau, and Haidinger Interferometers," Chapter 1 in *Optical Shop Testing*, 2nd edition, John Wiley & Sons, 1992, pp. 1-49.

83. R. Plymton, "Asphere Metrology: Options for Measuring aspheric lenses," Optimax Application Note (2008).

84. L. Selberg, "Interferometer Accuracy and Precision," Proc. SPIE, 1400, 24 (1990a).

85. A. Lowman and J. Greivenkamp, "Interferometer induced wavefront errors when testing in a non-null configuration," Proc. SPIE, 2004, 173-181 (1993).

86. C. J. Evans, "Compensation for errors introduced by nonzero fringes densities in phase-measuring interferometers," Int. Inst. Prod. Res. Ann. 42, 577-580 (1993).

87. P. Murphy, T. Brown and D. Moore, "Measurement and calibration of interferometric aberrations," Appl. Opt. 39, 6421-6429 (2000).

88. R. Gappinger and J. Greivenkamp, "Iterative reverse optimization procedure for calibration of aspheric wave-front measurements on a nonnull interferometer," Appl. Opt. 43, 5152-5161 (2004).

89. D. Daly, "Application and Fabrication Techniques," Chapter 2 in *Microlens Arrays,* 1st edition, CRC, 2000, pp. 7-39.

90. S. Sinzinger, J. Jahns, "Refractive microoptics," Chapter 5 in *Microoptics*, 2nd edition, Wiley-VCH, 2003, pp. 121-124.

91. *Exploring Surface Texture*, published by Talyor Hobson Limited, (2003).

92. *Reflection and Retro-reflection*, technical note RS101, published by Delta.

93. *J. Yuan, S. Chang, S. Li and Y. Zhang, "Design and fabrication of micro-cube-corner array retro-reflectors," Opt. Comm., 209, 75-83 (2002).*

94. E. Brinksmeier, R. Glabe and C. Flucke, "Manufacturing of molds for replication of micro-cube corner retro reflectors," Prod. Eng., 2, 33-38 (2007).

95. L. Lin, T. Shia and C. Chiu, "Silicon-processed plastic micropyramids for brightness enhancement applications," J. Micromech. Microeng., 10, 395-400 (2000).

96. C. J. Evans, "Compensation for errors introduced by non-zero fringe densities in phase-measuring interferometers," CIRP Annals 42(1), 577-580 (1993).

97. C. Huang, "Propagation errors in precision Fizeau interferometry," Appl. Opt. 32, 7016-7021 (1993).

98. P. E. Murphy, T. G. Brown, and D. T. Moore, "Measurement and calibration of interferometric imaging aberrations," Appl. Opt. 39, 6421-6429 (2000).

99. M. Change and C.S.Ho, "Phase-measuring Profilometry Using Sinusoidal Grating," Experimental Mechanics, 33, 117 (1993).

100. http://www.cargille.com/refractivestandards.shtml

101. *Mach-Zehnder interferometer for measuring wave aberrations of microlenses*, User's Guide, PSI Version 5.3, University Erlangen-Nurnberg, J. Schwider, 2002.

102. S. Reichelt, and H. Zappe, "Combinee Twyman-Green and Mach-Zehnder interferometer for microlens testing," Appl. Opt. 44, 5786-5792 (2005).

103. *Twyman-Green interferometer for testing microlens surfaces,* User's Guide, University Erlangen-Nurnberg, J. Schwider, 1998.

104. *Manual WYKO NT-2000*, Operator's Guide Version 1.00, USA, 1997.

105. V. Gomez, et. al., "Micro-optic reflection and transmission for complete microlens characterization," Meas. Sci. Technol. 20, (2009).

106. K. Medicus, "Improving Measurements Based on the Cat's Eye Retro-Reflection," Ph.D. dissertation (University of North Carolina at Charlotte, North Carolina, 2006.)

107. M. V. Mantravadi, "Newton, Fizeau, and Haidinger Interferometers," Chapter 1 in *Optical Shop Testing*, 2nd edition, John Wiley & Sons, 1992, pp. 1-49.

108. D. Daly, "The Method of Manufacturing Microlenses by Melting Photoresist," Chapter 3 in *Microlens Arrays,* 1st edition, CRC, 2000, pp. 40-77.

109. http://www.mathworks.com/access/helpdesk/help/toolbox/curvefit/bq_5ka6-1.html

110. http://www.mathworks.com/access/helpdesk/help/toolbox/curvefit/bq_5ka6-1_1.html

111. L. Selberg, "Radius measurement by interferometery," Optical Engineering, 31, pp. 1961-1966, 1992.

112. T. Schmitz, A. Davies and C. Evans, “Uncertainties in interferometric measurements of radius of curvature,” in Optical Manufacturing and Testing IV, Proccedings of SPIE Vol., 4451, pp. 432-447, 2001.

113. D. Purcell, A. Suratkar, A. Davies, F. Farahi, H. Ottevaere and H. Thienpont, “Interferometric technique for faceted microstructure metrology using an index matching liquid,” Appl. Opt. 49 (4), 732-738, 2010.

114. A. O'Neill, J. Soo Hoo and G. Walker, " Chips & Tips: Rapid curing of PDMS for microfluidic applications,” http://www.rsc.org/Publishing/Journals/lc/PDMS_curing.asp.

115. K. Kim, S. Park, J.-B. Lee, H. Manohara, Y. Desta, M. Murphy, and C. H. Ahn, Rapid replication of polymeric and metallic high aspect ratio microstructures using PDMS and LIGA technology,” Microsyst. Technol. 9, 5-10 (2002).

116. P. Bevington and D. Robinson, *Data Reduction and Error Analysis for the Physical Sciences* (McGraw-Hill, 1992).

117. *Guide to the Expression of Uncertainty in Measurement*, International Organization for Standardization, 1993.

118. Daryl Purcell, Construction and Error Analysis of a fringe projection system, *Master’s thesis*, University of North Carolina at Charlotte, 2005.

119. T. M Niebauer, “Frequency stability measurements on polarization-stabilized He-Ne lasers”, Appl. Opt 27(7), 1285.

120. J. Van Wingerden, H. J. Frankena, and C. Smorenburg, “Linear Approximation for Measurement Errors in Phase Shifting Interferometry,” *Appl. Opt*., 30, 2718 (1991).

121. V. Alvarez-Valado, et. al., “Testing phase-shifting algorithms for uncertainty evaluation in interferometric gauge block calibration,” *Metrologia*, 46, 637-645 (2009).

122. http://www.vertex42.com/ExcelArticles/mc/MonteCarloSimulation.html

123. B.C. Reed, “"Linear least-squares fits with errors in both coordinates", Am. J. Phys 57, 642 (1989).

124. Philip (Flip) Kromer, *Least Squares Fitting in Excel with Error in Both Variables* (http://vizsage.com/other/leastsquaresexcel/)

125. To Be Submitted: D. Purcell, A. Davies, “Experimental retrace-error correction for a non-null interferometer,” APPLIED OPTICS 2010.